Structure and properties of nanostructured materials from atomistic modeling and advanced diffraction methods

Luca Gelisio

December 31, 2014

Approved by

Prof. P. Scardi, University of Trento
Prof. I.K. Robinson, London Centre for Nanotechnology
Dr. P. Frontera, Mediterranean University of Reggio Calabria

Gelisio, Luca. *Structure and properties of nanostructured materials from atomistic modeling and advanced diffraction methods.* PhD Thesis, University of Trento (2014).

to my family

Contents

List of Equations

List of Algorithms

List of Tables

List of Figures

Chapter 1

Introduction

Matter at the *nanoscale* exhibits peculiar properties, often not shown by the bulk counterpart, and strongly coupled to the specific size, shape and structure of the atomic aggregate. Particularly, the enormous surface-to-volume ratio implies boosted reactivity with respect to the environment, while the electronic confinement might cause quantum effects to dominate physical properties.

One famous experiment demonstrating the size-dependency of the melting temperature of gold was given by Buffat and Borel [1], which reported this quantity to vary from the bulk value, approximately 1300K, to 800K for an aggregate as small as 2.5nm diameter. By the way, peculiar properties revealed at the nanoscale have been exploited since thousands of years, *exempli gratia* the Lycurgus Cup [2], a *diatretum* belonging to the 4th century AD, dichroic because of optical properties of gold-silver nanostructured particles embedded in the glass matrix. Nature also exploits nanotechonology, employed for example to create diffraction gratings on the wings of some butterflies or to produce self-cleaning lotus leafs.

The range of applicability of nanostructured materials is enormous, with notable cases in catalysis and medical imaging.

Characterization techniques are of course essential to investigate properties at the atomic scale. *Scattering techniques* have tremendously evolved in the recent past benefiting from third and fourth generation light sources, producing beams with unprecedented spatial and

temporal resolution. In a different realm, *atomistic simulations* have also greatly evolved deriving advantages from both recent theories and modern computing units. In this framework, a detailed description of the system in a spatial and temporal range compatible with lengths probed by scattering techniques is provided.

In a single sentence, the subject of this Thesis is the effort of tying atomistic methods and scattering techniques so to increase the comprehension around size, shape and structure of nanostructured particles.

A concise theoretical background for atomistic simulations, in particular projected onto the case of classical molecular dynamics, is discussed in chapter 2. Next, chapter 3 introduces the kinematical theory of scattering of X-rays. The expression for the intensity distribution is built without invoking the concept of unit cell but instead considering the given atomic aggregate as a single, big molecule. Supported by atomistic simulations, structural and dynamical features arising from the finiteness of the body are discussed in chapter 4, with particular emphasis on the effect on scattered intensity. To conclude, chapter 5 describes, around a case study, an algorithm for modeling scattering data while accounting for concepts discussed in previous chapters.

Chapter 2

Atomistic simulations

> If, in some cataclysm, all of scientific knowledge were to be destroyed, and only one sentence passed on to the next generation of creatures, what statement would contain the most information in the fewest words? I believe it is the atomic hypothesis (or the atomic fact, or whatever you wish to call it) that all things are made of atoms – little particles that move around in perpetual motion, attracting each other when they are a little distance apart, but repelling upon being squeezed into one another. In that one sentence, you will see, there is an enormous amount of information about the world, if just a little imagination and thinking are applied.
>
> R.P. Feynman, 1964 [3]

In 1952 the *Mathematical Analyzer, Numerical Integrator, and Computer* (MANIAC-1) began operations at the Los Alamos Scientific Laboratory [4]. In the following year, Metropolis and colleagues devised the first (Metropolis Monte Carlo (MMC)) computer simulation of a bi-dimensional system of rigid spheres [5]. Within a decade, Fermi, Pasta and Ulam simulated the dynamics of a one-dimension anharmonic crystal (engendering the FPU problem) [6]; Alder and Wainwright performed the first molecular dynamics (MD) simulation of hard spheres moving at constant velocity between elastic collisions [7]; Gibson and colleagues simulated a "real material" (copper) undergoing radiation damage [8]. In 1964, Rahman used a realistic potential to model liquid argon and succeeded to accurately match some experimental data [9].

Computer experiments are chiefly a tool to predict/understand the properties of materials. If experimental conditions are precisely mimicked, simulation results can be, more or less directly, compared with observed data. This allows the underlying theoretical model to be tested and, in case it is accurate, the simulation can assist in the interpretation of results. On the other hand, any arbitrarily difficult – or impossible – condition to be measured can be thought and realized. For instance, properties of iron at the pressure and temperature of Earth's core can be determined [10].

Broadly speaking, MMC methods consist in stochastically generating a set of atomic positions according to an appropriate statistical-mechanical distribution, therefore granting access to static equilibrium averages (see *e.g.* [11]). Dynamic properties are available from MD simulations, a deterministic technique where the time evolution of a many-body system is described by solving the Newton's equations of motion [12] (see section 2.2).

While producing a comprehensive theoretical framework for atomistic simulations is beyond the scope of this document, some selected concepts and methods concisely follow-up. Superb reference sources are, in my opinion, the evergreen by Allen and Tildesley [13], books by Frenkel and Smit [11] and by Leach [14] and the document by Ercolessi [15]. The formalism used to connect microscopic and macroscopic realms is the one of *statistical-mechanics*, thoroughly explained, for example, in the book by Chandler [16] or the one by Tuckerman [17].

2.1 Interaction potential

Atomic interactions are of course ruled by quantum mechanics. The full non-relativistic Hamiltonian for an atomic aggregate is

$$\hat{H} = \hat{K} + \hat{V} = \hat{K}_n + \hat{K}_e + \hat{V}_{nn} + \hat{V}_{ne} + \hat{V}_{ee}, \tag{2.1}$$

being $\hat{K}_n$ and $\hat{K}_e$ the kinetic energy operators for nuclei and electrons whereas terms $\hat{V}_{nn}$, $\hat{V}_{ne}$ and $\hat{V}_{ee}$ express the nuclei-nuclei, electron-electron and nuclei-electron interaction. Considering N nuclei and E

electrons, equation 2.1 can be expressed (using atomic units) as

$$\begin{aligned}\hat{H} = &\sum_{n=1}^{N} \frac{\hat{p}_n^2}{2m_n} + \sum_{e=1}^{E} \frac{\hat{p}_e^2}{2m'_e} + \frac{1}{2}\sum_{n=1}^{N}\sum_{u=1}^{N} \frac{Z_n Z_u}{\|\mathbf{r}_n - \mathbf{r}_u\|} \\ &+ \frac{1}{2}\sum_{e=1}^{E}\sum_{l=1}^{E} \frac{1}{\|\mathbf{r'}_e - \mathbf{r'}_l\|} - \sum_{n=1}^{N}\sum_{e=1}^{E} \frac{Z_n}{\|\mathbf{r}_n - \mathbf{r'}_e\|},\end{aligned} \tag{2.2}$$

where m, $\hat{\mathbf{p}}$, Z and $\mathbf{r}$ are, respectively, the mass, the momentum operator, the atomic number and the position vector of a nucleus whereas primed quantities refer to an electron. The solution of the Schrödinger equation [18],

$$\hat{H}\,\Psi\left(\mathbf{r}, \mathbf{r'}\right) = E\,\Psi\left(\mathbf{r}, \mathbf{r'}\right) \tag{2.3}$$

provides the total wave function ($\mathbf{r}$ and $\mathbf{r'}$ are, respectively, the set of all nuclear and all electronic coordinates) and therefore the complete description of the system.

2.1.1 Adiabatic approximation

To reduce the complexity of the problem, Born and Oppenheimer introduced the *adiabatic approximation* [19], built around the concept that electrons move faster than nuclei (being much lightweight) and adiabatically follow nuclear motion. Electronic and nuclear motion are therefore separated in this framework and the wave function, in turn, is expressed as

$$\Psi\left(\mathbf{r}, \mathbf{r'}\right) = \psi_N\left(\mathbf{r}\right)\,\psi_E\left(\mathbf{r'}; \mathbf{r}\right), \tag{2.4}$$

being ψ_N and ψ_E the wave function of the nucleus and of the electron (which parametrically depends on nuclear positions), respectively. Equation 2.3 can therefore be divided into an electronic equation (considering fixed nuclei positions),

$$\begin{aligned}\left(\sum_{e=1}^{E} \frac{\hat{p}_e^2}{2m_e} + \frac{1}{2}\sum_{n=1}^{N}\sum_{u=1}^{N} \frac{Z_n Z_u}{\|\mathbf{r}_n - \mathbf{r}_u\|} + \frac{1}{2}\sum_{e=1}^{E}\sum_{l=1}^{E} \frac{1}{\|\mathbf{r'}_e - \mathbf{r'}_l\|}\right. \\ \left. - \sum_{n=1}^{N}\sum_{e=1}^{E} \frac{Z_n}{\|\mathbf{r}_n - \mathbf{r'}_e\|}\right)\psi_E\left(\mathbf{r'}; \mathbf{r}\right) = V\left(\mathbf{r}\right)\psi_E\left(\mathbf{r'}; \mathbf{r}\right),\end{aligned} \tag{2.5}$$

and a nuclear equation,

$$\left(\sum_{n=1}^{N}\frac{\hat{p}_n^2}{2m_n}+V\left(\mathbf{r}\right)\right)\psi_N\left(\mathbf{r}\right)=E\,\psi_N\left(\mathbf{r}\right), \tag{2.6}$$

where the quantity $V\left(\mathbf{r}\right)$ is the *interatomic potential*. Further step, if the paradigm is the *classical molecular dynamics*, the Schrödinger equation can be replaced by Newton equation.

2.2 Classical molecular dynamics

The evaluation of the thermal de Broglie wavelength [20],

$$\Lambda=\sqrt{\frac{2\pi\hbar^2}{mk_{\mathrm{B}}T}} \tag{2.7}$$

being m the atomic mass, T the temperature of the system, $\hbar$ the reduced Planck constant and k_{B} the Boltzmann constant, permits to discriminate between quantum and classical regime. Particularly, if that wavelength is smaller than the mean nearest neighbor separation ($\Lambda \ll a$), then the *classical approximation* is justified. For instance, the thermal de Broglie wavelength of a crystal of palladium atoms ($m = 106.42$amu) at room temperature ($T = 273.15$K) is $\Lambda \approx 0.1$Å, much smaller than the lattice parameter ($a = 3.890$Å), therefore legitimizing nuclei to be considered as classical particles. In general, quantum effects tend to be relevant for lightest atoms and/or coldest temperature. In fact, if equation 2.7 is applied to helium atoms ($m = 4.002602$amu) at $T = 4$K, then $\Lambda \approx 4.4$Å, too wide to neglect quantum effects.

If the adiabatic approximation holds, the time evolution of a set of interacting atoms (a many-body system) is obtained in the framework of *classical molecular dynamics* from the numerical solution of Newton's equations of motion, which conserve the total energy of the system $E = K + V$. The force acting on atom n is calculated as

$$\mathbf{F}_n=\dot{\mathbf{p}}_n=-\nabla_{\mathbf{r}_n}V\left(\mathbf{r}\right), \tag{2.8}$$

where $\dot{\mathbf{p}}_n$ is the time derivative of the momentum vector ($\mathbf{p}_n = m_n\dot{\mathbf{r}}_n$) and $\nabla_{\mathbf{r}_n}V\left(\mathbf{r}\right)$ the gradient of the interatomic potential.

2.2.1 Molecular dynamics algorithm

The starting point of a MD simulation is the generation of a plausible atomic structure $\mathbf{r}$ and velocity field $\dot{\mathbf{r}}$, typically drawn from a Maxwell-Boltzmann distribution [21, 22] at a given temperature. An interatomic potential $V(\mathbf{r})$ is then specified, together with a timestep δt for the numerical integration of equations of motion. The step is a crucial parameter to be selected since, if too small computer time is wasted, otherwise numerical instabilities arise causing the energy conservation and time-reversibility to fail. Therefore, as a general rule the timestep should be a couple of orders smaller than the reciprocal of the highest-frequency motion, *i.e.* usually of the order of 1fs.

Before iterating, it is often opportune to minimize the energy of the initial configuration, therefore migrating to a nearby local minimum of the potential energy surface.

The MD loop proceeds until the desired time t_e is reached, evolving from the starting configuration through an *equilibration phase* to the *production phase*, during which properties are calculated. At every iteration forces are computed according to equation 2.8 whereas velocities and positions are obtained integrating according to some finite difference method, *e.g.* the velocity Verlet algorithm [23], depicted at line 6 in algorithm 5.1.

Algorithm 2.1 Simplified molecular dynamics algorithm conserving total energy and implementing the velocity Verlet integrator.

1: $\mathbf{r}(t=0)$, $\dot{\mathbf{r}}(t=0)$, $V(\mathbf{r})$ and δt
2: (energy-minimize configuration)
3: $\mathbf{F}_n(t=0) = -\nabla_{\mathbf{r}_n} V(\mathbf{r}(t=0))$
4: **while** $t < t_e$ **do**
5: $\quad \mathbf{F}_n(t_{i+1}) = -\nabla_{\mathbf{r}_n} V(\mathbf{r}(t_{i+1}))$
6: $\quad \begin{cases} \dot{\mathbf{r}}_n(t_{i+1}) = \dot{\mathbf{r}}_n(t_i) + [\mathbf{F}_n(t_{i+1}) + \mathbf{F}_n(t_i)]\,\delta t/2m \\ \mathbf{r}_n(t_{i+1}) = \mathbf{r}_n(t_i)\,\delta t + \mathbf{F}_n(t_i)\,(\delta t)^2/2m \end{cases}$
7: $\quad t_i \leftarrow t_i + \delta t$
8: **end while**

2.2.2 Microstates and macrostates

A MD simulation results in a temporal sequence of $3N$ positions and $3N$ momenta, *i.e.* a *trajectory*. This is naturally described in the $6N$-dimensional *phase space*, each point corresponding to a *microstate*, *i.e.* a configuration of the system. The collection of points in phase space satisfying the constrains of a particular thermodynamic state (*macrostate*) is an *ensemble*, which is said to be in *statistical equilibrium* if it does not evolve over time. The most natural thermodynamic ensemble for MD, *i.e.* the one obtained from the solution of equation 2.8 and discussed so far, is the microcanonical ensemble (NVE) characterized by the number of atoms N, the volume of the system V and the total energy E to be fixed to a given value. Other thermodynamic ensembles are reported in table 2.1.

NVE	microcanonical [24]
NVT	canonical [24]
NPT	isothermal-isobaric [25]
NPH	isoenthalpic-isobaric [26]
μVT	grand-canonical [24]

Table 2.1: Thermodynamic ensembles. The acronym in the first column is constructed from corresponding fixed variables. N is the number of atoms, V the volume, E the total energy, T the temperature, P the pressure, H the enthalpy and μ the chemical potential.

The connection between microstates and macrostates (the thermodynamic observables) is operated by the tools of statistical mechanics. Experimentally accessible quantities are generally obtained by probing a huge number of atoms sampling many microstates and therefore the macroscopic behavior of the system can be calculated by averaging over the ensemble, *i.e.* by integrating over the phase space of the system. If the *ergodic hypothesis* [27] holds, then the system will evolve through all possible microstates over a *sufficient period of time* and the ensemble average will equal the time average,

$$\mathscr{A}_o = \langle \mathscr{A}\left(\mathbf{\Gamma}\left(t\right)\right)\rangle_{\mathrm{e}} = \langle A\left(\mathbf{\Gamma}\left(t\right)\right)\rangle_{\mathrm{t}} \tag{2.9}$$

where $\mathscr{A}_o$ is the observable of interest, $\mathbf{\Gamma}\left(t\right) = \left(\mathbf{r}\left(t\right), \mathbf{p}\left(t\right)\right)$ a point of the phase space ($6N$ variables) and angle brackets represent an average,

over the ensemble (e) or over time (t). The time average is constructed in the conventional way,

$$\mathscr{A}_o = \langle \mathscr{A}(\mathbf{\Gamma}(t)) \rangle_{\mathrm{t}} = \lim_{\tau \to +\infty} \frac{1}{\tau} \int_{t=0}^{\tau} \mathscr{A}(\mathbf{\Gamma}(t'))\, \mathrm{d}t' \approx \frac{1}{S} \sum_{t=0}^{S} \mathscr{A}(\mathbf{\Gamma}_t)\,. \tag{2.10}$$

being S the number of steps in the simulation.

2.2.3 The bulk-like system

It is often desirable to investigated properties of a *bulk system* which, in principle, should contain an infinite number of atoms and no surfaces. While this condition is rather unpractical to achieve in a MD simulation, nevertheless it can be mimicked implementing the *periodic boundary conditions (PBCs)* [28]. For simplicity, consider a simulation box (but the reasoning can be extended to other geometries [14]) described by edges $\{L_i, L_j, L_k\}$ replicated an infinite number of times to describe a periodic lattice completely filling space. The coordinates of the n-th atom in the i-th *image cell* are expressed by the relation

$$\mathbf{r}_n^{(i)} = \mathbf{r}_n + a_i L_i \hat{\mathbf{i}} + a_j L_j \hat{\mathbf{j}} + a_k L_k \hat{\mathbf{k}} \quad a_i, a_j, a_k \in \mathbb{Z} \tag{2.11}$$

where $\hat{\mathbf{i}}$, $\hat{\mathbf{j}}$ and $\hat{\mathbf{k}}$ are unit vectors codirectional with coordinate system. As an atom exits the original cell, one of its periodic images enters from an adjacent cell therefore conserving the number of elements.

Care must be taken when implementing the PBCs since some artifacts are introduced. The first intuitive consideration is that the size of the cell should exceed the interaction distance of the interatomic potential so that atom n does not interact with its own image. If this condition is not satisfied the symmetry of the cell is imposed on the system [13].
Secondly, the characteristic length of the investigated property should be smaller than the size of the cell since the maximum wavelength of the density waves (fluctuations) is related to the latter quantity. Low-frequency phonons and shock waves are affected, for example, and displacement fields can interact.

A detailed description of PBCs principles, together with a comprehensive overview of inherent possible artifacts are available *e.g.* in [13].

2.2.4 Remarks on the choice of the potential

The realism of a simulation extremely relies on the choice of the potential. Many alternatives exist, commencing with the simple Lennard-Jones (pair) potential [29], still employed because of its computational efficiency. When dealing with metals, a widely employed formalism is the embedded atom method (EAM) [30–33] or its modified version (MEAM) [34]. Within the class of bond order potentials, the reactive force field (ReaxFF)[35–38] permits bonds to be formed and broken, therefore allowing chemical reaction to take place. Next level of complexity, the electron force field eFF [39, 40], is a semiclassical approach which allows dealing with excited systems by representing electrons as Gaussian wave packets and nuclei as point charges.

Many more models for the interatomic potential exist, characterized by a different degree of accuracy and computational complexity. The choice of the optimal potential depends on the specific tackled problem (chemical composition and bonding, size and time scale, ...) and on the kind of information to be extracted (structural, chemical, ...).

To conclude, the size- and time-scale which can be simulated are continuously increasing, both because of the uninterrupted growth of computing power, both because of advances in methodology.

Of particular interest is the so-called *multiscale modeling*, which combines techniques characterized by different levels of accuracy (*e.g.*, quantum, atomistic, mesoscopic and continuum), each solving a specific part of the problem (see *e.g.* [41–44] and references therein).

2.3 Analysis of results

• ○ • ○ • *Part of this section has been adapted from [45–47].*
The availability of information at the atomic level (the trajectory) added up to the tools offered by statistical mechanics allow to compute an impressive amount of quantities (see *e.g.* [13]). The following discussion will be restricted to a concise set of definitions related to this work and mainly useful to assess the deviation of the structure of a solid state aggregate from its reference one, both in space and time.

Configuration

The *configuration* is the set of the positions $\mathbf{r}$ forming a body. The starting guess of the system, constructed according to some mathematical recipe, is called *as-built configuration*.

The *time-averaged configuration* of the quantity $\mathscr{A}(\mathbf{r}(t))$ has already been defined ($\langle \mathscr{A}(\mathbf{r}(t)) \rangle_{\mathrm{t}}$ in equation 2.10), whereas the *average-position configuration* is expressed as

$$\mathscr{A}_p = \mathscr{A}\left(\langle \mathbf{r}(t) \rangle_{\mathrm{t}}\right). \tag{2.12}$$

As will be shown, this quantity permits to remove dynamical features (atomic vibrations) so to single out the static displacement field.

2.3.1 Atomistic deformation

Deformation is the transformation from a reference configuration $\mathbf{r}_0$ to the present, deformed configuration $\mathbf{r}_{\mathrm{d}}$ (see *e.g.* [48]). The change in configuration results in an *atomic displacement*,

$$\mathbf{u} = \mathbf{r}_{\mathrm{d}} - \mathbf{r}_0, \tag{2.13}$$

independent of the choice of the reference frame and defining a *field*. This quantity is in general composed by (i) a rigid-body displacement (translation/rotation), preserving distances between atoms; (ii) a deformation, defined by a nonzero relative displacement between particles and therefore changing the shape and/or size of the body.

An immediate visual perception of the deviation from the reference configuration is offered by the displacement, which hereinafter is considered to be *relative*, free from any rigid-body motion. To treat *e.g.* surfaces, it is useful to extract the component of the atomic displacement projected on the plane described by the normal $\hat{\mathbf{p}}$,

$$\mathcal{P}^{\perp}_{\hat{\mathbf{p}}}(\mathbf{u}_n) = \mathbf{u}_n - (\mathbf{u}_n \cdot \hat{\mathbf{p}})\,\hat{\mathbf{p}} \tag{2.14}$$

and normal to the plane,

$$\mathcal{P}_{\hat{\mathbf{p}}}(\mathbf{u}_n) = (\mathbf{u}_n \cdot \hat{\mathbf{p}})\,\hat{\mathbf{p}}, \tag{2.15}$$

so that $\mathcal{P}^{\perp}_{\hat{\mathbf{p}}}(\mathbf{u}_n) + \mathcal{P}_{\hat{\mathbf{p}}}(\mathbf{u}) = \mathbf{u}_n$. Alternatively, the displacement can be projected onto a given vector like the case of coherent X-ray diffraction (CXD) imaging [49–51], $\mathbf{Q}\cdot\mathbf{u}_n$, where $\mathbf{Q}$ is the wavevector transfer (scattering vector) which will be introduced in chapter 3.

To get rid of any physical dimension the concept of *strain*, the normalized relative displacement, is also introduced. Because of deformation, atomic volume can be modified: a simple method to measure atomic volume is by calculating the Voronoi tessellation [52] of the atoms.

The average atomistic strain can be evaluated by computing the difference of bond length (the Euclidean norm of $\mathbf{r}_{nm} = \mathbf{r}_n - \mathbf{r}_m$, n being a nearest neighbor of m) and averaging the information over the number of nearest neighbors ($\mathcal{N}$),

$$\mathrm{b}_n = \frac{1}{\mathcal{N}_n} \sum_{m=1}^{\mathcal{N}_n} \|\mathbf{r}_{nm}\| \,. \tag{2.16}$$

The average strain of atomic bonds of a given atom n as seen by its nearest neighbors can therefore be expressed as

$$\varepsilon_{\mathrm{b},n} = \frac{\mathrm{b_d}}{\mathrm{b}_0} - 1. \tag{2.17}$$

To provide a "surface view" of the above quantity, $\mathcal{N}_n$ nearest neighbors are identified by drawing an annulus centered on the given atom in the reference (as-built) configuration, with mean radius equal to the first neighbors distance, and lying on the plane described by the normal versor $\hat{\mathbf{p}}$. The neighbor list computed in the previous step is then used to draw the vector connecting atoms n and m in the deformed configuration and the strain is again evaluated according to equation 2.17, representing in this case the average strain of a given atom n as seen by its nearest neighbors lying on the plane described by $\hat{\mathbf{p}}$.

Different views of the strain can be built considering the symmetry of the atomic aggregate. For example, the *radial strain*

$$\varepsilon_{r,n} = \frac{\mathbf{u}_n \cdot \hat{\mathbf{r}}_{cn}}{\|\mathbf{r}_{cn}\|}, \tag{2.18}$$

being $\mathbf{r}_{cn}$ the vector connecting the center of the sphere to position n, perfectly fits spherical symmetry.

2.3.2 Radial pair correlation function

The average number of atomic pairs separated by a distance r at time t is given by

$$p\left(r,t\right)=\frac{1}{N}\sum_{n=1}^{N}\sum_{\substack{m=1\\m\neq n}}^{N}\delta\left(\left\|\mathbf{r}_{nm}\left(t\right)\right\|-r\right), \tag{2.19}$$

being $\delta\left(x\right)$ the Dirac-delta function [53], which is practically computed by compiling a histogram of separations within each interval $r+\Delta r$. For an isotropic and homogeneous system having numeral density ρ, the radial pair correlation function (RPCF) is defined as (see *e.g.* [13, 16, 54, 55] for a more rigorous definition)

$$g\left(r\right)=\frac{1}{\rho N}\left\langle \sum_{n=1}^{N}\sum_{\substack{m=1\\m\neq n}}^{N}\delta\left(\left\|\mathbf{r}_{nm}\left(t\right)\right\|-r\right)\right\rangle_{\mathrm{e}}. \tag{2.20}$$

Since the number of particles within the spherical shell of radii r and $r+\mathrm{d}r$ is $4\pi r^{2}g\left(r\right)$, the integration over the region of the RPCF extending from r_{-} to r_{+}, provides an estimate of the *average number of nearest neighbors*,

$$\mathcal{N}=4\pi\int_{r=r_{-}}^{r_{+}}g\left(r'\right)r'^{2}\,\mathrm{d}r'. \tag{2.21}$$

Interestingly, the RPCF is related to an experimental accessible quantity, the *structure function* $S\left(Q\right)$, through a Fourier transform. Assuming an isotropic sample (a *powder*, described in section 3.2) composed of a unique chemical species [56–58],

$$g\left(r\right)=1+\frac{1}{2\pi^{2}r\rho}\int_{Q=0}^{\infty}Q'\left[S\left(Q'\right)-1\right]\sin\left(Q'r\right)\,\mathrm{d}Q', \tag{2.22}$$

where Q is the modulus of the wavevector transfer (scattering vector).

2.3.3 Mean squared displacement

The mean squared displacement (MSD) quantifies, at a given instant, the average extent of the deviation of the instantaneous configuration

$\mathbf{r}$ from a reference configuration, which can be either the *as-built* $\mathbf{r}_0$ or the *average-position* $\langle \mathbf{r}(t) \rangle_t$, like in this case,

$$\langle u(t)^2 \rangle = \frac{1}{N} \sum_{n=1}^{N} \| \mathbf{r}_n(t) - \langle \mathbf{r}(t) \rangle_{tn} \|^2 . \tag{2.23}$$

In other words, if dealing with the solid state of matter this quantity express the mean square amplitude of atomic oscillations. The MSD is in turn related to the (isotropic) *B-factor*, which appears in the Debye-Waller temperature factor [59, 60], by the time average of the MSD,

$$B_{iso} = \frac{8\pi^2}{3} \langle \langle u(t)^2 \rangle \rangle_t . \tag{2.24}$$

This quantity, roughly, expresses the reduction of the *scattered intensity* (see chapter 3) because of motion of atoms about their equilibrium positions.

Chapter 3

Atomistic approach to scattering

The physical principles of the interaction between X-rays and matter are discussed in many books. Among them, in my opinion, two *must-reads* are the one by Guinier [61] and the one by Warren [57]. Although they are not the most up-to-date references (original versions date back to, respectively, 1956 and 1968), nevertheless they gracefully provide an astonishing multitude of concepts essential to understand X-ray scattering. A sublime contemporary source introducing X-ray physics and covering a broad set of techniques is the book by Als-Nielsen and McMorrow [62]. The main goal of this book is to present developments in X-ray science after the introduction of synchrotron radiation sources, in the late seventies.

Anyway, all of them comprehensively piece together the theory commencing from the scattering of an X-ray by a single electron and subsequently building the signal elastically scattered by an *isolated* atom. To do so, electrons can be considered as classical particles and the (number) charge density $\rho(\mathbf{r})$ can therefore be defined. The field scattered from an atom, in the framework of the *first-order Born approximation* [63, 64], is then obtained superimposing the contribution from each volume element of the distribution itself. With reference to figure 3.1, let the *plane wave* described by the wavevector $\mathbf{k}$ impinge on the charge element $\rho(\mathbf{r})\,\mathrm{d}^3\mathbf{r}$, being $\mathbf{r}$ originated at the center of the atom. If the scattered wave is denoted by $\mathbf{k}'$, then the phase difference between the charge element at $\mathbf{r}$ and that at the origin is $\Delta\phi(\mathbf{r}) = (\mathbf{k} - \mathbf{k}')\cdot\mathbf{r} = \mathbf{Q}\cdot\mathbf{r}$,

being the wavevector transfer (scattering vector)

$$\mathbf{Q} = \mathbf{k} - \mathbf{k}'. \tag{3.1}$$

If the scattering event is elastic, then $\|\mathbf{k}\| = \|\mathbf{k}'\|$ and therefore $Q = \|\mathbf{Q}\| = 2\,\|\mathbf{k}\| \sin\Theta = (4\pi/\lambda)\sin\Theta$.

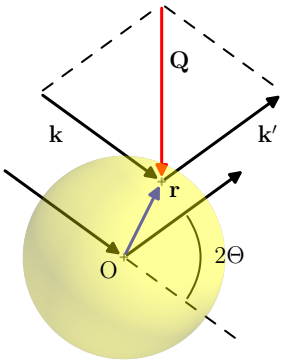

Figure 3.1: An X-ray impinging with wavevector $\mathbf{k}$ on the charge element of an isolated atom at position $\mathbf{r}$ is elastically scattered to $\mathbf{k}'$. Geometrical definition of the wavevector transfer ($\mathbf{Q}$) and of the scattering angle (2Θ) is also shown.

The integration of the contribution of each volume element to the scattered field engender the definition of the atomic form factor,

$$f_0(\mathbf{Q}) = \int_0^\infty \rho(\mathbf{r}) \exp(\imath \mathbf{Q}\cdot\mathbf{r})\, \mathrm{d}^3\mathbf{r} = \mathcal{F}_{\mathbf{Q}}[\rho(\mathbf{r})](\mathbf{Q}), \tag{3.2}$$

i.e. the Fourier transform of the charge density. By virtue of the quantum mechanics nature of electrons, the atomic form factor actually depend on the energy of the incoming beam,

$$^{\dagger} f(\mathbf{Q}, \hbar\omega) = f_0(\mathbf{Q}) + f'(\hbar\omega) + \imath f''(\hbar\omega), \tag{3.3}$$

where f' and f'' are the dispersion corrections to f_0. Often in X-ray diffraction (XRD) data interpretation *spherical symmetry* is invoked

[†]The dependence on the energy will not be explicitly indicated hereinafter

to simplify the non resonant term (equation 3.2) of $f(\mathbf{Q}, \hbar\omega)$, which can then be expanded as [65]

$$f_0(Q) = \sum_{i=0}^{4} a_i \exp\left(-b_i \left[\frac{Q}{4\pi}\right]^2\right) + c \tag{3.4}$$

Theory and tables for atomic form factors can be found *e.g.* in [62, 64–66] and analogous quantities exist for the interaction of neutrons and electrons with matter.

3.1 Intensity scattered by an atomic aggregate

Extending the reasoning carried out for the isolated atom to an atomic aggregate (molecule) composed of N atoms, *e.g.* the one in figure 3.2, the structure factor can be expressed as

$$F(\mathbf{Q}) = \sum_{n=1}^{N} f_n(\mathbf{Q}) \exp(\imath \mathbf{Q}\cdot\mathbf{r}_n), \tag{3.5}$$

being the nucleus of the n-*th* atom connected to the reference frame by the vector $\mathbf{r}_n$ and f_n its form factor.

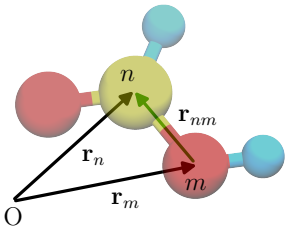

Figure 3.2: Formic acid molecule. Nucleus of the carbon atom (yellow) is connected to the origin of the reference frame (O) by vector $\mathbf{r}_n$.

Normally, and this is the founding principle of the so-called *reciprocal-space (RS) approach*, next step is to exploit a proper unit cell so to express the *crystal structure factor*.

However, last step can be avoided and the atomic aggregate considered to be a *single molecule* rather than a tiny crystal [67]. The quantity effectively probed during an experiment is the intensity distribution (figure 3.3), *i.e.* the structure factor times its complex conjugate

$$\begin{aligned} I(\mathbf{Q}) &= F(\mathbf{Q})\, F^*(\mathbf{Q}) \\ &= \sum_{n=1}^{N} f_n(\mathbf{Q}) \exp(\imath \mathbf{Q}\cdot\mathbf{r}_n) \sum_{m=1}^{N} f_m^*(\mathbf{Q}) \exp(-\imath \mathbf{Q}\cdot\mathbf{r}_m) \\ &= \sum_{n=1}^{N}\sum_{m=1}^{N} f_n(\mathbf{Q})\, f_m^*(\mathbf{Q}) \exp(\imath \mathbf{Q}\cdot\mathbf{r}_{nm}), \end{aligned} \tag{3.6}$$

being $\mathbf{r}_{nm} = \mathbf{r}_n - \mathbf{r}_m$, *i.e.* the vector connecting atoms n and m.

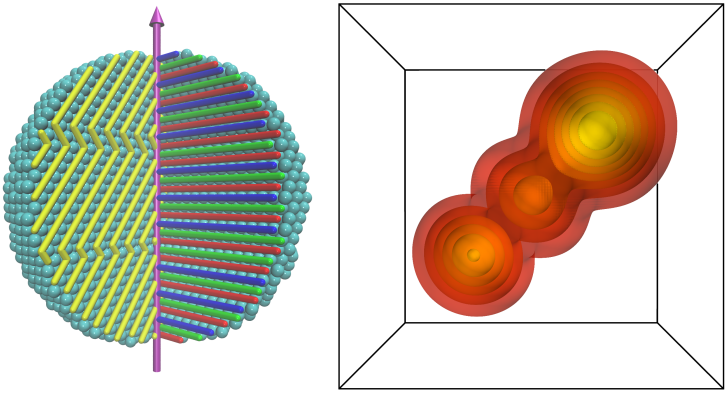

Figure 3.3: Portion of a small palladium spherical crystal showing a deformation and a twin fault. Purple arrow coincide with the (111) direction and yellow cylinders are drawn to guide the eye. Red, Green and Blue indicate, respectively, position of layers A, B and C (left). Intensity distribution (isosurfaces) around $(1\bar{1}1)$ RS point calculated from equation 3.6 (right).

Once the intensity distribution is built, any experiment can in principle be emulated (generally by integration of intensity distribution on a given surface in RS), the more direct one being a CXD measurement.

3.2 Powder average of the intensity

• ○ • ○ • *Part of this section has been adapted from [47, 68, 69].*
Let the molecule sketched in figure 3.4 rotate with respect to the incoming beam, taking every possible orientation with equal probability. Relative atomic positions are fixed and the motion is rapid enough that only the average scattered intensity is observed.

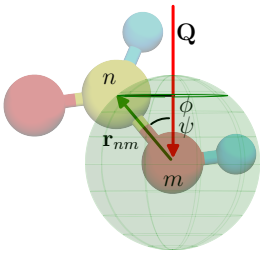

Figure 3.4: The head of the (green) vector connecting atom m to n ($\mathbf{r}_{mn}$) takes with equal probability every possible orientation with respect to the wavevector transfer ($\mathbf{Q}$) drawing the green spherical surface. Polar (ψ) and azimuthal angle (ϕ) are also indicated.

During its motion, the head of the vector $\mathbf{r}_{nm}$ spawns the spherical surface in figure 3.4. Mathematically, the powder average of the intensity distribution is expressed by the *orientational (spherical) average* of equation 3.6 (assuming spherically symmetric atomic form factor),

$$\langle I\left(\mathbf{Q}\right)\rangle_o = \sum_{n=1}^{N}\sum_{m=1}^{N} f_n\left(Q\right) f_m^*\left(Q\right) \langle \exp\left(\imath \mathbf{Q}\cdot\mathbf{r}_{nm}\right)\rangle_o. \tag{3.7}$$

The result of the spherical average of the exponential term in the equation above,

$$\langle \exp\left(\imath \mathbf{Q}\cdot\mathbf{r}_{nm}\right)\rangle_o = \frac{\displaystyle\int_{\phi=0}^{2\pi}\int_{\psi=0}^{\pi} \exp\left(\imath Q r_{nm}\cos\psi\right) r_{nm}^2 \sin\psi \;\mathrm{d}\phi\,\mathrm{d}\psi}{\displaystyle\int_{\phi=0}^{2\pi}\int_{\psi=0}^{\pi} r_{nm}^2 \sin\psi\,\mathrm{d}\phi\,\mathrm{d}\psi}, \tag{3.8}$$

leads to the definition of the Debye scattering equation (DSE), derived for the first time by Debye in 1915 [70],

$$I(Q) = \sum_{n=1}^{N} \sum_{m=1}^{N} f_n(Q) f_m^*(Q) \operatorname{sinc}(Q r_{nm}) . \tag{3.9}$$

Therefore, the powder average of the intensity distribution depends only on the magnitude of the interatomic distances (r_{nm}) and not on their mutual orientations.

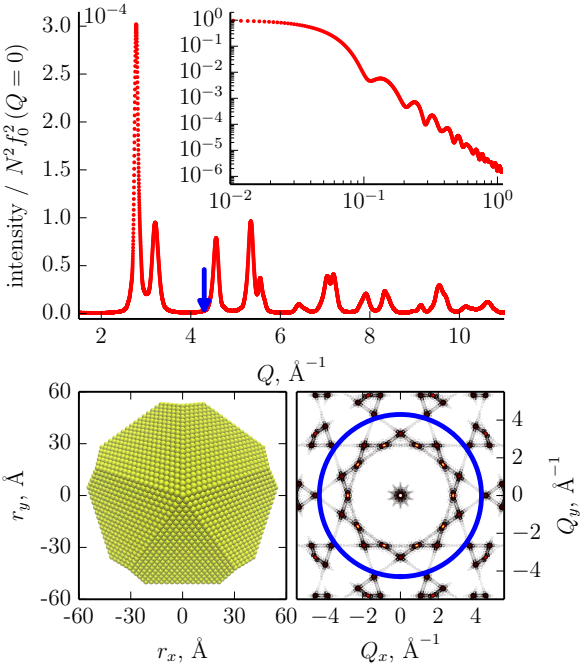

Figure 3.5: The DSE (red) applied to a palladium Marks decahedron (bottom, left), normalized over the squared number of electrons, *i.e.* $N^2 f_0^2(Q=0)$. *Small angle* region of the pattern is reported in the inset (log-log plot). The blue arrow indicates the position of the *powder diffraction sphere* at a given Q-value drawn in the $Q_z = 0$ RS cross-section (same color; bottom, right).

The RS view of the procedure used to deduce the DSE lies in a *(spherical) surface integral* (*powder diffraction sphere*, depicted in figure 3.5) of the intensity distribution. Traditionally, this procedure is simplified by the tangent plane approximation [71] invoking the argument that intensity distribution is concentrated around RS points (see *e.g.* [47] and references therein).

3.2.1 Computational aspects

One of the major limitations to a broad application of the DSE has been its computational requirements. Indeed, the number of calculations for a given value of wavevector transfer equals the squared number of atoms.

Several methods have been proposed to mitigate computational requirements. In the pioneering work of Germer and White (1941) on electron diffraction [72], the pattern for a powder of particles made of 55 atoms was obtained by manual calculations, exploiting crystal symmetry. Particularly, they recasted the DSE for a monoatomic fcc crystal as

$$I(x) = \sum_{n=0}^{pairs} B_n f^2(x) \operatorname{sinc}\left(x\sqrt{n}\right), \tag{3.10}$$

$x = \pi\sqrt{2}Ra_0/L\lambda$ being a function of the electron wavelength (λ), unit-cell parameter (a_0) and other experiment-dependent features (L is the specimen-plate distance, R the abscissa of the microphotometer curve). The term B_n is twice the number of atom pairs having the separation $a_0\sqrt{n/2}$ in the crystal, with $B_0 = N$. Germer and White accomplished to compute the DSE of even larger particles (up to 379 atoms, which corresponds to a spherical copper crystal described by a diameter of 20.4Å) by introducing the approximation, for large values of N, $B_n = Nb_n\epsilon_n$. The term $b_n = a_0\sqrt{n/2}$ is the number of atoms at a given distance in an infinite fcc crystal and ϵ_n, which lies in the range $0 \leq \epsilon_n \leq 1$, accounts for the shape of the crystal.

In 1980 Glatter proposed the so-called *distance histogram approximation* to drastically weaken the computational complexity [73]. To do so, distances between particles are grouped in discrete bins, each

containing $p(r_k)$ values, leading to the following variant of the DSE

$$I(Q) = f^2(Q) \sum_{k=1}^{bins} p(r_k) \operatorname{sinc}(Q\, r_k) . \tag{3.11}$$

A further step forward was the adoption of a fast Fourier transform (FFT) algorithm in place of the explicit summation, as proposed by Hall and Monot in 1991 [74], elegantly improved by Cervellino and colleagues who proposed a clever method to obtain a continuous distribution function of distances by smoothing the RPCF with a Gaussian function. This function is then re-sampled with a constant step, so that the FFT can be efficiently used to generate the powder pattern. The Gaussian smoothing can be easily removed via multiplication by an inverse function.

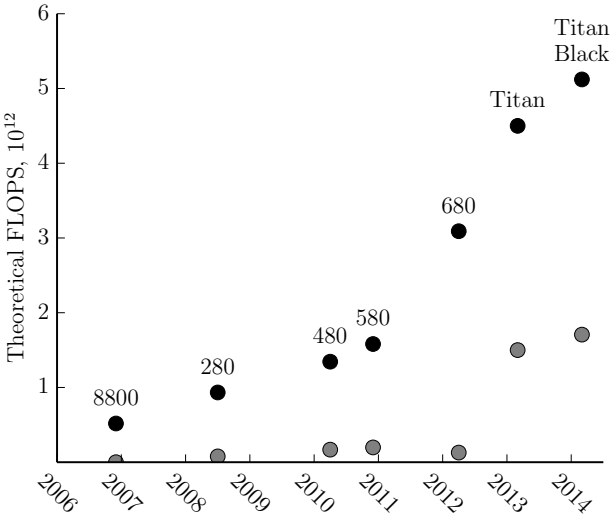

Figure 3.6: Theoretical single-precision (black dot) and double-precision (gray dot) peak performances (FLOPS) of some NVIDIA® GeForce GTX GPUs (data computed from specifications in [75]).

The tremendous computational power of GPUs has been exploited to allow the application of the original formulation of the DSE [68, 69]: the *embarrassingly parallel* nature of equation 3.9 perfectly fits the *data-parallel* vocation of GPUs. No approximation (apart from those inherent in the use of floating point math) is therefore enforced and the DSE can be safely applied to any type of atomic aggregate. The theoretical number of FLOPS of modern graphics cards, reported by figure 3.6 for some selected devices, outperform the throughput of central processing units (CPUs) and the growth rate of their computing power in the last half decade is impressive. To be included in the list of advantages, the modest power consumption (and relatively low price) of GPUs allows multiple devices to be hosted by a single desktop computer. Some technical details of processing units hosted by the personal computer used to calculate patterns presented in this chapter are reported in table 3.1. Although the *theoretical* number of FLOPS is just a rough indicator of computing power of processing units, nevertheless it offers a fair indication of achievable performances.

	cores	SP FLOPS	DP FLOPS	TDP, W
GPU [75]	2,880	†5,121	†1,707	250
x2	5,760	10,242	3,414	500
CPU [76]	4	‡243	‡122	95

† (2SP or 2/3DP)(FLOPS/cycle)(clock rate)(cores)
‡ (16SP or 8DP)(FLOPS/cycle)(clock rate)(cores)

Table 3.1: Technical details of the central (Intel® Core™ i7-2600K) and graphics (2 NVIDIA® GeForce GTX TITAN Black) processing units on the desktop computer used to calculate diffraction patterns presented in this chapter. Quantities shown here are the number of theoretical FLOPS when performing single precision (SP) and double precision (DP) operations. The thermal design power (TDP), a conventional figure used to express the thermal load generated by a given device and therefore proportional to the peak power consumption, is also reported.

To reduce even more computational time, the software proposed in [68, 69] also exploits the message passing interface (MPI) [77], so as to employ graphics cards plugged on different computers.

3.3 Interference in a scattering experiment

> The methods of Debye [70] are accepted in the scattering of electrons by gases, but despite the application to thin films by Germer and White [72] their use in kinematic electron diffraction from polycrystalline solids has seemed suspect and none of the recent texts on electron diffraction mention the methods. [...] The objection to the Debye theory is that it neglects interference between atoms situated in different crystals; while this is permissible for a gas of large molecules, it requires justification if the molecules (or small crystals) are densely packed.
>
> C.W.B. Grigson, 1967 [78]

• ○ • ○ • *Part of this section has been adapted from [45].*
In section 3.2, the DSE has been derived envisaging a particle *rotating* so to take every possible orientation with equal probability. Yet, this condition would be difficult to encounter in a real scattering experiment. Imagine notwithstanding a *large ensemble of copies* of the very same atomic aggregate *randomly directed* and *arranged* in space, as the one depicted in figure 3.7. If it was possible that the elements of the collection scatter *independently*, without any kind of *interference*, then it can be demonstrated that the signal scattered by the ensemble exactly equals the output of the DSE applied to a single element multiplied by the number of items in the collection. This important result, which strictly speaking only applies if copies are separated by an *infinite* length, guarantees equation 3.9 to be applied to real case studies.

3.3.1 Coherence and correlation

Interference among scattering domains causes specific features to appear[79–84], which modify the traditional concept of crystallite. As shown by Rafaja and colleagues [79, 80, 82, 83], those effects are clearly visible when (i) the scattering domains are sufficiently small and (ii) strongly textured. Effects of interference were observed in nanocrystalline thin films deposited by physical vapor deposition (PVD) [80, 82, 83], and has also been proposed in ball milled powders [81].

The general understanding of this effect is that when intensity distribution from different crystallites overlap in RS, the observed line profiles tend to sharpen, the peak width being related to a larger size than that of the single domains. Effects tend to be observed more at low diffraction angle, corresponding to RS points closer to the origin.

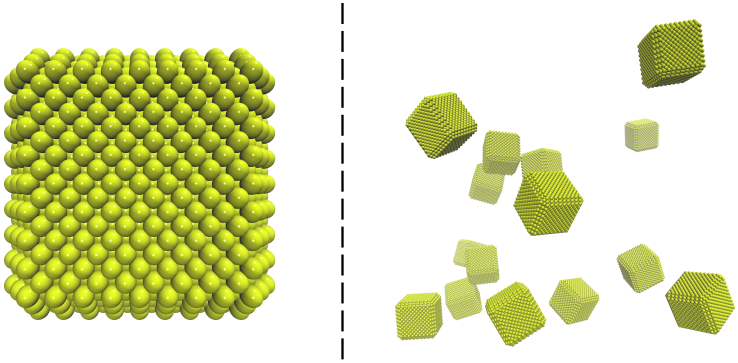

Figure 3.7: On the right, a large ensemble of copies of the atomic aggregate drawn on the left, randomly oriented and arranged, separated by an infinite distance.

Interference in a scattering experiment results either from properties (i) of the beam (*coherence*) and (ii) of the sample (*correlation*). An interesting discussion on their interplay is given in [85] and [86].

3.3.1.1 Coherence

The coherence lengths express the deviation of a real beam from an ideal one both in terms of divergence (*spatial coherence length*) and energy spread (*temporal coherence length*). Coherence depends on the source and optics (*i.e.* the measurement apparatus), and defines an upper limit for interference effects to be observable: for distances smaller than the coherence length amplitudes add up, otherwise intensities add up. The *coherence volume* delimits the largest region for interference among waves to arise *within a given crystal* and in the terminology of powder diffraction is commonly referred as *instrumental resolution*.

3.3.1.2 Correlation

The correlation lengths are related to inhomogeneity of the specimen (size and defects) and define the concept of *crystallite*, *i.e.* a coherently scattering domain (where scattered waves are in phase). In the simplified model of *ideally imperfect crystal*, or *mosaic*, first introduced by Darwin in 1922 [87], a real crystal is though of as if composed of many perfect-crystal blocks, slightly misoriented with respect to each other. Interference only occurs inside each block (crystallite), whose size therefore defines the correlation length, and not among waves diffracted from different domains. Thus, the scattered intensity from the whole mosaic equals the sum of intensities diffracted by each block (at least in the wide angle region if the correlation volume is infinite, as it will be assumed to be hereinafter) as it is demonstrated in figure 3.8c.

Imagine partitioning the perfectly crystalline cubic domain depicted in figure 3.8a in blocks (*grains*) and then rotating them by a given angle about a randomly oriented axis. If the misalignment is sufficiently large and random, as in figure 3.8c, then each grain in the *polycrystalline aggregate* will scatter incoherently, as in the mosaic model and the width of each diffraction peak (and in turn, the correlation length) will be related to the average size of the block. Indeed, as demonstrated by the powder diffraction pattern in figure 3.8c, the diffracted intensity from the whole mosaic equals the sum of the intensities scattered by each grain when considered as an isolated object.

The other extreme behavior is observed when blocks are not misaligned at all, and they will obviously scatter coherently and the width of the diffraction peak will be related to the size of a larger object, the cubic domain itself illustrated by figure 3.8a.

Intermediate misalignments, as shown in figure 3.8b, cause intensity scattered from different blocks to overlap in RS in such a way that the concept of crystallite becomes apparently dependent on the magnitude of the wavevector transfer modulus.

Shifting from the perfect crystalline aggregate depicted in figure 3.8a to the mosaic model in figure 3.8c can be accomplished (i) by rotating blocks and/or (ii) by displacing their centroids.

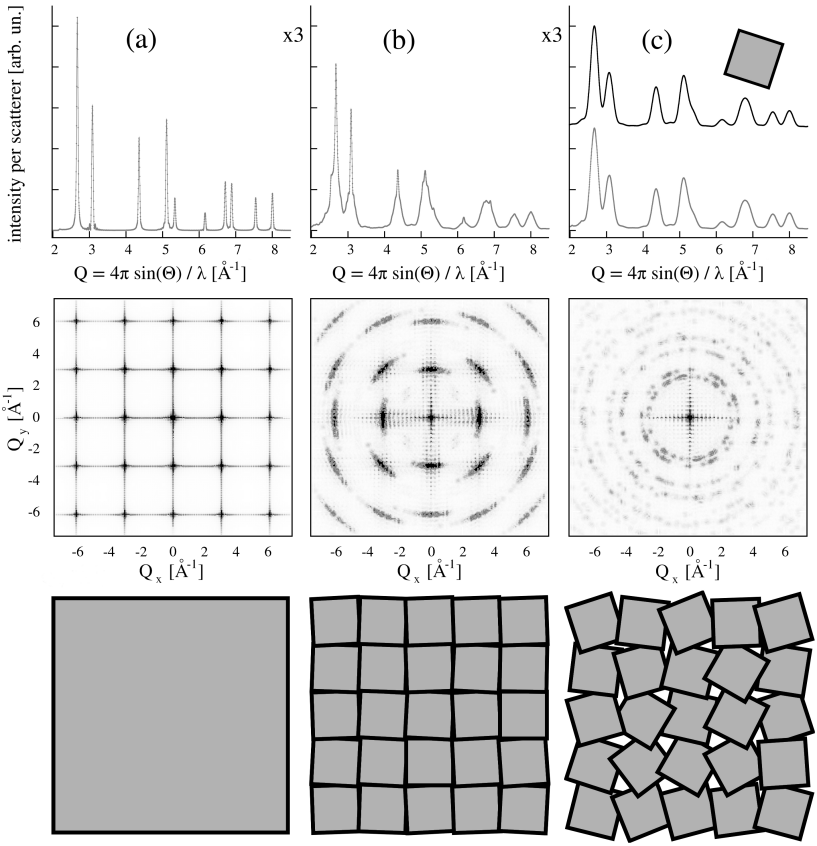

Figure 3.8: Cross-section of the intensity distribution in RS (equation 3.6) with $Q_z = 0$ (middle) for a fcc gold cube (a = 4.078 and implementing an appropriate form factor) (a), same object partitioned in slightly tilted smaller cubes (b) and same cubes strongly misaligned (c). The corresponding powder diffraction pattern is also drawn (top), the dotted curve in (c) showing the sum of the intensities scattered by each cube when considered as an isolated object. *Adapted from [47].*

Effect of rotation From a phenomenological point of view, the effect of rotation is summarized by figure 3.8 which leads to three intuitive considerations.

First of all, the probability of intensity overlapping in RS is proportional to the size of its distribution and therefore to the inverse of the crystallite size. The smaller the grain, the higher the probability of intensity overlapping, and thus the stronger the effect on the scattering pattern. For the sake of discussion, above argument can be expressed considering the Scherrer equation [88, 89], expressed in RS as,

$$\Delta Q \approx \frac{2\pi}{D}, \tag{3.12}$$

where, roughly, ΔQ is the broadening of the intensity distribution due to finite size of a sphere of diameter D.

Secondly, rotating two lattices in direct-space (DS) implies the rotation of their corresponding reciprocal lattices around a common center, the RS origin. Therefore, the smaller the angle θ between crystallites, the higher the overlapping probability. The last consideration is useful to understand how the effect of misorientation affects scattered intensity as a function of the momentum transfer Q.

Lastly, for a given misorientation degree, the overlapping volume becomes smaller by moving away from the RS origin since the arc length s (actually, the great-circle distance on the surface of a sphere) of equivalent points belonging to different reciprocal lattices increases linearly with the momentum transfer,

$$s = \theta Q. \tag{3.13}$$

To keep the discussion simple, assume that the arc length can be approximate by the chord d. Then, the common volume between two spherical distributions of intensities of diameter ΔQ is,

$$\Omega\left(\Delta Q, d\right) = \frac{\pi}{12}\left(2\Delta Q + d\right)\left(\Delta Q - d\right)^2 \quad d \leq \Delta Q, \tag{3.14}$$

and, after substituting equation 3.12 and equation 3.13,

$$\Omega\left(D, \theta, Q\right) \approx \frac{\pi}{12}\left(\frac{4\pi}{D} + \theta Q\right)\left(\frac{2\pi}{D} - \theta Q\right)^2 \quad \theta Q \leq \frac{2\pi}{D}, \tag{3.15}$$

which summarizes discussed concepts.

Effect of displacement To understand the effect of displacement on correlation it is better to recast the structure factor. Suppose that the atom n, placed at $\mathbf{r}_n$, belongs to grain p, connected to the (global) reference frame by the vector $\mathbf{R}_p$. Then, the position of n in the (local) reference frame anchored to the centroid of p can be expressed as $\mathbf{r}_{pn} = \mathbf{r}_n - \mathbf{R}_p$, as sketched in figure 3.9. This relation leads to the following definition of the structure factor (see equation 3.5),

$$F(\mathbf{Q}) = \sum_{p=1}^{M} \exp(\imath \mathbf{Q}\cdot\mathbf{R}_p) \sum_{n=1}^{N_p} f_n(\mathbf{Q}) \exp(\imath \mathbf{Q}\cdot\mathbf{r}_n), \tag{3.16}$$

where the innermost sum accounts for the internal structure of each grain, containing N_p atoms, and the outermost one spans the number of grains in the aggregate. The system sketched in figure 3.9, an ensemble of equally sized cubes, is designed to enhance the contribution of interference effects. If there is neither misorientation nor displacement of lattices inside grains, then they will form a perfect fcc crystal structure. Therefore, the summation over the number of grains in equation 3.16 is maximum (of the order of M) when block centroids are in phase, *i.e.* $\mathbf{Q}\cdot\mathbf{R}_p = 2\pi k \;\forall\; k \in \mathbb{Z}$, otherwise is of the order of unity.

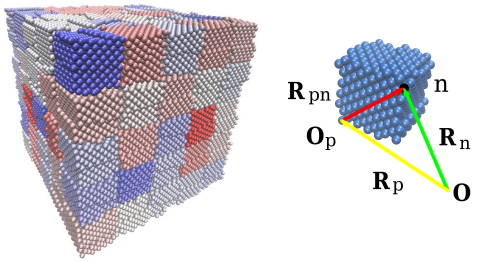

Figure 3.9: Atomistic model (125 grains, average block edge 2.45nm); colors are chosen randomly to help individuating grains (left). Position vectors connecting atom n to the global O and local O_p reference frame. *Adapted from [45].*

3.3.2 Uncorrelated crystallites

To assess the effect of misorientation on a powder diffraction pattern, the lattice inside each block in the idealized model in figure 3.9 is allowed to rotate about its geometrical center by a quantity expressed in terms of Euler angles $(\alpha, \beta, \gamma) \in \{(-\pi, \pi], [-\pi/2, \pi/2], (-\pi, \pi]\}$, using the x-convention. Those were sampled from a three-variate Gaussian distribution centered in $(0, 0, 0)$ and having variances $(\sigma, \sigma/2, \sigma)$ for the three (assumed uncorrelated) angles respectively: a strong *local texture* is therefore introduced. Lattices can also be displaced by a quantity sampled from a three-variate Gaussian distribution. Pseudo-random numbers were drawn from the "ranlux" [90] generator, implemented in the Gnu Scientific Library [91]. Rotations and translations are normalized to $\pi/2$ and the unit cell parameter, respectively, therefore defining the *misorientation degree* so to account for periodicities.

An analogous reasoning to the one used to derive equation 3.16 can be applied to the DSE, leading to the following result for the intensity scattered by a polycrystalline aggregate like the one in figure 3.9,

$$\begin{aligned} I(Q) &= \sum_{p=1}^{M}\sum_{q=1}^{M}\left[\sum_{n=1}^{N_p}\sum_{m=1}^{N_q} f_n(Q)\, f_m^*(Q)\,\mathrm{sinc}(Q\, r_{nm})\right] \\ &= \sum_{p=1}^{M}\left[\sum_{n=1}^{N_p}\sum_{m=1}^{N_p} f_n(Q)\, f_m^*(Q)\,\mathrm{sinc}(Q\, r_{nm})\right] \\ &+ \sum_{p=1}^{M}\sum_{\substack{q=1\\ q\neq p}}^{M}\left[\sum_{n=1}^{N_p}\sum_{m=1}^{N_q} f_n(Q)\, f_m^*(Q)\,\mathrm{sinc}(Q\, r_{nm})\right] \\ &= \sum_{p=1}^{M}\omega_p(Q) + \sum_{p=1}^{M}\sum_{\substack{q=1\\ q\neq p}}^{M}\chi_{pq}(Q) = \Omega(Q) + X(Q)\,. \end{aligned} \tag{3.17}$$

It should be noticed that, the consequence of feeding the DSE with this kind of aggregate, is effectively equivalent to introduce a *local texture* (because of the powder average) which exists in multiple places

within the specimen. In the above equation, the *self-correlation* function (Ω) represents the part of the intensity scattered by atoms inside grain p when considered as an isolated object (ω_p), whereas the *cross-correlation* function is the result of the interference of each atom in domain p with each other atom in the aggregate q (χ_{pq}). If grains are *uncorrelated* (they scatter independently, as in the mosaic model) than the equation $X(Q) = 0$ must be satisfied for all Q. An example of the above-defined functions is reported in figure 3.10.

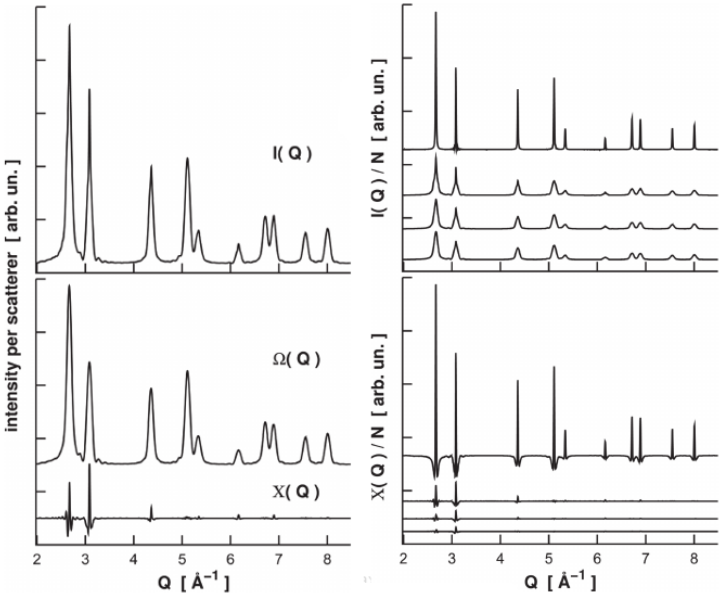

Figure 3.10: Left, Example of total intensity I, self- Ω and cross- X correlations for a polycrystalline aggregate composed of $5 \times 5 \times 5$ grains, rotated with a variance $\sigma = 5$ degrees. Each grain is approximately a (gold) cube characterized by an average edge of 3.67nm (9 unit cells). Right, intensity and cross-correlation for an ensemble of blocks with average edge 6.12nm (12 unit cells) not misaligned (top) and rotated, from top to bottom, by $\sigma = 3$, 6 and 9 degrees. In both cases curves are shifted vertically for clarity. *Adapted from [45].*

To roughly quantify how correlation is modified while playing with the model in figure 3.9, the *cumulative correlation parameter*, condensing the deviation of the observed intensity from that scattered by the corresponding mosaic model, is introduced

$$\nu\left(Q_i, Q_f\right) = \int_{Q_i}^{Q_f} \left|X\left(Q'\right)\right| \, \mathrm{d}Q' \Big/ \int_{Q_i}^{Q_f} \Omega\left(Q'\right) \, \mathrm{d}Q' \, . \tag{3.18}$$

The absolute value of X was considered to emphasize correlation effects, which otherwise could cancel as an effect of summing negative and positive values. The normalization factor, *i.e.* the intensity scattered from the same aggregate when grains are separated by an infinite distance (which corresponds to the mosaic model), allows for the comparison of patterns from different polycrystalline systems.

To assess the dependence of the cross-correlation as a function of (i) the misorientation degree and (ii) the size of the blocks, several gold (a = 4.078Å) systems have been simulated. Due to the statistical nature of the model, the effect of changing (iii) the number of grains in the aggregate has also been investigated. Indeed, intuitively, (iii.a) the larger the number of blocks, the better (more continuous) the representation of the "texture" (values are drawn from probability distributions). The reciprocal view of the above consideration is that the overlap of points in RS tends to be more uniform (*i.e.*, less subject to fluctuations) by increasing the number of grains. Moreover, (iii.b) correlation in this model is enhanced by increasing the number of domains: if all blocks are correctly oriented and not displaced (no misorientation) they will form a bigger coherently scattering aggregate.

The cumulative correlation parameter is reported in figure 3.11a against misorientation degree for aggregates composed by 8, 64, 216 and 512 blocks. The bar represents the relative standard deviation (the standard deviation normalized to the mean) of two models characterized by same misorientation degree but obtained using different sets of random numbers. As shown by the narrowing of the bars, by increasing the number of blocks models tend to be less sensitive to the random sequence. The trend of ν as a function of grains rotation, displacement or by a combination of the two is shown in figure 3.11b which

demonstrates that the most effective way of obtaining a mosaic model starting from a single domain is by implementing a combination of displacement and rotation.

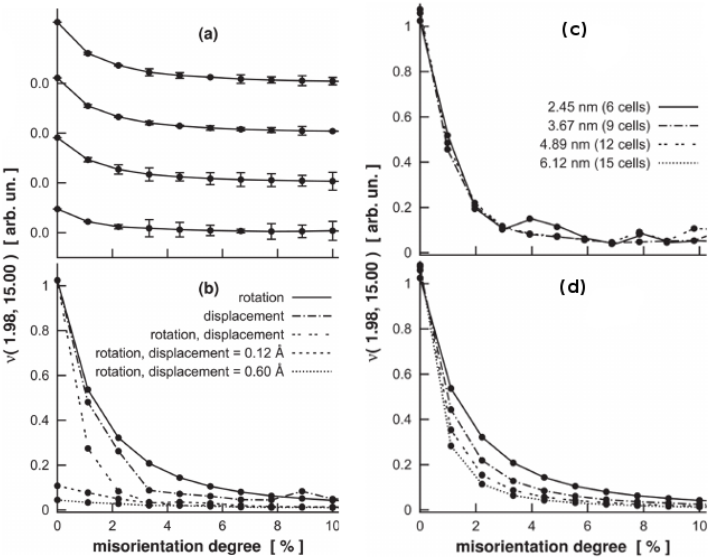

Figure 3.11: Left, trend of the cumulative interference parameter (equation 3.18, computed excluding the small-angle region, from $Q = 1.98$ to 15Å^{-1}) as a function of the misorientation degree for (a) different number of grains (average edge size 6.12nm) composing the polycrystalline aggregate (8, 64, 216, 512; decreasing from top to bottom) and different type of disorder (6.12nm, 125 grains). Curves in (b) represent the effect of pure rotation, pure displacement, and a combination of rotation and displacement or of a rotation with a fixed variance for displacement. Right, trend of the cumulative interference parameter as a function of the misorientation degree for different grain size (125 blocks) for the case of (c) pure displacement and (d) pure rotation. *Adapted from [45].*

As already discussed, the bigger the block, the narrower the spread of the intensity distribution in RS. Therefore, when grains are rotated, the smaller the grain size, the higher the probability of intensity over-

lapping. The concept is depicted in the right part of figure 3.11, where the trend of the cumulative interference parameter versus the rotation angle and the displacement is reported. Indeed, it is only the rotation which enforces a dependency of ν on the grain size, whereas the displacement does not affect the correlation parameter.

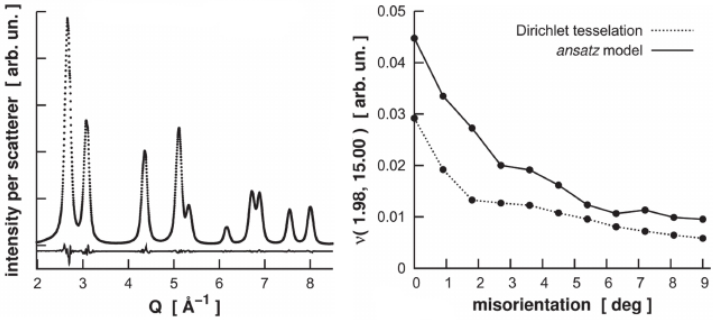

Figure 3.12: Right, intensity computed from the Dirichlet model (rotation with $\sigma = 3$ degrees) together with the cross-correlation function (below). Left, trend of the cumulative interference parameter as a function of the misorientation degree for the simplified model made of cubic blocks (solid line) and for the one obtained by Dirichlet tessellation (dash line). The size of the external box (12.23nm) and the number of grains (125) is the same for the two models. *Adapted from [45].*

The model so far investigated was conceived to explore correlation effects, and is therefore built to maximize it when there is no misorientation. It is legitimate to ask to what extent those effects can be observed in more realistic microstructures. An insight in this non trivial problem was obtained by seeding a cube with 125 random-placed nuclei and then tesseling space using the Dirichlet algorithm [92]. The resulting microstructure bears no regularity in the centers of mass of the grains, randomly distributed and positioned inside the box which preserves the cubic shape, while each grain lattice share the same orientation. As can be demonstrated by figure 3.12, with a suitable choice of parameters the results for the two models are comparable, thus supporting the conclusion that the *ansatz* is effectively capable to capture

main features related to misorientation.

As a final consideration, the beam in a typical laboratory powder diffraction measurement can be imagined as if composed by many coherent volumes. The total detected intensity could therefore be approximate as an *ensemble average* over systems like those discussed, inducing a further smoothing of interference features. However, the size of the coherence volume when employing synchrotron radiation can be sufficiently large to include the entire sample, therefore allowing features discussed to be investigated even for a powdered sample.

3.4 Demonstration of the paradigm

• ○ • ○ • *Part of this section has been adapted from [69].*
To demonstrate the flexibility of the DS approach, some considerations on the structure of graphite oxide (GO) dispersed in water are discussed. GO is a nonstoichiometric layered material consisting of graphene sheets bearing epoxy and hydroxyl groups on their basal planes and edges (see, *e.g.* [93, 94]). This causes GO to be hydrophilic and the interlayer separation to increase when increasing the water content [95].

A glass capillary was filled with a dispersion of GO, produced by the Hummers method [96], in water. Using a photon beam characterized by an energy of 10keV, a scattering pattern was collected, reported in figure 3.13. Although data are unfortunately modified by a set of aberrations affecting the experimental setup and therefore can not be properly modeled, nevertheless they can be used to demonstrate the DS approach.

The pattern reported in figure 3.13 shows three main features. The (i) two peaks at $Q \approx 5.1$ and $Q \approx 2.9\text{Å}^{-1}$ are associated, respectively, to graphene in-plane distances of $d = 1.23$ and $d = 2.13\text{Å}$.
The output of the DSE applied to a graphene layer is shown in figure 3.14, explaining reflections in (i). The broad peak in (ii) arises from the superposition of the signal from the glass capillary and water, which can be easily added to the atomistic model. Lastly, the reflection in

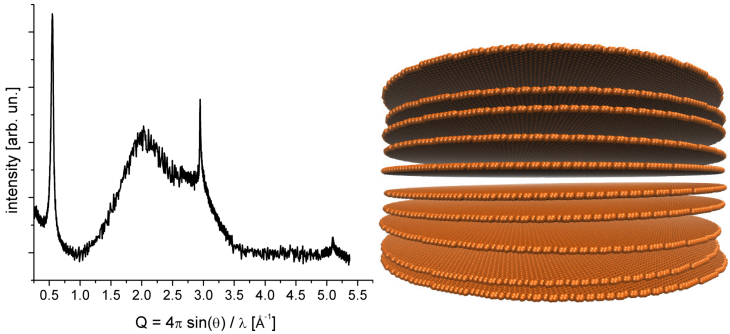

Figure 3.13: Intensities scattered by a dispersion of (0.050g) graphite oxide dispersed in (150µL) distilled water (left) and simplified atomistic model used to speculate on GO structure. *Adapted from [69].*

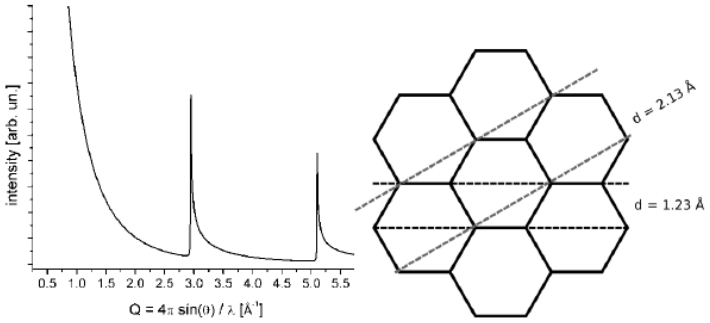

Figure 3.14: Output of the DSE applied to a circular graphene layer defined by a diameter of $D = 50$nm (left) and schematic of the honeycomb lattice with distances corresponding to (100) and (110) RS points. *Adapted from [69].*

(iii), corresponding to an interplanar distance of $d \approx 11.38$Å, results from the stacking of GO layers. The simulated pattern of a small graphite-like clusters (five layers, $D = 50$nm), like the one depicted in figure 3.13, with the appropriate layer separation is reported in figure

3.15. To keep the discussion as simple as possible, five circular graphene layers are stacked without considering the contribution of oxygen and hydrogen (which, by the way, can be easily added to the model).

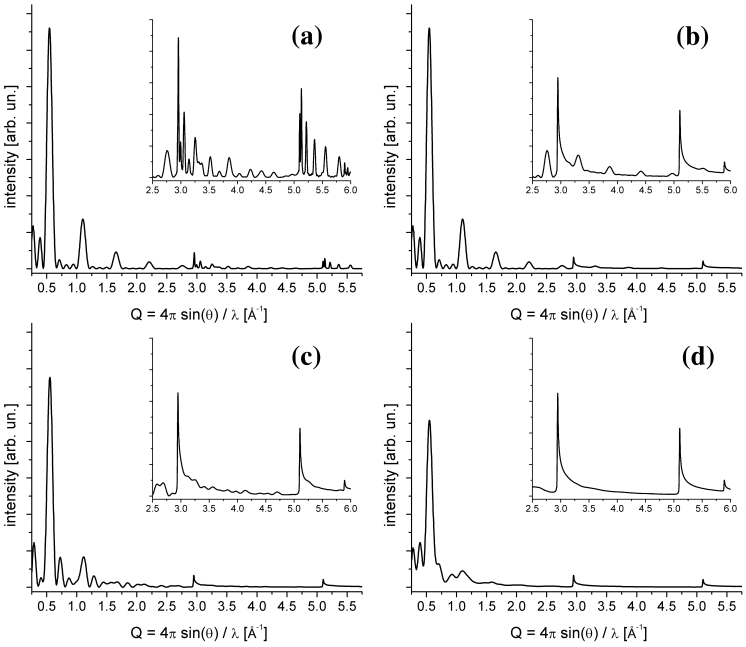

Figure 3.15: Simulated pattern for five layers of graphene stacked in a graphite-like structure, with increasing disorder from (a) to (d). See text for details. *Adapted from [69].*

In more detail, figure 3.15a is the powder pattern of a graphite-like system, *i.e.* a stacking of five layers constructed according to graphite symmetry, which clearly differs from observed data. Rotation of each layer by a random amount about the stacking axis (figure 3.15b) only affects the shape of the in-plane reflections: (100) and (110) peaks (see the inset) assume the typical asymmetry of a bi-dimensional structure, clearly demonstrated by experimental data. A different type of disorder is responsible for the suppression of the higher orders reflections of

the peak located at $Q \approx 0.5\text{Å}^{-1}$, mostly visible in figure 3.15a as satellite lines. By adding a random fluctuation of the interlayer distances, smaller than 1Å, several features tend to disappear (figure 3.15c). However, the most intense effect is produced by a random tilt about the stacking direction. As demonstrated in figure 3.15d, even a small tilt ($< 5\times10^{-3}$ degrees) removes most features apart from the fundamental modulation of the stacking ($Q \approx 0.5\text{Å}^{-1}$) and the in-plane reflections, in this case almost identical to those computed from the single layer (figure 3.14).

A further smoothing of the scattering features results from the effect of morphologic dispersion, in terms of correlation lengths either along the stacking direction and in-plane. Considering a set of clusters with two to ten layers, in-plane extension between 100 and 200nm, and adding the contribution of a cluster of water molecules (MD simulation) allows to obtain the pattern in figure 3.16.

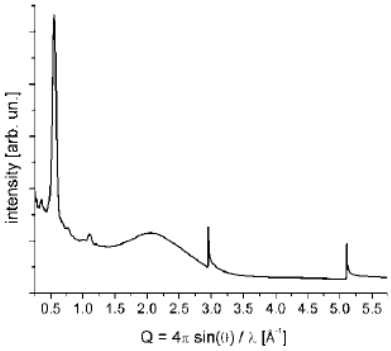

Figure 3.16: Simulated pattern of small graphite-like clusters dispersed in water. *Adapted from [69].*

It is also worth nothing that epoxy and hydroxyl groups locally destroying the bond planarity, structural defects [97, 98] and rippling [68, 99] also contribute to extinguish in-plane reflections and therefore need to be considered. However, as stated, the aim of this case study is only to demonstrate the power of the atomistic approach.

3.5 Assumptions

Different assumptions have been more or less explicitly made in this Chapter to build the intensity distribution, expressed by equation 3.6.

To commence with, the atomic form factor has been built, considering high-energy X-rays, exploiting the first Born approximation. In this framework, the former quantity is therefore the Fourier transform of the electronic density, like in equation 3.3 (see *e.g.* [100]). Moreover, the electronic density has been taken as symmetrically distributed around the nucleus (a complete and rigorous dissertation on radiation-matter interaction can be found *e.g.* in [101, 102]).

The impinging beam has been assumed to be *ideal (fully coherent)*, *i.e.* (i) perfectly monochromatic (*longitudinal coherence length*) and (ii) propagating in a well defined direction (*transversal coherence length*). If the distance to the detector is much larger than the typical size of the sample, *i.e.* it is in the *(Fraunhofer) far-field* region, scattered beam can be supposed to be in the same plane-wave state as the impinging beam. In any case, the assumption of full coherence can be partially relaxed since a *coherence volume* larger than the atomic aggregate is the actual requirement.

The so-called *kinematical approximation* (see *e.g.* [62]) is supposed to hold. In this framework, being the interaction between the beam and the crystal weak, the probability of multiple scattering with small size domains is negligible (lack of multiple scattering events). This approximation should work excellently for submicron-sized crystals investigated with X-ray photons.

Lastly, the *interaction time* between waves and scatterers is supposed to be negligible (X-ray frequencies are much higher than atomic vibration frequencies), *i.e.* the intensity distribution effectively corresponds to a snapshot of the atomic aggregate, not including the "blurring" effect due to atomic thermal vibrations.

Chapter 4

Small crystallites

> [...] we shall consider the effect on the diffraction pattern of various crystal imperfections such as small crystallite size, strains, and faulting. Since it is the simplest kind of imperfection, we start with the consideration of the effect of small crystallite size.
>
> B.E. Warren, 1990 [57]

Inasmuch the scattered signal is built considering each scatterer within a given volume, the effect of crystallite size/shape (morphology) on the diffraction pattern is automatically taken into account. Furthermore, dealing with single atoms implies the full control over whatever kind of "crystal imperfection". *Exempli gratia*, figure 4.1 portraits a small slab of aluminum (fcc, a = 4.05) placed on top of a (100) nickel substrate (fcc, a = 3.52), which causes an array of line defects together with a complicated strain field establishes in order to alleviate the (potential) energy cost associated with the lattice mismatch, together with a cross-section of the intensity distribution around (220) RS point.

The final goal of interpreting a scattering experiment should be to draw a picture as accurate as possible of atomic positions for the duration of the experiment. While it is appealing to try to decipher data fitting each atom position, it appears convincing the need for some physical model reducing the number of degrees of freedom (the complexity) from the number of atoms (which can be of the order of several millions) to a more manageable set.

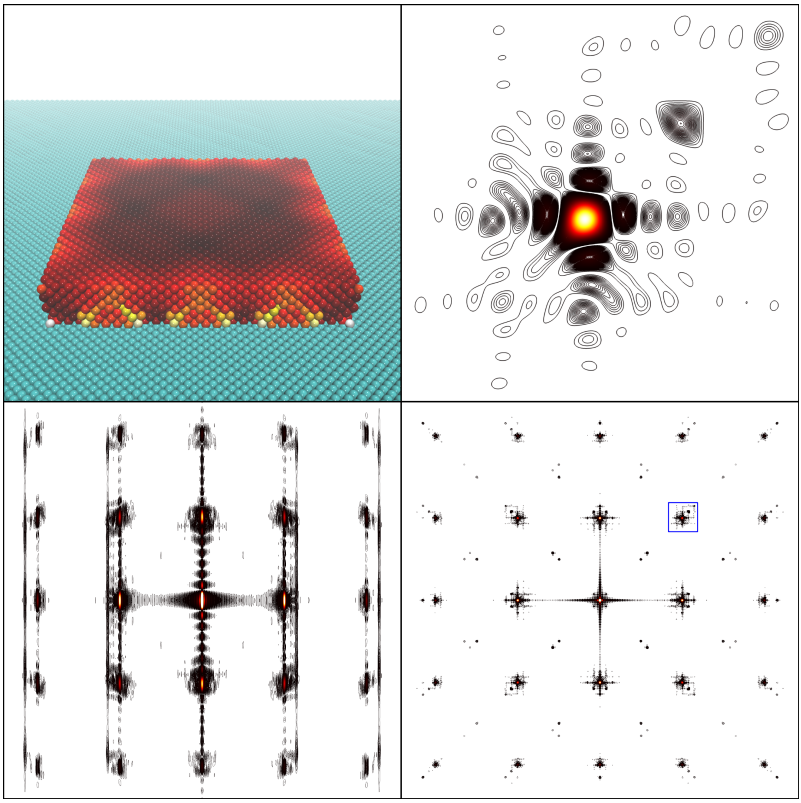

Figure 4.1: To reduce energy associated to lattice mismatch of a (100) slab of aluminum atoms on top of a (100) nickel substrate (cyan), MD predicts an array of line defects and a complicated displacement field, colored according to the Euclidean norm of equation 2.13, ranging from black (close to zero) to white (close to $4.050/\sqrt{2}$Å) (top, left). A hk0 cross section of the intensity distribution around (220) RS point from aluminum atoms, considered as separated from the substrate, is computed according to equation 3.6 (top, right). A h0l (bottom, left) and hk0 (bottom, right) RS cross sections of the same aggregate, extending approximately from -3.75 to 3.75Å^{-1} are also shown. Blue square surrounds 220 reflection, reported above.

4.1 Crystallite response to surface tension

• ○ • ○ • *Part of this section has been adapted from [46, 103, 104].* Atomic aggregates at the nanoscale violate symmetry rules fulfilled by their bulk counterparts. Barring *non-crystallographic* particles, frequently reported in nanoscience (see *e.g.* [105–109]), two symmetry breakings are intrinsically connected with the small crystallite size. While the most obvious one lies in the finiteness of the body, which is a limit for *translational invariance*, the more subtle one is connected to the generation of a *surface*. By symmetry, each atom inside an ideal crystal experiences a null net force. The creation of a surface implies a symmetry breaking which, in turn, results in a force responsible for displacing atoms to different equilibrium positions. Particularly, the physical principles ruling atomic displacement in (clean) metals are given by the *Smoluchowski smoothing effect* [110]. In this picture, the electron distribution on a surface is rearranged so to diminish the kinetic energy of the system. This redistribution leads to the establishment of electrostatic forces which displace of the outermost layers.

4.1.1 Effect of surface relaxation on powder patterns

For a spherical object of radius R, the surface $S(R) = 4\pi R^2$ over volume $V(R) = 4\pi R^3/3$ ratio diverges for the radius approaching zero. It is indeed the remarkable ratio of atoms sitting on the "outermost layers" to the total number of atoms composing the aggregate which causes surface effects to be sizable in nanostructured particles (NPs).

Although following concepts regard atomic rearrangement in a solid aggregate in response to the so-called *surface relaxation*, the point of view of powder diffraction is chiefly adopted to emphasize the way intensity distribution in RS is modified. In this context, to account for rather specific effects such as anisotropic broadening and asymmetry of the line profiles, in addition to peak position shift, of particular interest has been the effort to condense main features of this phenomenon by using models which minimize the number of fitting parameters. Notably, the works by Nunes and Lin [111], Ishikawa and Uemori [112] and Leoni and Scardi [113], whose phenomenological models are all based on a simple exponential displacement of the average unit cell dimension along the radial direction.

4.1.1.1 Atomistic simulation of clean metallic surfaces

Numerous simulations have been carried out to attempt understanding structural and dynamical features engendered by the creation of a surface. Different materials and conditions have been investigated, employing interatomic potentials based on the formalism of the EAM, the MEAM and the ReaxFF, mentioned in subsection 2.2.4. A few selected cases are reported, for simplicity confined to metallic fcc nanostructured crystals (NCs) in an otherwise vacuum environment, which nevertheless allows various insights to be drawn.

Computational details NCs defining *as-built configuration* were carved out of an ideal fcc crystal described by the lattice parameter predicted by the interatomic potential for the considered temperature. Atoms with less than six nearest neighbors were removed from the carved particle so to avoid noticeably high-energy configurations.

MD calculations were performed by means of the Large-scale Atomic/-Molecular Massively Parallel Simulator (LAMMPS [114]) with atomic interactions ruled by the EAM. Although this class of potentials often underestimates surface energy and therefore poorly perform when tackling problems involving the surface, the implemented parameterization [115] reasonably agrees with experimental data. Furthermore, it is worth noting that the purpose of the presented investigation disregards the accurate representation of a specific material. Instead, the aim is to disclose a picture and a physical interpretation of the peculiar atomic arrangement and put forward some general comment.

Integration timestep was set to one hundredth of the reciprocal of the largest phonon frequency in the ideal crystal at room temperature ($RT = 298.150$K) so to minimize numerical artifacts. Simulation commenced with a random field of velocities drawn from a normal distribution [116], imposing a temperature twice the target one, by virtue of the equipartition of energy [117]. The system was then gently equilibrated having fixed the number of atoms, the volume and the temperature of the system (canonical ensemble (NVT)), employing Langevin dynamics [118] and then a chain of Nosè-Hoover thermostats [119]. After this stage, the production phase initiated and data started to

be collected with the system evolving according to the microcanonical ensemble (NVE).

Observables Powder diffraction patterns are computed according to the DSE, defined by equation 3.9. Besides the *as-built* reference diagram, obtained using the as-built (reference) configuration as input, in order to highlight static and dynamic features due to surface relaxation two additional observables are defined (see the discussion in section 2.3).

First, the *time-averaged* pattern, obtained from the mean of a set of patterns computed from atomic configuration at each snapshot collected during the production phase, $I(Q) = \langle I(Q; r_t)\rangle_t$. This should mimic a real experiment, being both static (atomic re-arrangement) and dynamic (atomic vibrations) features included.

Second, *average-position* configuration is used as input from the DSE so to exclude the effect of vibrations, $I(Q) = I(Q; \langle r_t\rangle_t)$.

4.1.2 Models for surface relaxation

• ○ • ○ • *Part of this section has been adapted from [46, 103].*

The introduction of a surface causes atoms to displace from their reference position. For the streamlined case of spherical copper particles the radial strain (equation 2.18) is depicted by figure 4.2, where a complicated, oscillating behavior, more compressive when approaching the surface is shown.

Some considerations can be drawn considering the Young-Laplace equation [120, 121] for a spherical object of radius R,

$$\Delta p = 2\frac{\gamma}{R}, \tag{4.1}$$

where Δp is the difference between internal and external pressure and γ the surface tension. Expressing pressure in terms of Hooke's law [122] and considering γ to be the average (over representative crystallographic facets) surface energy for the copper/vacuum interface leads to an estimate of the radial strain at the surface,

$$\varepsilon_R = \frac{2}{E}\frac{\gamma}{R}, \tag{4.2}$$

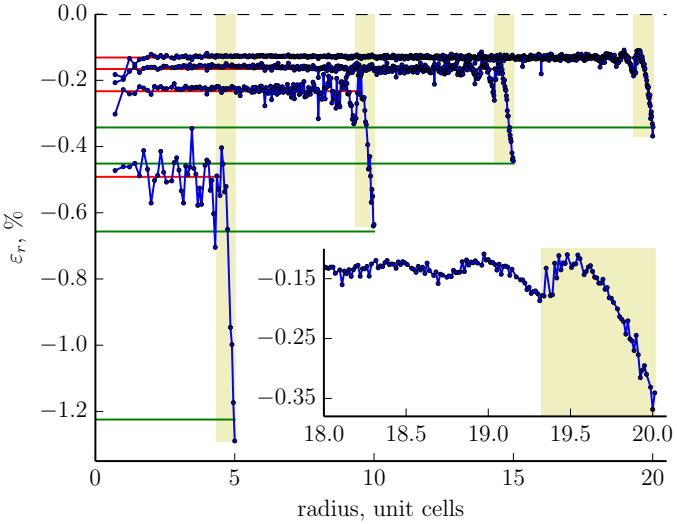

Figure 4.2: The radial strain, expressed as a function of the radius of the *as-built* spherical crystal, is reported for four copper particles (a = 3.615Å). Under-coordinated regions (outermost layers) are limited by yellow rectangles, horizontal green lines pinpoint the value predicted by the Young-Laplace equation (4.2) and horizontal red lines specify the radial strain averaged over the fully-coordinated region (characterized by twelve nearest neighbors). The inset reports a selected region of the curve calculated for the biggest particle, emphasizing the oscillating behavior of the deformation. *Adapted from [103].*

being E the Young's modulus. Interestingly, when using the above mentioned constants computed from the employed interatomic potential, this simple expression reasonably agrees with values predicted by MD simulations, as depicted by figure 4.2.

Figure 4.3 illustrates on a perceptional level the effect of above-discussed features on patterns computed from the DSE. While the main effect is a peak shift, the line profile is also affected.

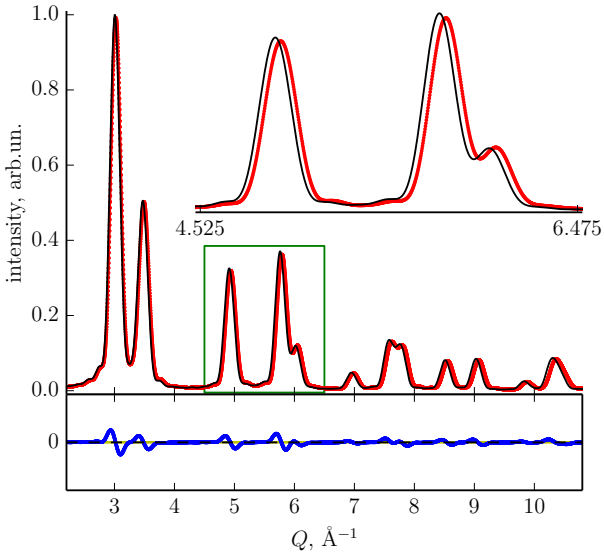

Figure 4.3: Output of the DSE for the smallest copper sphere (1.8nm or 5 unit cells radius). The as-built object (black line) and corresponding average-position configuration (red dots) with the difference between patterns (blue line, below) are reported. The inset shows a magnification of the region inside the green rectangle. Clearly, peaks shift is the dominating feature.

As briefly introduced, commonly employed phenomenological models displace atoms according to some function of the modulus of the radius r, as *e.g.* in the formulation by Ishikawa and Uemori† [112],

$$\varepsilon_r\left(r; f, k\right) = f \exp\left(-\frac{R-r}{k}\right), \tag{4.3}$$

being f and k the tunable parameters and R related to the particle size. Beyerlein and colleagues† observed the same oscillating behavior reported in figure 4.2 and proposed accordingly an adjustment of the

†Symbols have been modified with respect to the original formulation

above equation [123],

$$\varepsilon_r\left(r; f, k, n\right) = f\exp\left(-\frac{R-r}{k}\right)\sin\left(\frac{2\pi n r}{R}\right), \tag{4.4}$$

by adding the additional fit parameter n.

To access a more detailed picture of atomic rearrangement, the radial strain along selected lines passing through the centroid of the particles (diameters) was computed, therefore considering the projection of the deformation along different directions. The result is summarized in figure 4.4, where the radial strain is reported for selected directions within the largest sphere. As expected from the elastic anisotropy of the crystal, different crystallographic directions show a different average radial deformation.

While interpreting intensity distribution around a few RS points emanated from gold NCs, Huang and collaborators[†] realized the anisotropic behavior of surface relaxation. Furthermore, they used a simple argument by Pauling [124] to express the radial strain as a function of the coordination $\mathcal{N}$ of a given atom [125],

$$\varepsilon_r\left(\mathcal{N}; \alpha, \kappa_{hkl}\right) = \frac{\alpha}{R}\kappa_{hkl}\ln\left(\frac{12}{\mathcal{N}}\right), \tag{4.5}$$

where α and κ_{hkl}, a numerical coefficient depending on the given crystallographic direction, are fit parameters. Interestingly, this model is implicitly independent of the shape of the object (although a radial direction for the deformation is imposed), being the undercoordination the "driving force" for deformation.
To further assess anisotropy of deformation, the displacement field with respect to the reference configuration and the strain projected on selected planes (equation 2.14) through the centroid of a palladium truncated cube are depicted in figure 4.5. While from figure 4.5a it is clear the tendency for atoms less coordinated to displace inward, figure 4.5b depict the extension of the so-called *surface-relaxation*: to minimize surface energy, the entire NP – and not only the outermost layer – is deformed, according to the symmetry of the elastic tensor.

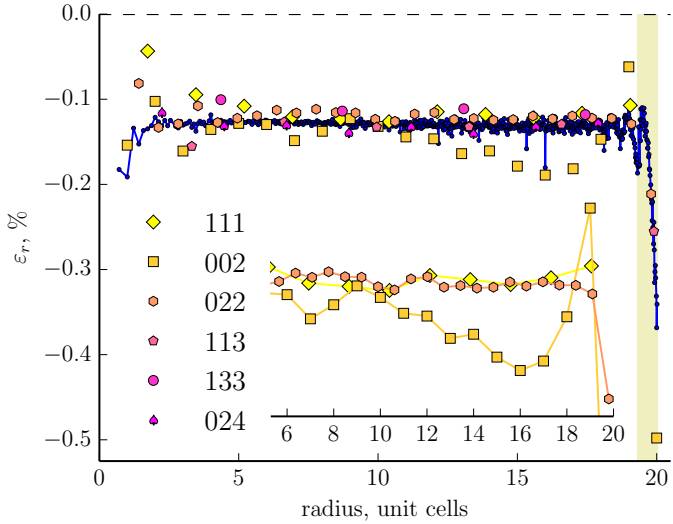

Figure 4.4: Radial strain for selected directions. The inset shows the trend for directions [002], [111] and [022], with the modulus of the average radial deformation increasing from the stiffest [111] direction to the softest [002] which experiences the heftiest deformation. *Adapted from [103].*

A direction- and coordination-dependent model for crystal response to surface tension Proceeding the arguments given by Huang and colleagues, the position of the n-th atom in the deformed configuration (denoted by suffix d) is expressed as

$$\mathbf{r}_{n,d}\left(\mathbf{r}_n, z; \alpha, a, \sigma\right) = \kappa\left(\hat{\mathbf{r}}; \alpha\right)\left[\frac{a - a_0}{a_0} + \sigma \ln\left(\frac{\mathcal{N}}{z}\right)\right]\mathbf{r}_n. \tag{4.6}$$

From the right, the fit parameter σ modulates the "Pauling term", not null for an incomplete atomic environment which is ideally characterized by $\mathcal{N}$ nearest neighbors ($\mathcal{N} = 12$ for the fcc system). Next, the tunable parameter a is responsible for a constant offset of the deformation which insists on the particle as clearly depicted by figure 4.2. For convenience this term is normalized to the equilibrium lattice param-

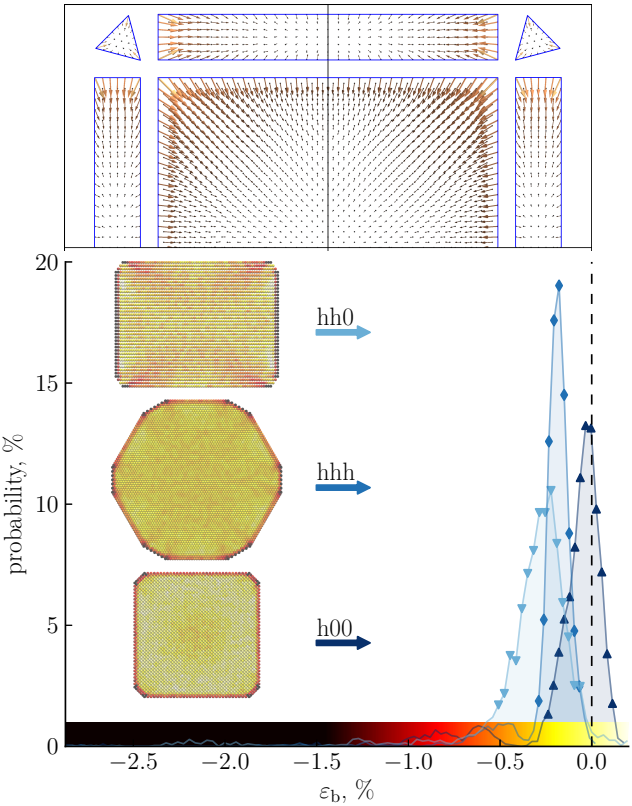

Figure 4.5: Top, atomic displacement with respect to as-built configuration on (100), (110) and (111) facets for a palladium truncated cube. Arrows are amplified for graphical convenience. Bottom, histogram of the average local strain (equation 2.14) projected on three significant cross-sections (hh0), (hhh) and (h00), drawn in the inset. The color scale shown on the abscissa represents the strain distribution. *Adapted from [104].*

eter a_0. Last but not least, κ produces the hkl-dependent behavior,

$$\kappa\left(\hat{\mathbf{r}};\alpha\right) = (1-\alpha) + \alpha\,\frac{s_{\hat{\mathbf{r}}}}{\overline{s}}, \tag{4.7}$$

being $s_{\hat{\mathbf{r}}}$ the compliance of the crystal projected on direction $\hat{\mathbf{r}}$, $\overline{s}$ its average value over all possible crystal directions and α a fit parameter. Considering cubic crystal symmetry, the reciprocal of the Young's modulus along $\hat{\mathbf{r}} = \{u_1, u_2, u_3\}$ can be expressed in terms of compliance matrix ($\mathcal{S}$) elements as (see *e.g.* [126]),

$$s_{\hat{\mathbf{r}}} = \frac{1}{E_{\hat{\mathbf{r}}}} = s_{11} - 2\left(s_{11} - s_{12} - \frac{s_{44}}{2}\right)\left(u_1^2u_2^2 + u_2^2u_3^2 + u_3^2u_1^2\right). \quad (4.8)$$

The displacement field engendered by this model can be quite complicated, depending on the choice of fit parameters. The simplest case consists of a coordination- and direction-independent ($\sigma, \alpha = 0$) deformation, corresponding to a uniform scaling, both expansive $a > 0$ or compressive $a < 0$, of atomic coordinates. If the dependence on the given crystallographic direction is considered ($\alpha \neq 0$), the deformation field mimics the symmetry encoded in equation 4.8, depicted by figure 4.6 for the case of palladium, responsible for both diffraction peaks shift and broadening.
In principle, in place of α the set of unique elements of the compliance matrix can be fitted. While this sounds appealing, especially since there is no guarantee for properties derived for an ideal crystal to apply to a NC, the propensity is to employ the smallest number of fit parameters. For the same reason, the symmetry of compliance matrix is applied to the outermost (under-coordinated) layers, although the persistence of the symmetry in this region is questionable.

4.1.3 Shape-effect on deformation

Different crystallographic facets, characterized by diverse energetic and mechanical properties, can be exposed in NCs. To illustrate the point, particles framed by (i) (100) planes (cube), (ii) (110) planes (rhombic dodecahedron) and (iii) (111) planes (octahedron) were carved out of an ideal lead lattice, the size chosen so to include approximately the same number of atoms (12,187, 11,393 and 11,720 respectively). It is the interplay between symmetry of the elastic tensor and of the given object which engender a displacement field (equation 2.13) complicated both in the magnitude and in the direction, as depicted in figure 4.7. Among simulated objects, the spherical aggregate seems

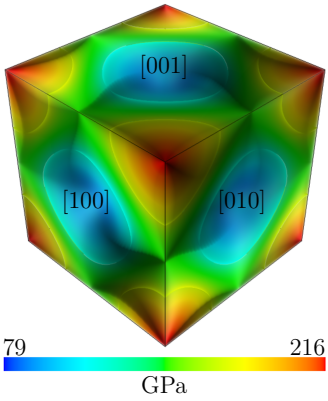

Figure 4.6: Symmetry of palladium Young's modulus computed from the reciprocal of equation 4.8, using data reported in table 5.1.

to be the simplest one, with the lowest effect of anisotropy as a result of the averaging effect over facets characterized by different Miller indices.

The choice of the abscissa of figure 4.8a stems for the assumption that deformation (equation 2.17) at the particle/vacuum interface can be expressed by means of equation 4.2 and therefore is proportional to γ_{hkl}/E_{hkl}, the ratio for the crystallographic planes enclosing the NC. It is worth noting that the spherical case, showing no specific facet, has no abscissa and is conventionally left near the ordinate axis.

4.2 Atomic vibrations

Considering the case study presented in subsection 4.1.3, it is interesting to evaluate the extent of atomic vibrations, represented at the atomic level by the MSD, computed by applying equation 2.23 to the MD trajectory. In turn, this quantity, is related to the (isotropic) *B-factor* B_{iso} (equation 2.24), reported in figure 4.9 as a function of the Young modulus projected along the direction perpendicular to a given face.

The linear relation is justified simplifying atomic vibrations to a spring

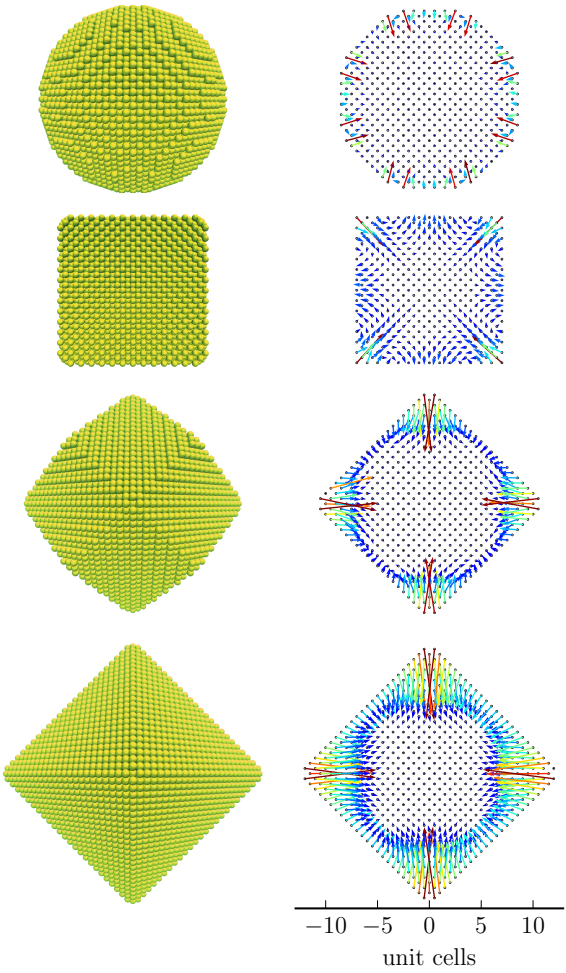

Figure 4.7: Displacement maps of four Pb samples. From left to right, sphere, cube, rhombic dodecahedron and octahedron. Maps refer to the (100) cross section (above), with the magnitude of the displacement vector multiplied by 25 times to emphasize displacement. *Adapted from [46].*

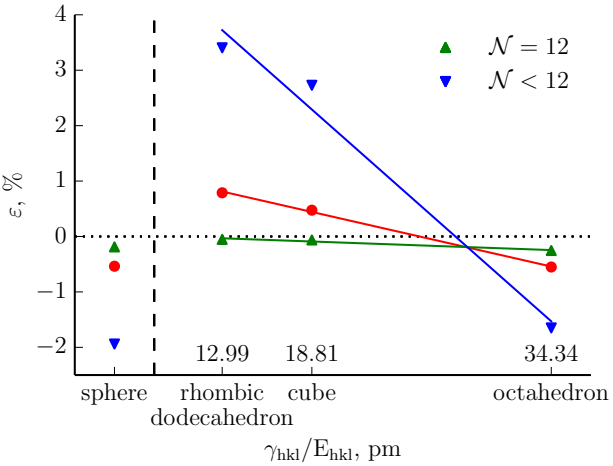

Figure 4.8: The average strain for systems exposing different crystallographic facets, denoted by hkl, as a function of the surface energy to Young's modulus normal to the given facet (left, see table 4.1 for physical properties) is reported. $\mathcal{N}$ indicates the atomic coordination, so $\mathcal{N} < 12$ (▲) is for outermost layers and $\mathcal{N} = 12$ (▼) for fully-coordinates atoms, whereas full circle (●) refer to the average over the entire aggregate. Lines are drawn to drive the eye. *Adapted from [46].*

system: the stiffer the spring constant, the narrower the oscillation. In fact, the softest spring, corresponding to the $[h00]$ direction (cube faces), allows the widest out-of-plane atomic oscillations, the stiffest $[hhh]$ (octahedron faces) gives the narrowest, with the rhombic dodecahedron (framed by $\{hh0\}$) laying in between. As in figure 4.8a, the sphere has no given abscissa, and corresponding values fall in between the limits of the $[h00]$ and $[hhh]$ cases. It is also worth noting that the anisotropy effect is much stronger for undercoordinated environments: again, considering that each atom is bounded by a spring, the smaller the coordination, the wider the oscillation. From geometrical considerations, the number of nearest neighbors in the outermost layer for $\{hhh\}$, $\{hh0\}$ and $\{h00\}$ facets are, respectively, 9, 11 and 8. To be added, while $\{hhh\}$ and $\{h00\}$ facets present a fully-coordinated layer

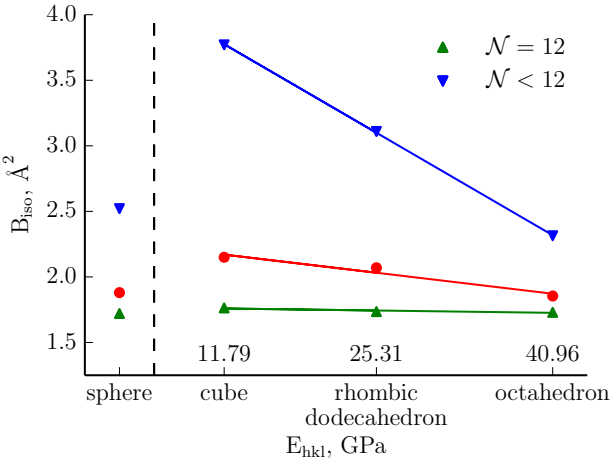

Figure 4.9: B_{iso} plotted against elastic modulus along the normal to the facets (right) is shown. $\mathcal{N}$ indicates the atomic coordination, so $\mathcal{N} < 12$ (▲) is for outermost layers and $\mathcal{N} = 12$ (▼) for fully-coordinates atoms, whereas full circle (●) refer to the average over the entire aggregate. Lines are drawn to drive the eye. *Adapted from [46].*

beneath the outermost one, the $\{hh0\}$ geometry implies a layer with coordination 7 below the one with coordination 11.

To emphasize the dependency of the average vibrational amplitude on atomic coordination [127–130], the MSD for the four spherical copper aggregates presented in subsection 4.1.2 is shown in figure 4.10. The magnitude of the time-averaged MSD shows the same trend and takes approximately the same value at the vacuum/particle interface for each particle size, showing a core-shell structure and therefore supporting the coordination-dependency argument. Average values for B-factors increase from the larger (diameter 14.460nm) to the smaller sphere (diameter 3.615nm), respectively from 0.632 ± 0.008 to 0.720 ± 0.040Å^2, as a result of a weighted average over different fractions of under-coordinated to fully-coordinated atoms.

A model has been developed to consider the effect of vibrations (consid-

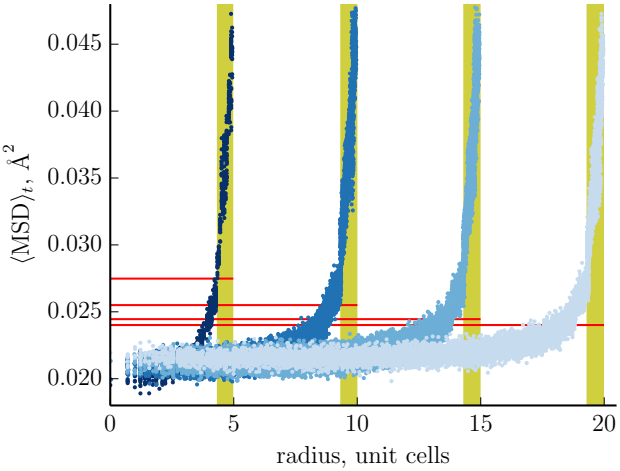

Figure 4.10: Time-averaged mean squared displacement as a function of the radius for four spherical copper aggregates characterized by different diameters. Under-coordinated regions are limited by yellow rectangles while horizontal red lines indicate the average value. *Adapted from [103].*

ered as correlated), automatically including intensity depression, thermal diffuse scattering (TDS) and structural features; it is built considering vibrations instead of phonons, which are the more traditional approach. However, such new development is still in progress and will not be described here any further.

4.3 Modeling the pattern from metal nanocrystals

● ○ ● ○ ● *Part of this section has been adapted from [46].*
MD was used to simulate spherical aggregates of five elements displaying a wide range of properties, especially concerning material stiffness and elastic anisotropy. Features arising from the introduction of a surface are interpreted and discussed within the framework of two different approaches, respectively based on (i) a RS (the most widely used) and (ii) a DSE representation of the underlying model.

4.3.1 Whole powder pattern modeling

In the framework of the traditional approach employed to interpret signal diffracted from condensed matter, either (i) peaks are described by (mathematical) profile functions (profile fitting), or (ii) model-based expressions which permit a direct evaluation of structural and microstructural parameters. Within the latter category, whole powder pattern modeling (WPPM) is a perturbation approach applied to a perfect crystal model in RS (see *e.g.* [131, 132] and references therein). The effect of any deviation from the otherwise perfect crystal (*i.e.*, any *microstructural feature*) is then convolved to the model to build the peak profile. Notably, models for finite size and shape [133], strain fields due to dislocations of different type in any crystal system [134] and stacking faults [131, 135, 136] are available therefore allowing crystals to be investigated down to small sizes, with the highest precision for the spherical domain shape [137]. More difficult to express in the WPPM procedure is the atomic displacement engendered by surface tension, so far only tackled by simplified models [113]. Thermal vibrations can also be considered, according to a model proposed by Warren [57, 138] and recently adapted to the finite size of NCs [139].

In the following, a spherical NC model is adopted, including the Debye-Waller factor and the TDS for the spherical shape [133]. To account for the complex atomic displacement caused by the relaxation of surface forces, a flexible (although not entirely rigorous) root mean squared displacement (*microstrain*) is introduced by representing the associated peak profile component with a pseudo-Voigt function [140] whose width varies for different (*hkl*)s according to the fourth order invariant form of Miller indices for cubic materials [141],

$$\Gamma_{hkl} = A + BH = A + B\frac{h^2k^2 + k^2l^2 + l^2h^2}{\left(h^2 + k^2 + l^2\right)^2}. \tag{4.9}$$

The Fourier Transform (FT) of the peak profile component related to atomic displacement can therefore be expressed as [140]

$$A^D\left(L\right) = \exp\left(-Q^2\frac{L^2\langle\varepsilon_{hkl}^2\left(L\right)\rangle}{2}\right) \cong \exp\left(-Q^2\Gamma_{hkl}\frac{aL + bL^2}{2}\right), \tag{4.10}$$

where $\langle \varepsilon_{hkl}^2 (L) \rangle$ is the variance of the strain distribution for a correlation (or Fourier) length L.

Similarly, peak positions are also displaced by remapping interplanar distances d_{hkl} according to the symmetry of the crystal,

$$d_{hkl} = d_{hkl}^0 \left(A' + B' H \right). \tag{4.11}$$

4.3.2 Challenging interpretation paradigms

MD has been employed to simulate five metals displaying a wide range of properties, reported in table 4.1. The shape of the aggregates used to generate test cases for interpretation paradigms was a sphere. After atoms with less than six nearest neighbors were removed, the DSE was applied to atomic positions to generate powder diffraction patterns. Three patterns were generated for each combination of element and radius, corresponding to (i) *as-built*, (ii) *time-averaged* and (iii) *average-position* configurations (see section 2.3). Although already discussed, it is worth remembering that the pattern generated from configuration (ii) should mimic a real experiment, being both static (atomic arrangement) and dynamic (atomic vibrations) features included; whereas data computed from configuration (iii) does not include the effect of atomic vibrations and singles-out the effect of atomic displacement engendered by the finiteness of the body. Although a pattern generated from the *as-built* configuration has no particular physical meaning, it is useful to produce the effect of morphology by itself.

To assess the statistical quality of each fit, the Normalized Residual Sum of Squares (NRSS) is introduced,

$$NRSS = \frac{1}{P} \sum_{p=1}^{P} \left(\frac{I_{m,p} - I_{s,p}}{N f_q^2} \right)^2 = \frac{1}{P} \sum_{p=1}^{P} \left(\Im_{m,p} - \Im_{s,p} \right)^2, \tag{4.12}$$

where the normalization over (i) the number of atoms N and (ii) the squared form factor f allows fits from aggregates characterized by different (i) volume and (ii) chemical composition to be compared. This way, it is actually the squared difference of the *interference function* (see *e.g.* [61]) of the model (m) and of the simulation (s) to be computed. Finally, the normalization over the number of points P permits patterns sampled with a different number of points to be compared.

	Rh	Pd	Ag	Pt	Pb	
a	3.8034	3.890	4.090	3.92	4.9508	Å
E	369	127	78	180	25	GPa
$E_{\langle 100\rangle}$	300.6	78.9	48.5	136.3	11.8	GPa
$E_{\langle 110\rangle}$	405.5	150.6	92.3	186.0	25.3	GPa
$E_{\langle 111\rangle}$	458.9	216.2	132.2	211.8	41.0	GPa
Zr	1.651	2.982	3.000	1.604	3.753	/
$\gamma_{\langle 100\rangle}$	2.481	1.645	1.042	1.778	0.476	Jm^{-2}
$\gamma_{\langle 110\rangle}$	2.381	1.747	1.125	1.934	0.532	Jm^{-2}
$\gamma_{\langle 111\rangle}$	2.233	1.529	0.977	1.694	0.405	Jm^{-2}
T_m	2,065	1,680	1,255	1,890	680	K

Table 4.1: Lattice parameter (a), Young modulus projected on different directions (E), Zener ratio [142] ($Zr = 2c_{44}/(c_{11} - c_{12})$), surface energies ($\gamma$) and melting temperature (T_m) for simulated elements. Properties are calculated for the given interatomic potential using values taken from [115].

4.3.2.1 As-built aggregates

When the WPPM approach is applied to *as-built* NCs, a nearly perfect fit is obtained as depicted in figure 4.11. Two parameters were refined, the unit cell parameter a and domain diameter D while all other parameters were fixed, including the scale factor calculated from the known number of atoms.

Refined lattice parameters agree with the model better than 4×10^{-6}, for larger sizes better than 1×10^{-6}. Minuscule differences can be easily explained considering the powder pattern was generated by the DSE for a single (atomistic) model whereas the RS approach, as implemented by WPPM, implicitly assumes the condition of Ino and Minami [137, 143]. In this context, an average of patterns computed from spherical models centered in different positions is made, as if slightly different spheres were carved out of a perfect lattice. The condition involves a fraction of atoms on the outermost layers, the more significant the smaller the size of the aggregate [137].

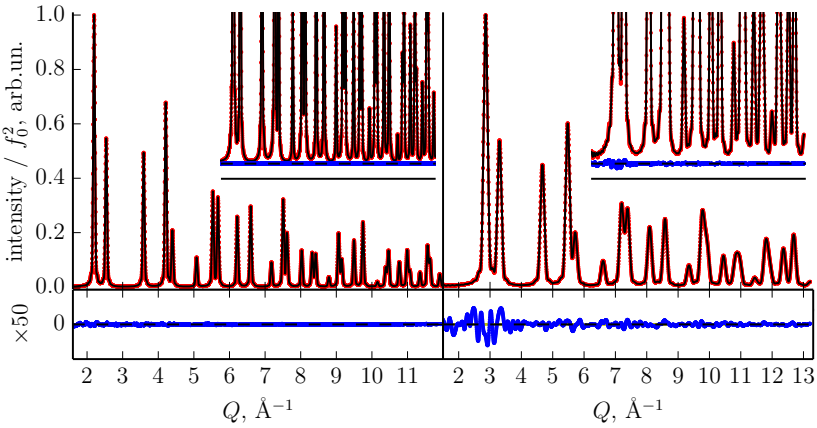

Figure 4.11: Results of WPPM applied to the powder patterns produced by spherical aggregates of radius 12 (28,867 atoms) and 6 (3,559 atoms) unit cells, respectively for Pb (left, $NRSS = 1.9\times10^{-15}$) and Rh (right, $NRSS = 2.1\times10^{-12}$). Below, the residual between data and intensities generated by the model. A magnification of the peak tail region is also reported in the inset to assess fine discrepancies. *Adapted from [46].*

4.3.2.2 Time-averaged configuration

Six parameters are tuned during the WPPM. They are, besides the lattice parameter and the domain size, the Debye-Waller factor B_{iso}, an effective microstrain with anisotropy parameter B and an effective macrostrain anisotropy parameter B', described in subsection 4.3.1. One of the most evident effects is the shrinkage of the NP caused by surface tension, in turn a consequence of the lower coordination of surface metal atoms, as discussed in section 4.1. The feature is clearly demonstrated by figure 4.12, where the relative change of lattice parameter with respect to the *as-built* value is reported for the five investigated metals and four different spherical domain diameters. Clearly, the effect decreases progressively for increasing size, consequently of the reduction of the surface fraction. Each trend depends on the specific metal and, as a general tendency, the effect is stronger for softer metals

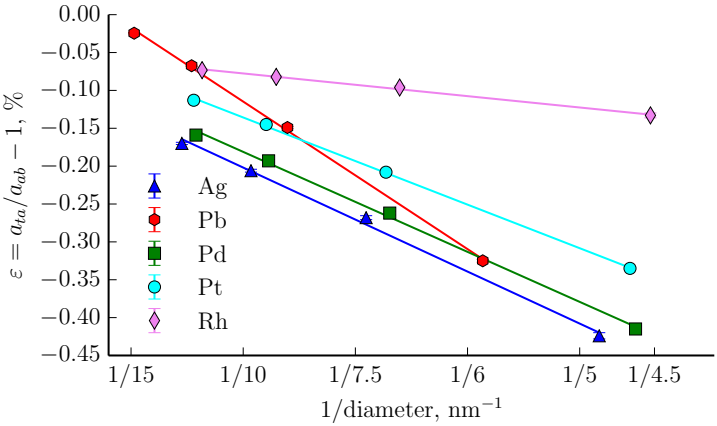

Figure 4.12: Results of WPPM for the relative change of unit cell parameter after MD simulation, computed as the normalized difference between the one calculated from the *time-averaged* (*ta*) configuration and the *as-built* (*ab*) one, as a function of the domain diameter for the five investigated fcc metals. Linear trends parallel those reported by Sheng and colleagues in [144]. *Adapted from [46].*

(lower Young modulus), so the smallest effect is for Rh, the largest for Pb.

As already introduced in section 4.2, the finiteness of the body also affects the Debye-Waller factor, as a result of the decreased number of atoms in surface regions. Refined values of B_{iso}, reported in figure 4.13a, show an inversely proportional relation to the Young's modulus of the investigated metals, in turn related to the "spring constant" for atomic vibrations (actually, the ordinate B_{iso} should be normalized by the lattice parameter, in turn proportional to vibrations amplitude, but this would add little to the discussion and complicate the interpretation). Values refined by WPPM are in a reasonably good agreement with the reference B_{iso} computed applying equation 2.24 to frames of the MD trajectory. The value of B_{iso} increases in smaller domains, as shown in figure 4.13b, since the surface fraction decreases accordingly. Horizontal lines in this figure represent B_{iso} calculated for a

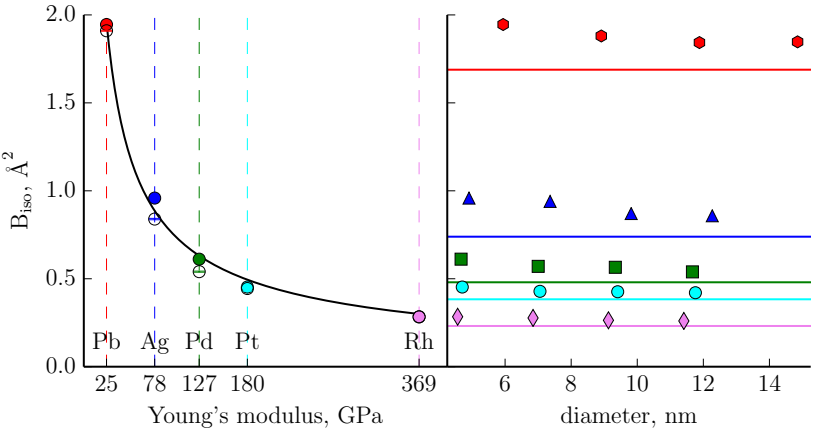

Figure 4.13: B_{iso} for the smallest spherical aggregate reported as a function of the Young's modulus of different metals (left). Values calculated from MD simulations (equation 2.24) are drawn as full symbol, from WPPM for the patterns generated from the *time-averaged* configuration as open symbol. B_{iso} is also shown as a function of sphere diameter (right). Horizontal lines represent B_{iso} calculated for a $40 \times 40 \times 40$ unit cells cube, implementing PBCs in the simulation. *Adapted from [46].*

$40 \times 40 \times 40$ unit cell cube, implementing the PBCs so to mimic an "infinite" crystal. Even if the periodicity condition alters the vibrational properties (the longest phononic wavelength is proportional to the size of the simulation domain as discussed in subsection 2.2.3), values are in good agreement with the literature [145] and correctly point out the asymptotic trend of B_{iso} with the increasing nanocrystal size.

The discrepancy between values of B_{iso} from the WPPM and (calculated) from the simulation mostly stems from the different definition of the quantity in DS and RS. While in the former case an average over atoms and time (see section 2.3) is calculated, the Debye-Waller factor refined by WPPM mostly depends on the depression of intensities with increasing scattering vector, and to some extent on the TDS.

As depicted by figure 4.14 the amplitude of vibrations of atoms sitting

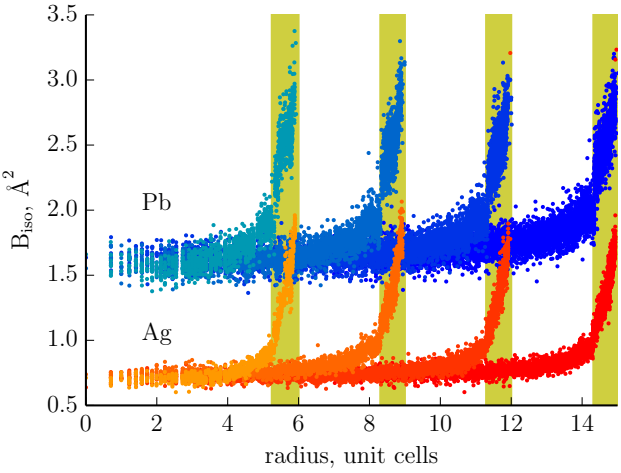

Figure 4.14: B_{iso} as a function of the radial coordinate in four spheres with different radius, expressed in number of unit cells for Ag and Pb. Under-coordinated regions are limited by yellow rectangles. Interestingly, the behavior of B_{iso} as a function of the radius predicted by MD is similar for the two metals. *Adapted from [46].*

on the outermost layers is larger than atoms in a fully-coordinated environment, therefore explaining the dependency of the mean B_{iso} value with the size depicted in figure 4.13b.

To address the role of the TDS term, figure 4.15 reports the WPPM of the powder pattern of spherical aggregates described by a radius of 6 or 12 unit cells and made of silver or lead. Both results obtained implementing a realistic TDS model (right, [139]) and by using the so-called Debye TDS, *i.e.* the diffuse scattering when considering completely uncorrelated atomic vibrations (left, [57]) are shown. It is quite evident for the two cases that the TDS effect cannot be ignored, nor a poor model can be used. Again, the effect of disregarding it gets worst for (i) decreasing the size of the NC and (ii) lowering the Young modulus, since, as already discussed, this implies wider oscillations.

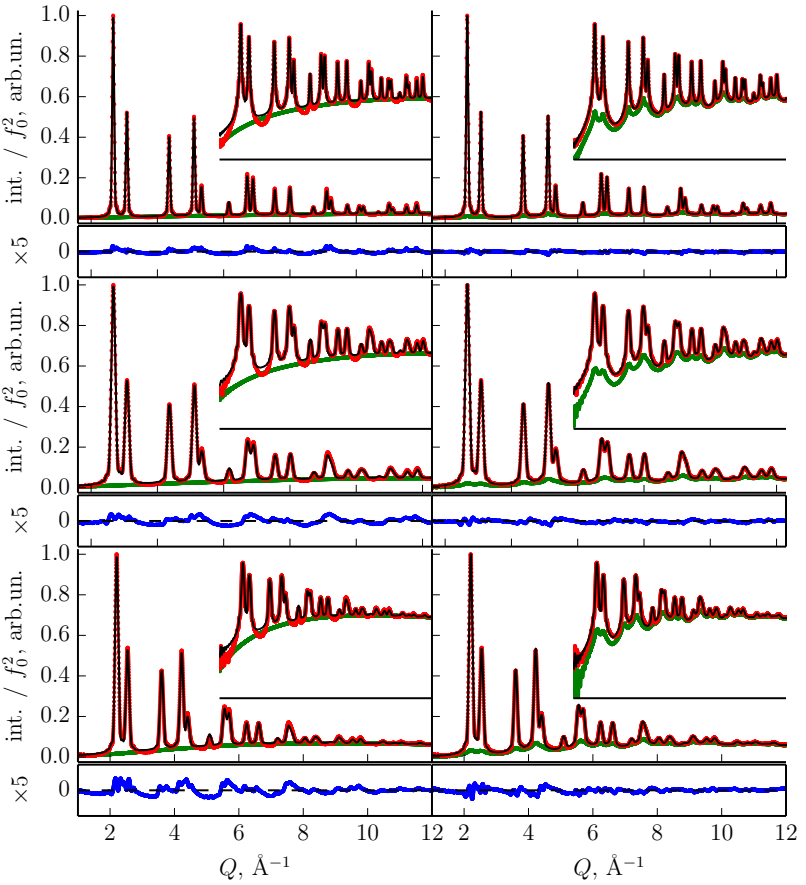

Figure 4.15: Modelling results with TDS models based on correlated (right) and uncorrelated (left) atomic vibrations. Spherical domains with different radius (in unit cells, uc), from the top: Ag 12 uc (uncorrelated $NRSS = 7.9\times10^{-12}$, correlated $NRSS = 1.1\times10^{-12}$), Ag 6 uc (uncorrelated $NRSS = 3.9\times10^{-10}$, correlated $NRSS = 6.4\times10^{-11}$), and Pb 6 uc (uncorrelated $NRSS = 4.1\times10^{-10}$, correlated $NRSS = 1.0\times10^{-10}$). The inset reports a semilogarithmic view of each pattern. *Adapted from [46].*

4.3.2.3 Atomic displacement

Even if peak broadening mainly arises from the finiteness of the body, local atomic displacements engendered by surface relaxation also contribute to alter the line profile. As discussed in subsection 4.3.1, this intricate phenomenon was treated in a simplified way within the WPPM approach, which although not totally rigorous allows different information to be drawn.

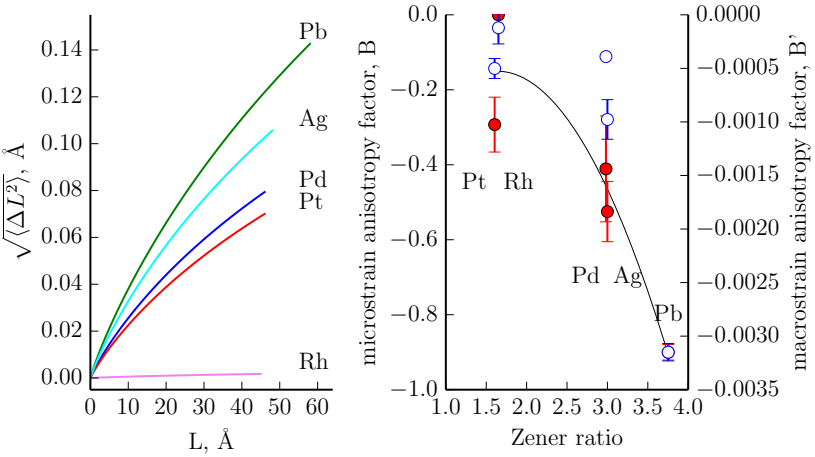

Figure 4.16: Warren's diagram (RMSD as a function of L) for the five elements are shown on the left. The anisotropy of microstrain affecting line broadening (B, •) and of macrostrain (B', ∘), influencing peak position, as a function of the Zener ratio are shown on the right (the line is drawn to guide the eye). All values are obtained from WPPM as those shown in figure 4.15 implementing the TDS model for correlated atomic vibrations. *Adapted from [46].*

WPPM results allow to compute Warren's diagrams [146], showing the Root Mean Squared Displacement (RMSD) as a function of L, the distance between couples of scatterers (which are unit cells according

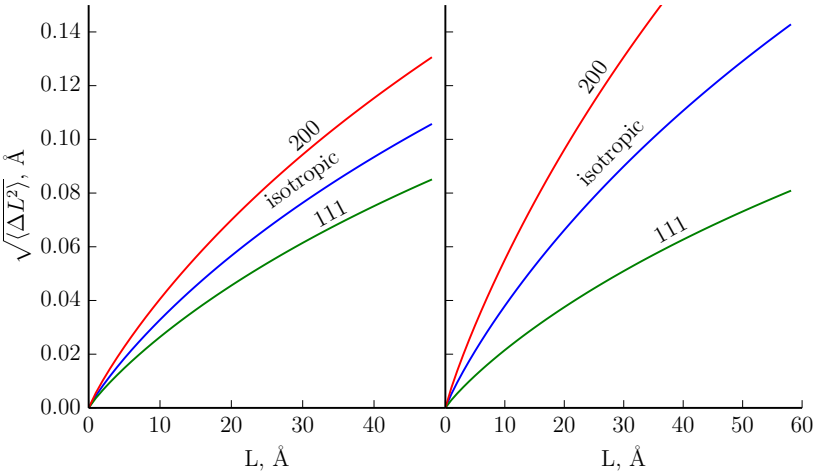

Figure 4.17: Warren's diagram for Ag (left) and Pb (right) spheres (6 unit cells radius), considering an anisotropic RMSD model (see text for details). *Adapted from [46].*

to Warren's theory),

$$\sqrt{\langle \Delta L^2 \rangle} = L\sqrt{\langle \varepsilon^2 \rangle}. \tag{4.13}$$

Diagrams referring to an isotropic model, where the invariant form of Miller indices $(A + BH)$ is used with $B = 0$, are shown in figure 4.16a for the smallest spheres. In any case, the effect follows similar trends for larger spheres, but with much smaller absolute values. Based on figure 4.16a and figure 4.16b, microstrain and anisotropy range from the lowest level, for Rh, characterized by the largest Young modulus and small Zener ratio (Zr $= 2c_{44}/(c_{11} - c_{12})$, one for the isotropic case), to the highest values, for Pb, with the smallest Young modulus and highest Zener ratio.

With the anisotropy taken into account ($B \neq 0$), the analysis presented above can be repeated for each different crystallographic direc-

tion. Only extreme cases for the fcc metals are considered, corresponding to the elastically soft ($h00$) and stiff directions (hhh), with the isotropic and all other values laying in between, as shown in figure 4.17. In terms of quality of line profile modeling, considering the anisotropy gives a modest improvement. Consistently with the amount of strain, Pb and Rh are again the two extremes (see figure 4.16b), with the former the most affected by strain anisotropy. Numerically, Goodness of Fit (GoF) improves of 3.33% for Pb and just 0,04% for Rh, with the other metals lying in between.

4.3.2.4 A direct space view of displacement

Modeling the effect of the complex atomic displacement resulting from lattice relaxation in the framework of a RS approach is far from being trivial; the DS approach is inherently more appropriate, being the signal from each atomic pair computed. The left part of figure 4.18a reports a modeling of an *average-position* sample (Ag, 6uc radius), obtained applying the DSE to generate the powder pattern of an *as-built* aggregate, and perturbing atomic positions by means of equation 4.6[†]. The radial deformation, computed applying equation 2.18, measured for the *average-position* aggregate and for the object generated by the modeling procedure is reported in figure 4.18b as a function of the atomic coordination. A complementary view underlying the complexity of the displacement field is shown in figure 4.18c, where the radial deformation is plotted against the most natural variable, the radial position of a given atom in its reference *as-built* configuration. Particularly, figure 4.18b illustrates that, although the average value of the strain (circles) is roughly reproduced by the model, the standard deviation (bars) of the strain distribution for a given coordination value is underestimated. As expected, worst case scenario is given by the smallest Pb sphere (6uc radius). Even if the quality of the fit is definitely worse than for the Ag case, it is still remarkably good with respect to the one obtained by WPPM.

[†]This was actually a slightly different formulation [103], a bit less accurate but nevertheless appropriate for the sake of the discussion

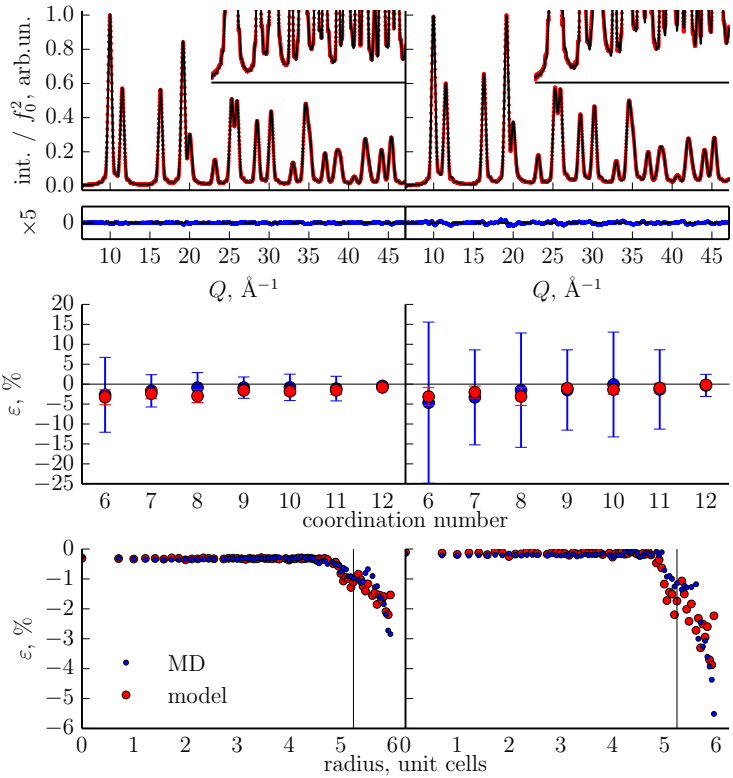

Figure 4.18: Modeling of DSE patterns computed from *average-position* configuration of Ag (left; $NRSS = 1.3{\times}10^{-11}$) and Pb (right; $NRSS = 4.1{\times}10^{-11}$) aggregates; the inset shows a magnification of the region of the pattern whereas the residual is shown above. Radial deformation as a function of the numbers of nearest neighbors is also shown (middle): points represent average values, bars standard deviation. Radial deformation is also shown along radial direction (bottom). In each figure, blue curves represent deformation calculated for the *space-averaged* object, whereas red points shown the result obtained by fitting equation 4.6 to the DSE output. Vertical lines represent the interface between fully-coordinated and under-coordinated atoms. *Adapted from [46].*

4.4 Conclusions and outlook

Several static and dynamic effects emerging from MD simulations of small, clean, metal NP have been discussed and their strong correlation with atomic coordination and elastic properties underlined. A simple expression for atomic displacement arising from relaxation of forces at the particle/environment interface, based on above concepts, has been formulated and tested against the pattern computed from the DSE of simulated particles. While it is not possible for the model to describe localized features arising from particular geometrical conditions, nevertheless it provides a reasonable description of the deformation of a NC. In principle, the degree of accuracy can be further increased if, after atomic positions are adjusted by the model, some energetic criterion is applied to fine-adjust them.

Considerations presented here give just a flavor of the complexity of dealing with NCs. More details have been investigated and currently the effort is in including a physical environment in the discussion, particularly oxygen and capping agents [147, 148].

Chapter 5

Modeling scattering data

Concepts and physical models illustrated so far have been implemented in the stochastic real-space modeling (StoRM)[†] algorithm [149], released under the GNU general public license (GPL) version 3 [150]. The philosophy underlying StoRM grants dignity to data and therefore no manipulation is performed while trying to generate a plausible model.

5.1 The modeling engine

StoRM relies on a *stochastic* engine to model data. A considerable quality of *Monte Carlo* methods (see *e.g.* [151]) is the ability to escape *local minima*, provided the number of iterations is *substantial*.

At a given iteration k, the configuration is devised according to a set of parameters (ψ_k, with ν varied parameters) and the *energy* of the configuration is computed,

$$\chi^2_k = \frac{1}{P-\nu}\sum_{p=1}^{P}\left(\frac{I_{k,p}-I_{o,p}}{\sigma_p}\right)^2. \tag{5.1}$$

Above equation conveys the difference between intensity observed (I_o) and computed for a given model (I_k), normalized to the standard un-

[†]actually, *direct-space* is more appropriate than *real-space* but the latter contributes to build a dandy acronym

certainty (σ) and integrated over the pattern (P points). Given the true intensity (I_t), ideally obtained by repeating the measurement an infinite number of times, the normalization factor is related to the observed intensity by the expression

$$I_o = I_t \pm \sigma. \tag{5.2}$$

If individual photons are counted (pulse counting), then $\sigma^2 = I_o$. In the astonishing event that the intensity computed from the model equals the true intensity, χ^2 will equal one (it follows from inserting equation 5.2 in equation 5.1). A sublime discussion on implications of χ^2 being different from one, among other important concepts, is given by B.H. Toby in [152].

Consistently with the Metropolis-Hastings algorithm [5, 153], the transition from state $k-1$ to state k is accepted with the probability

$$\Pr\left[k-1 \longrightarrow k\right] := \begin{cases} 1, & \text{if } \chi_k^2 < \chi_{k-1}^2 \\ \exp\left(-\dfrac{\chi_k^2 - \chi_{k-1}^2}{c}\right), & \text{otherwise.} \end{cases} \tag{5.3}$$

The bigger the energy-like term c, the higher the probability for a transition to be accepted. The normalization factor can be lowered as the algorithm evolve, like in the *simulated annealing* procedure [154–156]. This way, the probability for a higher-energy configuration to be accepted decreases while iterating. The analogy is the annealing process in condensed matter physics, used to reduce the number of defects of a given microstructure, including grain surface.

A set of parameters ψ is generated at every iteration k (see line 6 in algorithm 5.1) according to

$$\psi_k^{(\alpha)} = \psi_\eta^{(\alpha)} + \mathrm{U}\left([0,1]\right) \Upsilon^{(\alpha)} \quad \in \Psi^{(\alpha)}, \tag{5.4}$$

being $\mathrm{U}\left([0,1]\right)$ a random number uniformly distributed in $[0, 1]$, Υ the step size for the given parameter α, allowed to take any value in Ψ. The label η indicates the last accepted set.

Practically, the loop in the algorithm 5.1 proceeds until a good enough value of χ^2 is achieved or a maximum number of iterations is performed. The simulated annealing algorithm is sketched in algorithm 5.1.

Algorithm 5.1 Outline of the simulated annealing algorithm

1: $k \leftarrow 0$ ▷ iteration number
2: $c \leftarrow c_0$ ▷ initial control parameter
3: $\psi \leftarrow \psi_0$ and $\chi^2 \leftarrow \chi^2_0$ ▷ initial configuration and its energy
4: **while** χ^2 is not satisfactory **do**
5: $k \leftarrow k + 1$
6: ψ_k and χ^2_k ▷ propose a new configuration
7: **if** $\Pr[k-1 \longrightarrow k] > \mathrm{U}([0,1])$ **then** ▷ equation 5.3
8: $\psi \leftarrow \psi_k$ and $\chi^2 \leftarrow \chi^2_k$ ▷ update configuration
9: **end if**
10: $c \leftarrow f(k)$ ▷ update c according to the *cooling schedule*
11: **end while**

5.1.1 Parameters

The way the algorithm walks on the χ^2 surface determines the number of iterations to locate an acceptable solution. The former, in turn, depends on the step size for a given parameter, guessed at the beginning of the modeling and potentially inappropriate.

5.1.1.1 Tuning

The general behavior of the algorithm consists in simultaneously evolving all parameters at a given iteration. However, after M steps and for m iterations, $\alpha - 1$ parameters are fixed and the potential energy surface is sampled only along dimension α.
At this stage, the algorithm attempts to guarantee a global acceptance ratio of the order of $1/2$ by tuning the step size of the parameter α,

$$\Upsilon_T^{(\alpha)} = \Upsilon^{(\alpha)} \begin{cases} (1-\gamma), & \text{if acceptance ratio} < 1/2 \\ (1+\gamma), & \text{if acceptance ratio} > 1/2, \end{cases} \tag{5.5}$$

being γ the tuning coefficient, usually something in the order of 10^{-1}.

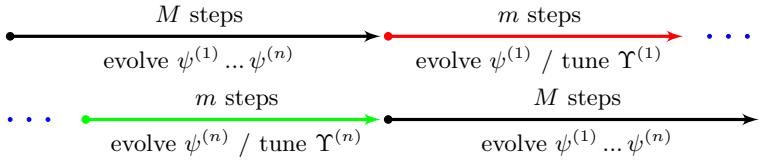

Figure 5.1: Schematic of the procedure used to tune the step size vector.

5.1.1.2 Resolution

Provided a reasonable guess of the solution generated from $\psi_b^{(\alpha)}$, an estimate of the *resolution* of each parameter can be evaluated by numerically solving the equation

$$\Delta_{\pm}\psi^{(\alpha)} = \left[\psi^{(\alpha)}\left(\chi_b^2 \pm \chi_d^2\right)\right]_{A\setminus\{\alpha\}}, \tag{5.6}$$

being χ_d^2 the maximum acceptable displacement from the best value and A the complete set of parameters. Therefore, the intersection of each axis of the parameter space and of an iso-χ^2 surface is computed. Although this procedure implicitly assumes *uncorrelated* parameters, still it provides an indication of the effect of displacing a parameter from its best value and it contributes other information which can be drawn by inspection of a suitable projection of the iso-surface.

5.1.2 Programming

StoRM mainly adheres to the C++11 standard [157], although the C-style is often preferred. Heavy-parallel tasks, as discussed in subsection 3.2.1, are programmed using the compute unified device architecture (CUDA) language [158] and spread across a large number of hosts exploiting the MPI [77]. Pre- and post-processing chiefly relies on the Python programming language [159].

5.1.3 Alternative engines

Other algorithms to probe the energy landscape which are currently under evaluation are *replica exchange* [160, 161], *metadynamics* [162] and an hybrid Monte Carlo/non-linear least squares method.

5.2 Truncated palladium nanocubes

● ○ ● ○ ● *Part of this section has been adapted from [104].*
Rather than pedantically describe all features in StoRM, the general workflow is discussed around a case study.

Small metallic crystals for catalysis

A great effort is nowadays devoted to understand morphology-dependent catalysis processes [163–170]. As discussed in section 4.1, the actual arrangement of atoms within NCs is more complex than the ideal (traditional) polyhedral model crystals, especially in the under-coordinated surface region. This non-idealized atom arrangement and the underlying electronic redistribution directly influences the binding energies of adsorbates, intermediates, and products along reaction pathways on catalytic surfaces [171–175].

Electron microscopy is amazingly contributing to the characterization of NCs, supported by the development of aberration-corrected scanning transmission electron microscopy (TEM) and high angle annular dark field (HAADF) imaging [125, 176–183]. Although microscopy offers the highest spatial resolution, down to the atomic scale [184], only a few NCs represent the entire population, therefore limiting the statistical basis [178, 185]. In addition, the electron beam can damage the sample or induce structural transformations [105, 186, 187] and the operation under vacuum conditions may induce differences with respect to the actual *in operando* environment.

Impressive three-dimensional morphological information together with a spatially resolved map of lattice strain projected on a given crystallographic direction is available by CXD. While this technique can virtually operate in any environment, the smallest NCs which can be investigated using currently available instruments are about 60nm in diameter [188]. Smaller crystalline sizes create considerable and still unsolved challenges in terms of counting statistics and radiation dose [189]. These constraints are likely to be alleviated by "next" generation light sources, X-ray free-electron lasers (XFELs) [190].

The centenarian technique of powder diffraction (PD) can play an important role in the quest for resolving structure and dynamics of NCs.

Truncated palladium nanocubes Cubic palladium NCs are widely investigated system in catalytic applications [167, 168, 191]. As shown in figure 5.2, electron microscopy (EM) is an invaluable tool to assess morphological properties. In particular, a glimpse allows to appraise that NCs are very similar (figure 5.2ab) and that edges and corners are truncated (figure 5.2d). External shape is therefore not only framed by (100) planes, but also includes fractions of (110) and (111) planes.

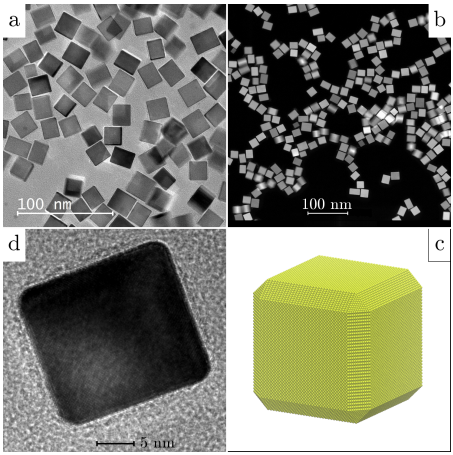

Figure 5.2: TEM (a,d) and HAADF (b) images of palladium NCs. A particle with [00h] perpendicular to the sample holder and clearly exhibiting truncated edges and corners is shown in (d). *Adapted from [104].*
A typical atomic aggregate (c) used as input for StoRM is also depicted.

5.2.1 Atomistic model

The building block of StoRM is merely a set of atomic positions in DS, as depicted in figure 5.2c. Coordinates can be generated according to crystallographic rules or by atomistic simulations (see chapter 2). Each point is associated with the correct (spherical) atomic form factor and the intensity distribution computed applying methods described in chapter 3. Ideally, shape and size of the atomic aggregate should be inferred from EM data.

5.2.2 Morphological dispersion

> Imaging of very small individual particles is generally limited by radiation effects, independently of whether X-rays or electrons are used. [...] Crystallography, in which 10^{12} copies of the specimen are imaged in parallel, is one way around the dose problem, but it can only be applied to structures that can be prepared in identical copies; [...].
>
> I.K. Robinson, 2008 [67]

Consider a cylindrical region with radius $R = 0.4$mm and height $H = 1.5$mm, filled with small cubes with edge $e = 15$nm and at a packing fraction of $\Phi = 5 \times 10^{-4}$. The number of particles inside the region can be roughly estimated, as the ratio between the volume of the cylinder ($V_c = \pi R^2 H$) and the volume of the particle normalized over the packing fraction ($V_p' = e^3/\Phi$), to be in order of $V_c/V_p' \approx 10^{11}$.

At first glance, PD is the ideal tool to investigate NCs since an enormous (and representative) amount of particles simultaneously contribute the experimental pattern (i) granting statistical validity to the experiment. To be added, (ii) the information spread over a large portion of RS (therefore projected over different crystallographic directions) are available as condensed onto a single line.

Curiously, advantages and disadvantages coincides in PD. In general, NCs are far from being *identical copies*: (i) the more *disperse* the sample (in terms of shape and size), the larger the "blurring" of information. This concept is clarified in figure 5.3 where the PD patterns, normalized over scatterers, of the fcc particle depicted in figure 5.2c and for a distribution of objects with same shape and different sizes are shown. It is of particular interest to evaluate the smoothing effect on the {200} reflection. In effect, the powder integration preserves the visibility of fringes related to distance between cube faces, since as sketched in figure 5.4, they are locally (approximately) tangent to the powder sphere.

In principle it is still possible to accurately model data, although dealing with a growing number of variables. Furthermore, (ii) handling a collapsed version of the RS requires strong physically-sound models, together with informations from supporting techniques like EM, in

order to extract meaningful quantities.

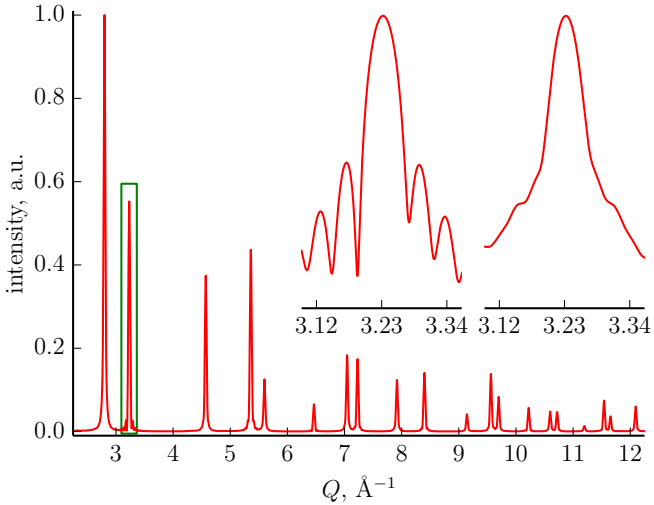

Figure 5.3: DSE pattern of the particle depicted in figure 5.2c (15.0nm edge). A magnification of the {200} reflection (green rectangle) is reported (inset, left) together with the same peak obtained by summing the intensity scattered by fifteen particles, ranging from 9.6 to 20.5 nm edge, normalized to the number of scatterers (inset, right).

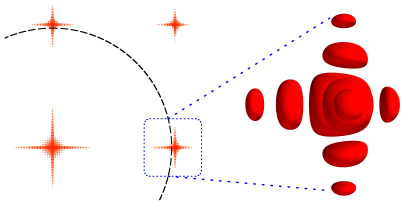

Figure 5.4: A $\{hk0\}$ RS cut schematically depicting the powder diffraction sphere (black, dashed), centered on $(0, 0, 0)$ and intersecting the {200} reflection (magnified on the right) of a fcc cubic crystal. *Adapted from [104].*

5.2.2.1 Ensemble strain

Consider the same distribution of particles introduced in figure 5.3 and suppose that the lattice parameter (a') of each particle is slightly different one from the other. From the Young-Laplace equation (4.1) the pressure on the surface of a spherical particle of radius R can be estimated as a function of the surface energy (γ). This pressure can in turn be related to the lattice parameter deformation by [192]

$$\frac{\mathrm{a}' - \mathrm{a}}{\mathrm{a}} = \frac{2}{3}\frac{\gamma}{\mathrm{K}R}, \tag{5.7}$$

being a the lattice parameter of the associated "bulk" phase and K the bulk modulus (values for palladium are reported in table 5.1). Equating the surface area of a sphere of radius R and of a cube of edge e leads to the relation $R = e\sqrt{3/2\pi}$, to be substituted in equation 5.7,

$$\frac{\mathrm{a}' - \mathrm{a}}{\mathrm{a}} = \frac{2}{3}\sqrt{\frac{2\pi}{3}}\frac{\gamma}{\mathrm{K}e}. \tag{5.8}$$

Figure 5.5 depicts (i) a DSE pattern computed for fifteen particles, ranging from 9.6 to 20.5nm edge, sharing the same lattice parameter a = 3.887596Å and (ii) another pattern calculated for the same set but with each particle being described by a different lattice parameter, ranging from 3.886429 to 3.888326Å according to equation 5.8. As demonstrated by the difference between the two curves, even if each particle in the ensemble is actually undeformed with respect to its crystallographic counterpart, a *strain-like* effect insists on the powder pattern and has to be taken into account when modeling scattering data from an ensemble of NCs, the effect being more pronounced the wider the size distribution.

a, Å	$\gamma_{(100)}$, Jm^{-2}	s_{11}	s_{12}	s_{44}, TPa^{-1}	K, GPa
3.890	1.645	12.06	-5.178	14.045	180

Table 5.1: Some physical properties of palladium [115, 193]. From the left, (i) bulk lattice parameter at 300K, (ii) surface energy for the (100) interface with vacuum, (iii, iv, v) compliance tensor coefficients at 0K, (vi) bulk modulus.

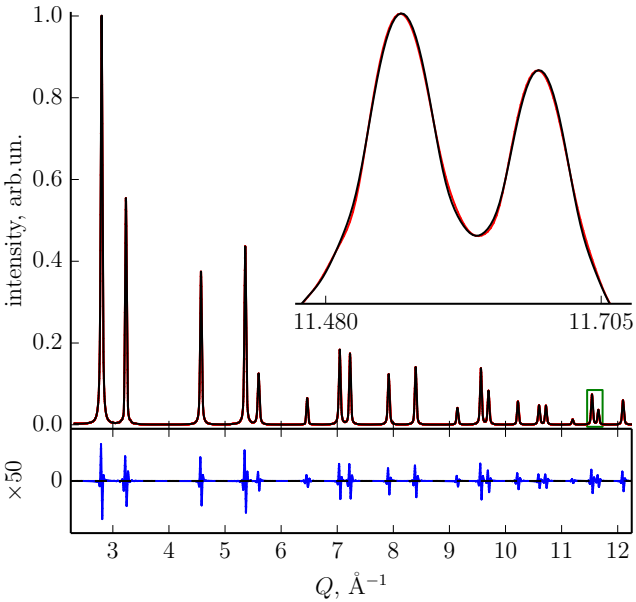

Figure 5.5: Sum of the DSE patterns of fifteen particles, from 9.6 to 20.5nm edge, (black) sharing the same lattice parameter and (red) described by a one calculated according to equation 5.8. The inset shows a magnification of peaks inside the green box. Below, the difference between the two curves.

5.2.3 Powder diffraction pattern

Interestingly, the current trend of nanotechnology is toward the production of NPs with *identical* size and shape. Under these conditions powder diffraction can offer detailed information, in a certain sense similar to those offered by "imaging techniques", affording access to structural details of NC size, shape, and atomic displacement simultaneously along many crystallographic directions.

The beamline 11BM at the Advanced Photon Source [194, 195] was employed to analyze palladium NCs shown in figure 5.2, synthesized by the C.-K. Tsung group at Boston College[†]. The (transmission)

[†]B.T. Sneed, M.K. Sheehan and C.-K. Tsung (details in [104])

Debye-Scherrer geometry [196] was adopted and the sample loaded in a $R = 0.4$mm Kapton® capillary, spun at 4,200rpm to improve statistics. The beam, characterized by a wavelength of $\lambda = 0.0413874$nm, had a footprint of approximately $H = 1.5$mm times the diameter of the capillary. Two measurements of one hour each were performed at room temperature ($T = 298$K), counting 0.3s for every point. The instrumental resolution was amplified with a detection system based on 12 independent Si(111) analyzers.

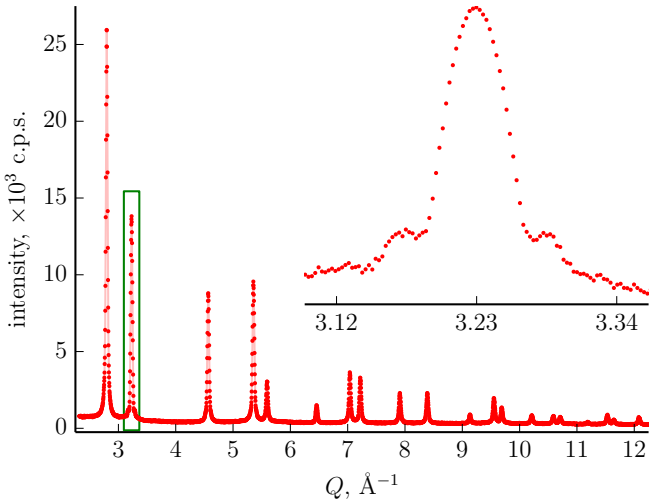

Figure 5.6: Experimental PD pattern of palladium NCs together with (inset) a magnification (semi-log plot) of the region around the (200) reflection (inside a green box) showing fringes related to cube faces separation.

Collected data were binned so to further lower the signal-to-noise ratio; the pattern obtained is reported in figure 5.6, extending from $Q \approx 2.3$ to 12.3Å^{-1}. The inset reports a magnification (semi-log plot) of the region around the (200) reflection showing fringes as a fingerprint of the cubic shape (and of the relatively narrow size distribution, as discussed in subsection 5.2.2). It is worth nothing that information projected along 15 crystallographic directions are encoded in the experimental set, one for each independent Bragg reflection.

5.2.3.1 Instrumental contribution

The underlying principle of the presented approach is that experimental data quality has to be excellent: speculations must concern the sample and not the instrument. Lowest instrumental resolution of 11BM in the probed Q-region is $\Delta Q \approx 2.5 \times 10^{-3}$, *i.e.* approximately fifteen times smaller than the full width at half maximum of the narrower Bragg peak associated to the sample.

Apart from assessing the beam wavelength by measuring the NIST SRM-660b LaB_6 standard [197, 198] in this study no correction is attempted for instrumental resolution. Although it seems reasonable to safely neglect the role of the instrument given the efficiency of the probe, further investigations are currently carried out in order to properly account for subtle effects.

5.2.3.2 Background

The Kapton® holder obviously contributes the scattered intensity and needs to be properly accounted for when modeling data. For this purpose, an empty capillary was measured at 11BM and fitted using a mixture of mathematical functions, namely pseudo-Voigt curves and Chebyshev polynomials.

Pseudo-Voigt J.I. Langford proposed the employ of the Voigt function, the convolution of m Cauchy (Lorentzian) and n Gaussian curves sharing a common origin, for interpreting the breadths of diffraction profiles [199]. To avoid the convolution, the flexible pseudo-Voigt function can be defined as a linear combination of those curves. StoRM implements the normalized for unit height form (see *e.g.* [200]),

$$pV\left(2\Theta; 2\Theta_c, \omega, \eta\right) = \frac{\eta}{1 + \left(\dfrac{2\Theta - 2\Theta_c}{\omega}\right)^2} + (1-\eta)\exp\left(-\ln 2\left[\frac{2\Theta - 2\Theta_c}{\omega}\right]^2\right), \tag{5.9}$$

multiplied by the parameter ι which has the physical units of the measured intensity. In the above equation, the quantity $2\Theta_c$ indicates the position of the centroid of the peak, characterized by the $FWHM = 2\omega$, and η the mixing parameter.

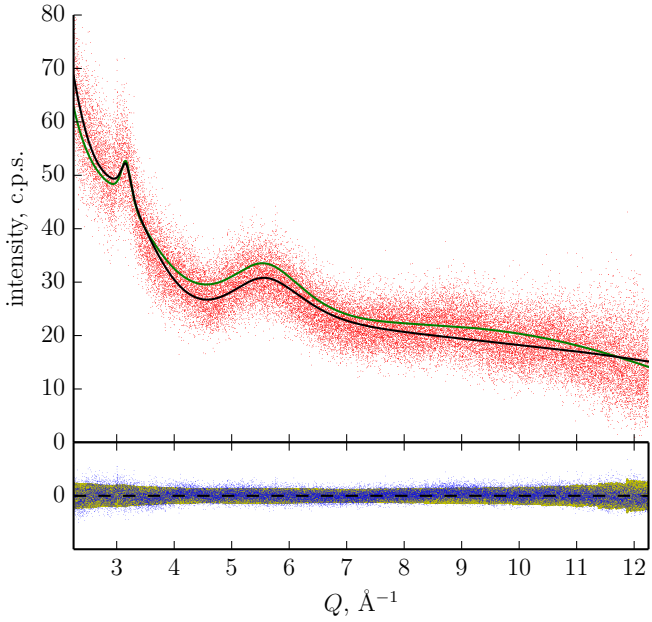

Figure 5.7: Experimental scattering pattern of an empty Kapton® capillary (red dots) reported together with the optimized fitting function (black line, $\chi^2 \approx 0.7$) and residual intensity (blue dots). The yellow region includes values within plus and minus the standard uncertainty whereas green line represents the background function obtained after modeling of the signal emanated from palladium NCs (see text for details).

Chebyshev polynomials Chebyshev polynomials of the first kind [201] can be defined by the recurrence relation,

$$T_k(x) = 2x\,T_{k-1}(x) - T_{k-2}(x) \qquad k \geq 2, \tag{5.10}$$

where $T_0(x) = 1$ and $T_1(x) = x$. StoRM implements a function based on above polynomials, obtained by remapping the domain on $[-1, 1]$,

$$x = 2\,\frac{2\Theta - 2\Theta_{min}}{2\Theta_{max} - 2\Theta_{min}} - 1, \tag{5.11}$$

being $2\Theta_{min}$ and $2\Theta_{max}$ the smallest and largest values of 2Θ, and multiplying the k-th term by the (fitting) coefficient a_k,

$$C_\kappa\left(2\Theta; a_0, ..., a_\kappa\right) = \sum_{k=0}^{\kappa} a_k T_k \left(2\,\frac{2\Theta - 2\Theta_{min}}{2\Theta_{max} - 2\Theta_{min}} - 1\right). \tag{5.12}$$

Fitting the signal emanated by an empty Kapton® capillary Seven pseudo-Voigt functions (equation 5.9, 7×4 varied parameters, vps) were added to a fourth order Chebyshev polynomial (equation 5.12, 5 vps) to create the fit function f_b. StoRM was employed to model the experimental pattern, collected at the same temperature and implementing the same geometry defined in subsection 5.2.3. The beam wavelength was $\lambda = 0.0412225$nm and the counting time 0.1s per step. The optimized fitting function ($\chi^2 \approx 0.7$) and the experimental pattern are reported in figure 5.7.

Background modeling To account for, *exempli gratia*, the capillary being not empty or the likely presence of some carbonaceous production leftovers contributing the scattered intensity, the *background function* is defined as a perturbation of the fit function,

$$\mathcal{B}\left(2\Theta; \iota, a_0, a_1, a_2, a_3\right) = \iota\, f_b\left(2\Theta\right) + C_3\left(2\Theta; a_0, a_1, a_2, a_3\right). \tag{5.13}$$

The above is added to the output of the DSE and contributes six vps when modeling palladium NCs. The background function, normalized by ι, is reported in figure 5.7 together with the fit function f_b. Interestingly, the difference between the two functions is relatively modest therefore validating the robustness of the above-described procedure. It is also worth nothing that the contribution of the capillary to the scattered intensity is much smaller than the signal due to palladium NCs, as demonstrated by figure 5.6.

5.2.3.3 Absorption

The measurement of the transmittance of the intensity when the detector is aligned with the impinging beam (I_0) permits to asses sample absorption by means of the equation (see *e.g.* [202])

$$T = \frac{I}{I_0} = \frac{1}{V}\int_V \exp(-\mu l)\ \mathrm{d}V = 0.974 \tag{5.14}$$

being I the transmitted beam, V the volume of the sample with l the path length of the beam in the crystal, and μ the linear attenuation coefficient. Although in this particular case the transmitted fraction is so close to unity ($\mu R \approx 0.01$) that any correction is practically unnecessary, StoRM can model absorption contribution by numerically solving equation 5.14 applied to the case in equatorial plane of cylinder of radius R within the X-ray beam [202]

$$T(\Theta) = \frac{1}{\pi R^2}\int_{r=0}^{R}\int_{\phi=0}^{2\pi} \exp\Bigg(-\mu\left[\sqrt{R^2 - r^2\sin^2(\Theta+\phi)} + \sqrt{R^2 - r^2\sin^2(\Theta-\phi)}\right]\Bigg)\cosh(2\mu r\sin\Theta\sin\phi)\, r\,\mathrm{d}r\,\mathrm{d}\phi \tag{5.15}$$

where ϕ is the azimuthal angle. Following the approach by Bowden and Ryan [203], the contribution of the sample holder (capillary) can also be taken into account by suitably expressing the path length of the X-ray beam. Consistently with the general philosophy of StoRM, absorption coefficients must be provided (*i.e.* they are not fitting parameters), together with geometrical characteristics of the sample holder.

Absorption can dramatically affect experimental data both by (i) modifying scattered intensity and, in the severest cases, by (ii) giving rise to a slight Θ-dependent displacement of data [204]. Given the transmittance of the impinging beam, the packing fraction for the presented case can be estimated (see subsection 5.2.2) to be $\Phi \approx 5\times10^{-4}$, approximately a thousand times smaller than for a micron-sized powder. The low density value likely arises from the complexity of uniformly filling the capillary with a powder of NCs and from the possible presence of carbonaceous production leftovers.

5.2.4 The sample

A plausible model of scattered signal from the so-far described system is reported in figure 5.8. The result, in the framework of the DS approach is a distribution (any probability curve or a histogram) of particles, composed of atoms deformed (according to the model described by equation 4.6, in this case) with respect to a reference, crystallographic configuration. Interestingly, deformation generated by the underlying physical model can be directly visualized as a displacement or a strain field, according to methods presented in chapter 2.

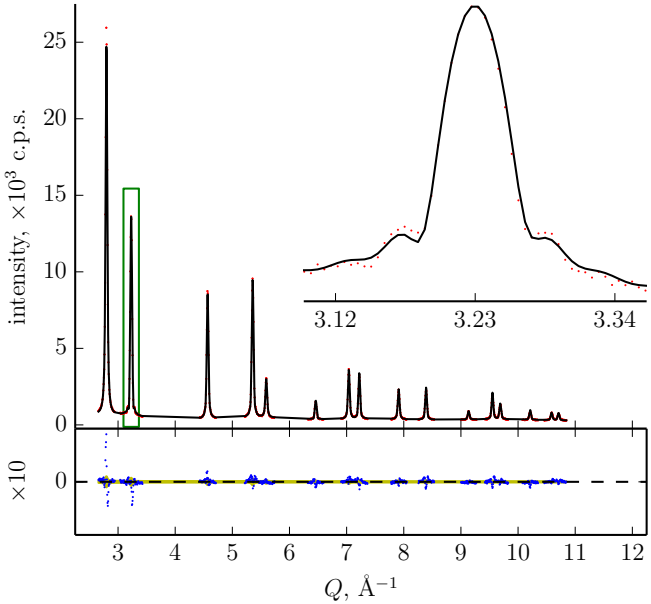

Figure 5.8: Experimental scattering pattern of a set of palladium NCs reported together with a plausible model.

Exempli gratia, figure 5.9 reports the strain field (equation 2.16) predicted by StoRM for one of the particles belonging to the set. Moreover, the model implemented by the algorithm for considering the effect of atomic vibrations provides an estimate of MSD and of the average degree of correlation among oscillations.

Parameters varied during modeling are reported in table 5.2, together with a minimalistic comment.

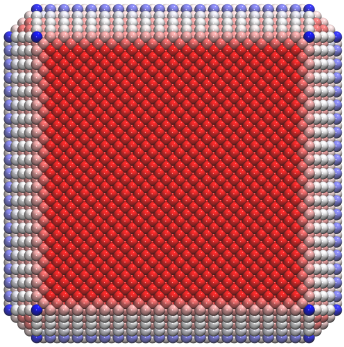

Figure 5.9: Color map for one of the particles belonging to the set used as input for StoRM, useful to visualize the strain-field obtained by fitting the model described by equation 2.13 to experimental data. It is interesting to notice that the larger deformation (blue) affects less-coordinated atoms.

Young-Laplace law for size-dependent properties In 5.2.2.1 the need for considering properties to change within a sample has been explained. To this purpose, a Young-Laplace law (see equation 4.1) has been implemented to map the given (structural or dynamical) property ϕ on different sizes,

$$\phi = \phi_0 + \frac{\phi_s}{s}, \tag{5.16}$$

being s the size of the aggregate (the edge of the cube in this case), ϕ_0 and ϕ_s the fit parameters. This further relation, for example, assigns a different strain field to a different particle. In the case of equation 4.6, both the "Pauling term" σ and the constant offset a vary according to the Young-Laplace law. Interestingly, one can try connecting *sigma* and a to surface energy or bulk modulus by equating equation 5.16 to equation 4.2 and equation 5.7, respectively.

vps	role
6	background, see subsection 5.2.3.2
13(3)	morphology, histogram (probability distribution)
3	deformation, equation 4.6
+2	for mapping values on different sizes, equation 5.16
16(2)	atomic vibrations (reduced model)
+1	for mapping one value on different sizes, equation 5.16

Table 5.2: Number of parameters varied (vps) during modeling of data with a concise comment on their role. In parenthesis, alternative, simplified formulations useful to approach a fair approximation of the best solution.

5.3 Conclusions and outlook

The PD pattern of a billion-sized population allows for accurately assessing structural and dynamical properties of palladium nanocubes. Particularly, "defocus" of information due to morphological dispersion is reduced by relatively narrow size and shape distributions of particles composing the sample, therefore emphasizing the duality of the DSE approach. While the *greatest flexibility* is offered since one is dealing with single atoms, computing the interference of each results in the *stiffest* approach, which provides accurate data only if each subtle feature discussed so far is properly taken into account.

Although the investigation presented in this chapter is far from being completed, nevertheless it offers a perfect framework to present the philosophy underlying StoRM, condensing concepts presented through this thesis.

Further actions should be carried out to improve the model. Particularly, (i) the beamline has to be better characterized and instrumental resolution taken into account. In fact, the DSE is a *total scattering* technique and ideally requires no aberration to affect experimental pattern. Next, to boost the value of the approach applied to this case of study, (ii) an ongoing high-resolution transmission electron microscopy (HRTEM) campaign will provide enough data for a statistically-sound

comparison of size and shape. Last, (iii) for Monte Carlo methods to converge to a plausible minimum of the potential energy surface (and provide a solid guess of the resolution of each parameter) many iterations are needed. This consideration permits to emphasize a drawback of the presented approach: the computational cost. In this specific case, every iteration consists in evaluating something in the order of the number of points composing the pattern times the squared number of atoms in each particle (approximately half a million in the worst case). However, as discussed in subsection 3.2.1, the future seems to be more than promising, from this point of view.

Chapter 6

Outlook

Third- and fourth-generation light sources have granted a tremendous evolution to scattering techniques, lighting up details at the atomic scale thanks to the unprecedented spatial and temporal resolution. Theoretical methods should improve accordingly, progressively relieving approximations which are consistent with less accurate experimental techniques. The propensity for an *atomistic approach* to scattering ideally fits the case of nanostructured materials, intrinsically lacking symmetry arguments invoked by traditional approaches, and provides a natural framework for atomistic simulations.

While through this thesis simulations have been mainly employed to generate plausible models so to improve the understanding of observed patterns, in principle they could actively take part in the modeling procedure: provided an appropriate description of atomic interactions, they could in fact supply energetic constrains for the modeling engine.

To reliably assess properties, the point of view of other techniques should be adopted. Interestingly, observables related to a broad range of experiments can be calculated within a common, *unified framework* based on the fact that we are dealing with atoms and electrons. *Exempli gratia*, for the ideally complementary technique to X-rays (or neutrons) scattering, transmission electron microscopy, different approaches exist for computing images (see *e.g.* [205]). Analogously, absorption and vibrational spectroscopies can be calculated, for example, in the framework of the time-dependent density functional theory [206].

The link among techniques is not easy to define, the most straightforward option implicitly presented in the case of study in section 5.2, parallels multi-scale methods where one technique (HRTEM, which provides valuable information on morphology and defects) informs another one (XRPD, statical and dynamical information with a large statistical basis).

Computational physics has greatly evolved in the last decades, continuously providing new tools and theories with increasing level of accuracy; to name but one the Car-Parrinello method [207], integrating classical molecular dynamics by explicitly including the electrons as degrees of freedom.

On the other hand, computing power tremendously increases over time. The powerful IBM-704 (see the historical note in chapter 2) employed by Alder and Wainwright in 1957 [7] computed 7,000 collisions among 32 particles in one hour. This machine was able to perform approximately 4×10^3 floating-point operations per second (FLOPS) [208], approximately nine orders of magnitude less than a single modern graphics processing unit (see table 3.1). In 2008 Germann and Kadau demonstrated the first trilion-atom simulation [209], and predicted the achievement of the centimeter/millisecond scale in 50 to 100 years.

Those considerations foreseen a bright future for computational methods, linking with increasing accuracy theory and experiments therefore providing exceptionally detailed pictures of atomic properties.

Acknowledgements

Many people deserve my gratitude and love, starting from my family, which has been supporting and bearing me for the last (almost) three decades. Good friends (and especially Alberto, Fabio, Matteo and Paolo) and patient roommates (Leonardo, Nico and Stefano) magnificently help in enjoying life, making it easier. Francesca, who suffered me for years, and people sharing the greatest part of each day, notably Cristy, Alberto, Claudia, Matteo, Melanie, Ken, Mirco and Rob. Daniele and Tarcisio are also acknowledged with emphasis.

Tons of other people gravitating around my life are collectively thanked; those enjoying the exertion of hiking, climbing, skiing, mountain-biking and sailing as well as those sharing a beer from time to time.

The open-source community is also acknowledge, always providing exceptional tools and among them, the Debian GNU/Linux operating system and those employed to write/draw pictures reported in this thesis, LaTeX, GIMP [210], Matplotlib [211] and VMD [212].

Some people inspired me in the attempt of doing some "science", motivating in trying to do something meaningful; Prof. P. Scardi, Prof. I.K. Robinson and Dr. A. Kohlmeyer are greatly acknowledged.

A special thought is devoted to Marica, gently and patiently standing me every day.

Abbreviations

Physics

DS	direct-space
RPCF	radial pair correlation function
MSD	mean squared displacement
MMC	Metropolis Monte Carlo
MD	molecular dynamics
PBC	periodic boundary condition
NVE	microcanonical ensemble
NVT	canonical ensemble
EAM	embedded atom method
MEAM	modified embedded atom method
ReaxFF	reactive force field
EM	electron microscopy
TEM	transmission electron microscopy
HRTEM	high-resolution transmission electron microscopy
HAADF	high angle annular dark field
RS	reciprocal-space
DSE	Debye scattering equation
WPPM	whole powder pattern modeling
TDS	thermal diffuse scattering
CXD	coherent X-ray diffraction
XRD	X-ray diffraction
PD	powder diffraction
XFEL	X-ray free-electron laser
NP	nanostructured particle
NC	nanostructured crystal

StoRM	stochastic real-space modeling

Computer Science

CPU	central processing unit
GPU	graphics processing unit
FLOPS	floating-point operations per second
FFT	fast Fourier transform
GPL	GNU general public license
CUDA	compute unified device architecture
MPI	message passing interface

Symbols

$\mathbb{Z}$	set of integers
$\imath$	imaginary unit, $\sqrt{-1}$
$\mathrm{U}([0,1])$	random number uniformly distributed in [0, 1]
$\mathrm{sinc}(x)$	$\sin(x)/x$
$\mathcal{F}$	Fourier transform operator
$\|\mathbf{v}\|$	l^2-norm, $\sqrt{x_1^2+x_2^2+x_3^2}$ for real vectors
$\hat{\mathbf{v}}$	unit vector, $\mathbf{v}/\|\mathbf{v}\|$
$\mathcal{P}_{\hat{\mathbf{n}}}(\mathbf{v})$	projection of $\mathbf{v}$ onto $\hat{\mathbf{n}}$, $(\mathbf{v}\cdot\hat{\mathbf{n}})\,\hat{\mathbf{n}}$
$\mathbf{r}$	position vector
$\dot{\mathbf{r}}$	velocity vector
$\mathbf{p}$	momentum vector, $\mathbf{p}=m\dot{\mathbf{r}}$
$\mathbf{N}$	number of atoms
$\mathbf{E}$	total energy
$\mathbf{T}$	temperature
$\mathbf{V}$	volume
$\mathbf{P}$	pressure
$\rho(\mathbf{r})$	electronic density
$g(r)$	radial pair correlation function

$\mathbf{Q}$	wavevector transfer (scattering vector)
Θ	half of the scattering angle
λ	wavelength
$f(\mathbf{Q}, \hbar\omega)$	atomic form factor
$F(\mathbf{Q})$	structure factor
$I(\mathbf{Q})$	intensity distribution
σ	standard uncertainty
Z	atomic number
$\mathcal{N}$	number of nearest neighbors
b	bond length
a	lattice parameter
$\mathcal{S}$	compliance tensor
$\mathcal{C}$	stiffness tensor
s_{ij}	compliance matrix ($\mathcal{S}$) element
c_{ij}	stiffness matrix ($\mathcal{C}$) element
Zr	Zener ratio, $2c_{44}/c_{11} - c_{12}$
$\mathrm{E}_{\hat{\mathbf{v}}}$	Young's modulus for a given direction
K	bulk modulus
γ	surface energy
fcc	face-centered cubic
$\mathbf{r}_0$	reference (as-built) configuration
$\mathbf{r}_\mathrm{d}$	deformed configuration
$\mathbf{u}$	displacement vector, $\mathbf{r}_0 - \mathbf{r}_\mathrm{d}$

$\langle \mathbf{r}\,(t) \rangle_{\mathrm{t}}$	average-position configuration
FWHM	full width at half maximum
vp	varied parameter
$\hbar$	reduced Planck constant[†], $6.58211928\,(15) \times 10^{-16}$eV·s
k_{B}	Boltzmann constant[†], $8.6173324\,(78) \times 10^{-5}$eV·K^{-1}

[†]Datum taken from [213]

Bibliography

[1] P. Buffat and J.-P. Borel. "Size effect on the melting temperature of gold particles". *Physical Review A* **13** (1976), pp. 2287–2298. DOI: 10.1103/PhysRevA.13.2287.

[2] I. Freestone, N. Meeks, M. Sax, and C. Higgitt. "The Lycurgus Cup – A Roman nanotechnology". English. *Gold Bulletin* **40** (2007), pp. 270–277. DOI: 10.1007/BF03215599.

[3] R.P. Feynman, R.B. Leighton, and M. Sands. *The Feynman Lectures on Physics*. Vol. I. Addison-Wesley, 1964.

[4] H.L. Anderson. "Scientific Uses of the MANIAC". *Journal of Statistical Physics* **43** (1986). DOI: 10.1007/BF02628301.

[5] N.C. Metropolis, A.W. Rosenbluth, M.N. Rosenbluth, A.H. Teller, and E. Teller. "Equation of State Calculations by Fast Computing Machines". *The Journal of Chemical Physics* **21** (1953), pp. 1087–1092. DOI: 10.1063/1.1699114.

[6] E. Fermi, J. Pasta, S. Ulam, and M. Tsingou. *Studies of Nonlinear Problems*. Tech. rep. Los Alamos Scientific Laboratory report LA-1940, 1955.

[7] B.J. Alder and T.E. Wainwright. "Phase Transition for a Hard Sphere System". *The Journal of Chemical Physics* **27** (1957), pp. 1208–1209. DOI: http://dx.doi.org/10.1063/1.1743957.

[8] J.B. Gibson, A.N. Goland, M. Milgram, and G.H. Vineyard. "Dynamics of Radiation Damage". *Physical Review* **120** (1960), pp. 1229–1253. DOI: 10.1103/PhysRev.120.1229.

[9] A. Rahman. "Correlations in the Motion of Atoms in Liquid Argon". *Physical Review* **136** (1964), A405–A411. DOI: 10.1103/PhysRev.136.A405.

[10] A. Laio, S. Bernard, G.L. Chiarotti, S. Scandolo, and E. Tosatti. "Physics of Iron at Earth's Core Conditions". *Science* **287** (2000), pp. 1027–1030. DOI: 10.1126/science.287.5455.1027.

[11] D. Frenkel and B. Smit. *Understanding Molecular Simulation: from Algorithms to Applications. 2^{nd} ed.* Vol. 1. Computational Science. Academic Press, 2001.

[12] S. Newton. *Philosophiæ Naturalis Principia Mathematica*. 1687.

[13] M.P. Allen and D.J. Tildesley. *Computer Simulation of Liquids*. Clarendon Press, 1989.

[14] A.R. Leach. *Molecular Modelling: Principles and Applications. 2^{nd} ed.* Ed. by P. Hall. 2001.

[15] F. Ercolessi. *A molecular dynamics primer*. http://www.fisica.uniud.it/~ercolessi/md/, 1997.

[16] D. Chandler. *Introduction to Modern Statistical Mechanics*. Oxford University Press, 1987.

[17] M.E. Tuckerman. *Statistical Mechanics: Theory and Molecular Simulation*. Oxford Graduate Texts, 2010.

[18] E. Schrödinger. "An Undulatory Theory of the Mechanics of Atoms and Molecules". *Physical Review* **28** (1926), pp. 1049–1070. DOI: 10.1103/PhysRev.28.1049.

[19] M. Born and R. Oppenheimer. "Zur Quantentheorie der Molekeln". *Annalen der Physik* **389** (1927), pp. 457–484. DOI: 10.1002/andp.19273892002.

[20] L.-V. de Broglie. "Recherches sur la théorie des quanta". PhD thesis. Faculty of Sciences at Paris University, 1924.

[21] J.C. Maxwell. "V. Illustrations of the dynamical theory of gases. Part I. On the motions and collisions of perfectly elastic spheres". *Philosophical Magazine Series 4* **19** (1860), pp. 19–32. DOI: 10.1080/14786446008642818.

[22] J.C. Maxwell. "Illustrations of the dynamical theory of gases. Part II. On the process of diffusion of two or more kinds of moving particles among one another". *Philosophical Magazine Series 4* **20** (1860), pp. 21–37. DOI: 10.1080/14786446008642902.

[23] L. Verlet. "Computer "Experiments" on Classical Fluids. I. Thermodynamical Properties of Lennard-Jones Molecules". *Physical Review* **159** (1967), pp. 98–103. DOI: 10.1103/PhysRev.159.98.

[24] J.W. Gibbs. *Elementary Principles in Statistical Mechanics, developed with especial reference to the rational foundation of thermodynamics*. Charles Scribner's Sons, 1902.

[25] E.A. Guggenheim. "Grand Partition Functions and So-Called "Thermodynamic Probability"". *The Journal of Chemical Physics* **7** (1939), pp. 103–107. DOI: http://dx.doi.org/10.1063/1.1750386.

[26] H.C. Andersen. "Molecular dynamics simulations at constant pressure and/or temperature". *The Journal of Chemical Physics* **72** (1980), pp. 2384–2393. DOI: http://dx.doi.org/10.1063/1.439486.

[27] L. Boltzmann. *Vorlesungen über Gastheorie*. Vol. 2. Vorlesungen über Gastheorie. J. A. Barth, 1898.

[28] M. Born and T. Von Kármán. "Über Schwingungen in Raumgittern". *Physikalishe Zeitschrift* **13** (1912), pp. 297–309.

[29] S.E. Lennard-Jones. "On the Determination of Molecular Fields. II. From the Equation of State of a Gas". *Proceedings of the Royal Society of London. Series A* **106** (1924), pp. 463–477. DOI: 10.1098/rspa.1924.0082.

[30] M.S. Daw and M.I. Baskes. "Semiempirical, Quantum Mechanical Calculation of Hydrogen Embrittlement in Metals". *Physical Review Letters* **50** (1983), pp. 1285–1288. DOI: 10.1103/PhysRevLett.50.1285.

[31] M.S. Daw and M.I. Baskes. "Embedded-atom method: Derivation and application to impurities, surfaces, and other defects in metals". *Physical Review B* **29** (1984), pp. 6443–6453. DOI: 10.1103/PhysRevB.29.6443.

[32] M.S. Daw, S.M. Foiles, and M.I. Baskes. "The embedded-atom method: a review of theory and applications". *Materials Science Reports* **9** (1993), pp. 251–310. DOI: http://dx.doi.org/10.1016/0920-2307(93)90001-U.

[33] S.M. Foiles and M.I. Baskes. "Contributions of the embedded-atom method to materials science and engineering". *MRS Bulletin* **37** (2012), pp. 485–491. DOI: 10.1557/mrs.2012.93.

[34] M.I. Baskes. "Modified embedded-atom potentials for cubic materials and impurities". *Physical Review B* **46** (1992), pp. 2727–2742. DOI: 10.1103/PhysRevB.46.2727.

[35] A.C.T. van Duin, S. Dasgupta, F. Lorant, and W.A. Goddard. "ReaxFF: A Reactive Force Field for Hydrocarbons". *The Journal of Physical Chemistry A* **105** (2001), pp. 9396–9409. DOI: 10.1021/jp004368u.

[36] K. Chenoweth, A.C.T. van Duin, and W.A. Goddard. "ReaxFF Reactive Force Field for Molecular Dynamics Simulations of Hydrocarbon Oxidation". *The Journal of Physical Chemistry A* **112** (2008), pp. 1040–1053. DOI: 10.1021/jp709896w.

[37] H.M. Aktulga, J.C. Fogarty, S.A. Pandit, and A.Y. Grama. "Parallel reactive molecular dynamics: Numerical methods and algorithmic techniques". *Parallel Computing* **38** (2012), pp. 245–259. DOI: http://dx.doi.org/10.1016/j.parco.2011.08.005.

[38] L. Liu, Y. Liu, S.V. Zybin, H. Sun, and W.A. Goddard. "ReaxFF-lg: Correction of the ReaxFF Reactive Force Field for London Dispersion, with Applications to the Equations of State for Energetic Materials". *The Journal of Physical Chemistry A* **115** (2011), pp. 11016–11022. DOI: 10.1021/jp201599t.

[39] J.T. Su and W.A. Goddard. "Excited Electron Dynamics Modeling of Warm Dense Matter". *Physical Review Letters* **99** (2007), pp. 185003–185006. DOI: 10.1103/PhysRevLett.99.185003.

[40] A. Jaramillo-Botero, J. Su, A. Qi, and W.A. Goddard. "Large-scale, long-term nonadiabatic electron molecular dynamics for describing material properties and phenomena in extreme environments". *Journal of Computational Chemistry* **32** (2011), pp. 497–512. DOI: 10.1002/jcc.21637.

[41] J.Q. Broughton, F.F. Abraham, N. Bernstein, and E. Kaxiras. "Concurrent coupling of length scales: Methodology and application". *Physical Review B* **60** (1999), pp. 2391–2403. DOI: 10.1103/PhysRevB.60.2391.

[42] R.E. Rudd and J.Q. Broughton. "Concurrent Coupling of Length Scales in Solid State Systems". *Physica Status Solidi B* **217** (2000), pp. 251–291. DOI: 10.1002/(SICI)1521-3951(200001)217:1<251::AID-PSSB251>3.0.CO;2-A.

[43] M. Steinhauser. *Computational Multiscale Modeling of Fluids and Solids. Theory and Applications*. Springer, 2008.

[44] S. Baeurle. "Multiscale modeling of polymer materials using field-theoretic methodologies: a survey about recent developments". English. *Journal of Mathematical Chemistry* **46** (2009), pp. 363–426. DOI: 10.1007/s10910-008-9467-3.

[48] L.D. Landau and E.M. Lifshitz. *Theory of Elasticity. 3^{rd} ed.* Vol. 7. Course of Theoretical Physics. Butterworth-Heinemann, 1986.

[49] I.A. Vartanyants and I.K. Robinson. "Partial coherence effects on the imaging of small crystals using coherent x-ray diffraction". *Journal of Physics: Condensed Matter* **13** (2001), pp. 10593–10611. DOI: 10.1088/0953-8984/13/47/305.

[50] M.A. Pfeifer, G.J. Williams, I.A. Vartanyants, R. Harder, and I.K. Robinson. "Three-dimensional mapping of a deformation field inside a nanocrystal". *Nature* **442** (2006), pp. 63–66.

[51] I.K. Robinson and R. Harder. "Coherent X-ray diffraction imaging of strain at the nanoscale". *Nature Matererials* **8** (2009), pp. 291–298.

[52] G. Voronoi. "Nouvelles applications des paramètres continus à la théorie des formes quadratiques". *Journal für die Reine und Angewandte Mathematik* **133** (1908), pp. 97–178. DOI: 10.1515/crll.1908.133.97.

[53] P.A.M. Dirac. *The Principles of Quantum Mechanics. 4^{th} ed.* Oxford University Press, 1958.

[54] J.P. Hansen and I.R. McDonald. *Theory of Simple Liquids. 3^{rd} ed.* Academic Press, 2006. DOI: http://dx.doi.org/10.1016/B978-012370535-8/50000-8.

[55] B.G. Levine, J.E. Stone, and A. Kohlmeyer. "Fast analysis of molecular dynamics trajectories with graphics processing units—Radial distribution function histogramming". *Journal of Computational Physics* **230** (2011), pp. 3556–3569. DOI: http://dx.doi.org/10.1016/j.jcp.2011.01.048.

[56] F. Zernike and J.A. Prins. "Die Beugung von Röntgenstrahlen in Flüssigkeiten als Effekt der Molekülanordnung". German. *Zeitschrift für Physik* **41** (1927), pp. 184–194. DOI: 10.1007/BF01391926.

[57] B.E. Warren. *X-Ray Diffraction*. Dover, 1990.

[58] S. Billinge. "Local Structure from Total Scattering and Atomic Pair Distribution Function (PDF) Analysis". In: *Powder Diffraction: Theory and Practice*. The Royal Society of Chemistry, 2008. Chap. 16, pp. 464–493. DOI: 10.1039/9781847558237-00464.

[59] P.J.W. Debye. “Interferenz von Röntgenstrahlen und Wärmebewegung”. *Annalen der Physik* **348** (1913), pp. 49–92. DOI: 10.1002/andp.19133480105.

[60] I. Waller. “Zur Frage der Einwirkung der Wärmebewegung auf die Interferenz von Röntgenstrahlen”. German. *Zeitschrift für Physik* **17** (1923), pp. 398–408. DOI: 10.1007/BF01328696.

[61] A. Guinier. *X-ray diffraction in crystals, imperfect crystals, and amorphous bodies*. Dover, 1994.

[62] J. Als-Nielsen and D. McMorrow. *Elements of modern X-ray physics*. New York: John Wiley & Sons, 2011.

[63] M. Born. “Quantenmechanik der Stoßvorgänge”. *Zeitschrift für Physik* **38** (1926), pp. 803–827. DOI: 10.1007/BF01397184.

[64] P. Coppens. “The structure factor”. English. In: *International Tables for Crystallography Volume B: Reciprocal space*. Ed. by U. Shmueli. Vol. B. International Tables for Crystallography. Springer Netherlands, 2001, pp. 10–24. DOI: 10.1107/97809553602060000550.

[65] P. Brown, A. Fox, E. Maslen, M. O’Keefe, and B. Willis. “Intensity of diffracted intensities”. English. In: *International Tables for Crystallography Volume C: Mathematical, physical and chemical tables*. Ed. by E. Prince. Vol. C. International Tables for Crystallography. Springer Netherlands, 2004, pp. 554–595. DOI: 10.1107/97809553602060000600.

[66] C.T. Chantler. “Theoretical Form Factor, Attenuation, and Scattering Tabulation for $Z = 1 - 92$ from $E = 1 - 10$ eV to $E = 0.4 - 1.0$ MeV”. *Journal of Physical and Chemical Reference Data* **24** (1995), pp. 71–643. DOI: dx.doi.org/10.1063/1.555974.

[67] I.K. Robinson. “Coherent diffraction: Giant molecules or tiny crystals?” *Nature Matererials* **7** (2008), pp. 275–276. DOI: 10.1038/nmat2144.

[70] P.J.W. Debye. “Zerstreuung von Röntgenstrahlen”. *Annalen der Physik* **351** (1915), pp. 809–823. DOI: 10.1002/andp.19153510606.

[71] M.v. Laue. “Lorentz-Faktor und Intensitätsverteilung in Debye-Scherrer Ringen.” *Zeitschrift für Kristallographie - Crystalline Materials* **64** (1926), pp. 115–142. DOI: 10.1524/zkri.1926.64.1.115.

[72] L.H. Germer and A.H. White. “Electron Diffraction Studies of Thin Films. II. Anomalous Powder Patterns Produced by Small Crystals”. *Physical Review* **60** (1941), pp. 447–454. DOI: 10.1103/PhysRev.60.447.

[73] O. Glatter. “Computation of distance distribution functions and scattering functions of models for small angle scattering experiments”. *Acta Physica Austriaca* **52** (1980), pp. 243–256.

[74] B.D. Hall and R. Monot. “Calculating the Debye–Scherrer diffraction pattern for large clusters”. *Computers in Physics* **5** (1991), pp. 414–417. DOI: 10.1063/1.168397.

[75] Nvidia. *http://www.nvidia.com/*.

[76] Intel. *http://www.intel.com/*.

[77] Message Passing Interface Forum. *MPI: A Message-Passing Interface Standard (version 3.0)*. Tech. rep. University of Tennessee, 2012.

[78] C.W.B. Grigson. “Validity of the Debye Scattering Equation in Elastic Electron Diffraction”. *Nature* **215** (1967), pp. 382–383. DOI: 10.1038/215382b0.

[79] D. Rafaja, V. Valvoda, J. Kub, K. Temst, M.J. Van Bael, and Y. Bruynseraede. “Long-range periodicity and disorder in two-dimensional arrays of metallic dots studied by x-ray diffraction”. *Physical Review B* **61** (2000), pp. 16144–16153. DOI: 10.1103/PhysRevB.61.16144.

[80] D. Rafaja, V. Klemm, G. Schreiber, M. Knapp, and R. Kužel. “Interference phenomena observed by X-ray diffraction in nanocrystalline thin films”. *Journal of Applied Crystallography* **37** (2004), pp. 613–620. DOI: 10.1107/S0021889804012701.

[81] G. Ribárik, N. Audebrand, H. Palancher, T. Ungár, and D. Louër. “Dislocation densities and crystallite size distributions in nanocrystalline ball-milled fluorides, MF2 (M = Ca, Sr, Ba and Cd), determined by X-ray diffraction line-profile analysis”. *Journal of Applied Crystallography* **38** (2005), pp. 912–926. DOI: 10.1107/S0021889805027202.

[82] D. Rafaja, A. Poklad, V. Klemm, G. Schreiber, D. Heger, M. Šíma, and M. Dopita. “Some consequences of the partial crystallographic coherence between nanocrystalline domains in Ti–Al–N and Ti–Al–Si–N coatings”. *Thin Solid Films* **514** (2006), pp. 240–249. DOI: http://dx.doi.org/10.1016/j.tsf.2006.02.092.

[83] D. Rafaja, C. Wüstefeld, M. Dopita, M. Růžička, V. Klemm, G. Schreiber, D. Heger, and M. Šíma. “Internal structure of clusters of partially coherent nanocrystallites in Cr–Al–N and Cr–Al–Si–N coatings”. *Surface and Coatings Technology* **201** (2007), pp. 9476–9484. DOI: http://dx.doi.org/10.1016/j.surfcoat.2007.04.007.

[84] S. Förster, A. Timmann, C. Schellbach, A. Frömsdorf, A. Kornowski, H. Weller, S.V. Roth, and P. Lindner. "Order causes secondary Bragg peaks in soft materials". *Nature Matererials* **6** (2007), pp. 888–893. DOI: 10.1038/nmat1995.

[85] U. Pietsch, V. Holý, and T. Baumbach. *High-Resolution X-Ray Scattering: From Thin Films to Lateral Nanostructures. 2^{nd} ed.* Vol. 149. Springer Tracts in Modern Physics, 2004.

[86] R. Stömmer and U. Pietsch. "Coherence phenomena in x-ray diffuse scattering on organic multilayers". *Journal of Physics D: Applied Physics* **29** (1996), pp. 3161–3165. DOI: 10.1088/0022-3727/29/12/034.

[87] C.G. Darwin. "XCII. The reflexion of X-rays from imperfect crystals". *Philosophical Magazine Series 6* **43** (1922), pp. 800–829. DOI: 10.1080/14786442208633940.

[88] P. Scherrer. "Bestimmung der Größe und der inneren Struktur von Kolloidteilchen mittels Röntgenstrahlen". *Nachrichten von der Gesellschaft der Wissenschaften zu Göttingen, Mathematisch-Physikalische Klasse* **1918** (1918), pp. 98–100.

[89] A.L. Patterson. "The Scherrer Formula for X-Ray Particle Size Determination". *Physical Review* **56** (1939), pp. 978–982. DOI: 10.1103/PhysRev.56.978.

[90] M. Lüscher. "A portable high-quality random number generator for lattice field theory calculations". *Computer Physics Communications* **79** (1994), pp. 100–110. DOI: 10.1016/0010-4655(94)90232-1.

[91] M. Galassi, J. Davies, J. Theiler, B. Gough, G. Jungman, P. Alken, M. Booth, and F. Rossi. *GNU Scientific Library Reference Manual. 3^{rd} ed.* Network Theory Limited. 2009.

[92] L.G. Dirichlet. "Über die Reduction der positiven quadratischen Formen mit drei unbestimmten ganzen Zahlen." *Journal für die reine und angewandte Mathematik* **40** (1850), pp. 209–227. DOI: 10.1515/crll.1850.40.209.

[93] W. Gao, L.B. Alemany, L. Ci, and P.M. Ajayan. "New insights into the structure and reduction of graphite oxide". *Nature Chemistry* **1** (2009), pp. 403–408. DOI: 10.1038/nchem.281.

[94] D.R. Dreyer, S. Park, C.W. Bielawski, and R.S. Ruoff. "The chemistry of graphene oxide". *Chemical Society Reviews* **39** (2010), pp. 228–240. DOI: 10.1039/B917103G.

[95] A. Lerf, A. Buchsteiner, J. Pieper, S. Schöttl, I. Dekany, T. Szabo, and H.P. Boehm. "Hydration behavior and dynamics of water molecules in graphite oxide". *Journal of Physics and Chemistry of Solids* **67** (2006), pp. 1106–1110. DOI: http://dx.doi.org/10.1016/j.jpcs.2006.01.031.

[96] W.S. Hummers and R.E. Offeman. "Preparation of Graphitic Oxide". *Journal of the American Chemical Society* **80** (1958), pp. 1339–1339. DOI: 10.1021/ja01539a017.

[97] A. Hashimoto, K. Suenaga, A. Gloter, K. Urita, and S. Iijima. "Direct evidence for atomic defects in graphene layers". *Nature* **430** (2004), pp. 870–873. DOI: 10.1038/nature02817.

[98] F. Banhart, J. Kotakoski, and A.V. Krasheninnikov. "Structural Defects in Graphene". *ACS Nano* **5** (2011), pp. 26–41. DOI: 10.1021/nn102598m.

[99] J.C. Meyer, A.K. Geim, M.I. Katsnelson, K.S. Novoselov, T.J. Booth, and S. Roth. "The structure of suspended graphene sheets". *Nature* **446** (2007), pp. 60–63. DOI: 10.1038/nature05545.

[100] J.J. Sakurai. *Modern Quantum Mechanics*. Ed. by S.F. Tuan. Addison-Wesley Publishing Company, 1994.

[101] S. Mobilio. "Introduction to Matter Radiation Interaction". In: *Synchrotron Radiation*. Ed. by S. Mobilio, F. Boscherini, and C. Meneghini. Springer Berlin Heidelberg, 2015, pp. 107–143. DOI: 10.1007/978-3-642-55315-8_4.

[102] C.M. Bertoni. "Quantum Description of the Matter-Radiation Interaction". In: *Synchrotron Radiation*. Ed. by S. Mobilio, F. Boscherini, and C. Meneghini. Springer Berlin Heidelberg, 2015, pp. 145–178. DOI: 10.1007/978-3-642-55315-8_5.

[105] L.D. Marks. "Experimental studies of small particle structures". *Reports on Progress in Physics* **57** (1994), pp. 603–649. DOI: 10.1088/0034-4885/57/6/002.

[106] D. Shechtman, I. Blech, D. Gratias, and J.W. Cahn. "Metallic Phase with Long-Range Orientational Order and No Translational Symmetry". *Phys. Rev. Lett.* **53** (1984), pp. 1951–1953. DOI: 10.1103/PhysRevLett.53.1951.

[107] F. Baletto and R. Ferrando. "Structural properties of nanoclusters: Energetic, thermodynamic, and kinetic effects". *Review of Modern Physics* **77** (2005), pp. 371–423. DOI: 10.1103/RevModPhys.77.371.

[108] Y. Xia, Y. Xiong, B. Lim, and S.E. Skrabalak. "Shape-Controlled Synthesis of Metal Nanocrystals: Simple Chemistry Meets Complex Physics?" *Angewandte Chemie International Edition* **48** (2009), pp. 60–103. DOI: 10.1002/anie.200802248.

[109] W. Niu and G. Xu. "Crystallographic control of noble metal nanocrystals". *Nano Today* **6** (2011), pp. 265–285. DOI: http://dx.doi.org/10.1016/j.nantod.2011.04.006.

[110] R. Smoluchowski. "Anisotropy of the Electronic Work Function of Metals". *Physical Review* **60** (1941), pp. 661–674. DOI: 10.1103/PhysRev.60.661.

[111] A.C. Nunes and D. Lin. "Effects of Surface Relaxation on Powder Diffraction Patterns of Very Fine Particles". *Journal of Applied Crystallography* **28** (1995), pp. 274–278. DOI: 10.1107/S0021889894011039.

[112] K. Ishikawa and T. Uemori. "Surface relaxation in ferroelectric perovskites". *Physical Review B* **60** (1999), pp. 11841–11845. DOI: 10.1103/PhysRevB.60.11841.

[113] M. Leoni and P. Scardi. "Grain Surface Relaxation Effects in Powder Diffraction". In: *Diffraction Analysis of theMicrostructure of Materials*. Ed. by P. Scardi and E.J. Mittemeijer. Vol. 68. Springer Series in Materials Science. Springer Verlag, Berlin, 2003. Chap. 16, pp. 413–454.

[114] S. Plimpton. "Fast Parallel Algorithms for Short-Range Molecular Dynamics". *Journal of Computational Physics* **117** (1995), pp. 1–19. DOI: http://dx.doi.org/10.1006/jcph.1995.1039.

[115] H.W. Sheng, M.J. Kramer, A. Cadien, T. Fujita, and M.W. Chen. "Highly optimized embedded-atom-method potentials for fourteen fcc metals". *Physical Review B* **83** (2011), pp. 134118–134137. DOI: 10.1103/PhysRevB.83.134118.

[116] C.F. Gauss. *Theoria motus corporum coelestium in sectionibus conicis solem ambientium*. F. Perthes and I.H. Besser, 1809.

[117] J.J. Waterston. "On the Physics of Media that are Composed of Free and Perfectly Elastic Molecules in a State of Motion". *Philosophical Transactions of the Royal Society of London A* **183** (1892), pp. 1–79.

[118] T. Schneider and E. Stoll. "Molecular-dynamics study of a three-dimensional one-component model for distortive phase transitions". *Physical Review B* **17** (1978), pp. 1302–1322. DOI: 10.1103/PhysRevB.17.1302.

[119] W. Shinoda, M. Shiga, and M. Mikami. "Rapid estimation of elastic constants by molecular dynamics simulation under constant stress". *Physical Review B* **69** (2004), pp. 134103–134110. DOI: 10.1103/PhysRevB.69.134103.

[120] T. Young. "An Essay on the Cohesion of Fluids". *Philosophical Transactions of the Royal Society of London* **95** (1805), pp. 65–87. DOI: 10.1098/rstl.1805.0005.

[121] P.-S. Laplace, Marquis de. *Traité de Mécanique Céleste*. Vol. 4. Courcier, 1805.

[122] R. Hooke. *Ut tensio, sic vis*. Enunced as anagram. 1660.

[123] K.R. Beyerlein, R.L. Snyder, M. Li, and P. Scardi. "Simulation and Modeling of Nanoparticle Surface Strain". *Journal of Nanoscience and Nanotechnology* **12** (2012), pp. 8554–8560. DOI: 10.1166/jnn.2012.6473.

[124] L. Pauling. "Atomic Radii and Interatomic Distances in Metals". *Journal of the American Chemical Society* **69** (1947), pp. 542–553. DOI: 10.1021/ja01195a024.

[125] W.J. Huang, R. Sun, J. Tao, L.D. Menard, R.G. Nuzzo, and J.-M. Zuo. "Coordination-dependent surface atomic contraction in nanocrystals revealed by coherent diffraction". *Nature Materials* **7** (2008), pp. 308–313. DOI: 10.1038/nmat2132.

[126] J.F. Nye. *Physical Properties of Crystals: Their Representation by Tensors and Matrices*. Oxford University Press, 1985.

[127] C. Yang, M. Xiao, W. Li, and Q. Jiang. "Size effects on Debye temperature, Einstein temperature, and volume thermal expansion coefficient of nanocrystals". *Solid State Communications* **139** (2006), pp. 148–152. DOI: 10.1016/j.ssc.2006.05.035.

[128] R. Kumar, G. Sharma, and M. Kumar. "Effect of Size and Shape on the Vibrational and Thermodynamic Properties of Nanomaterials". *Journal of Thermodynamics* **2013** (2013), pp. 328051–328055. DOI: 10.1155/2013/328051.

[129] R. Meyer and P. Entel. "Vibrational properties of metallic nanoparticles". *Zeitschrift für Kristallographie* **222** (2007), pp. 646–649. DOI: 10.1524/zkri.2007.222.11.646.

[130] Y.H. Zhao, H.W. Sheng, and K. Lu. "Microstructure evolution and thermal properties in nanocrystalline Fe during mechanical attrition". *Acta Materialia* **49** (2001), pp. 365–375. DOI: 10.1016/S1359-6454(00)00310-4.

[131] P. Scardi. "Microstructural properties: lattice defects and domain size effects". In: *Powder Diffraction: Theory and Practice*. The Royal Society of Chemistry, 2008. Chap. 13, pp. 376–413. DOI: 10.1039/9781847558237-00464.

[132] M. Leoni, T. Confente, and P. Scardi. "PM2K: a flexible program implementing Whole Powder Pattern Modelling". *Zeitschrift für Kristallographie Supplements* **23** (2006), pp. 249–254. DOI: 10.1524/zksu.2006.suppl_23.249.

[133] A. Leonardi, M. Leoni, S. Siboni, and P. Scardi. "Common volume functions and diffraction line profiles of polyhedral domains". *Journal of Applied Crystallography* **45** (2012), pp. 1162–1172. DOI: 10.1107/S0021889812039283.

[134] J. Martinez-Garcia, M. Leoni, and P. Scardi. "A general approach for determining the diffraction contrast factor of straight-line dislocations". *Acta Crystallographica Section A* **65** (2009), pp. 109–119. DOI: 10.1107/S010876730804186X.

[135] P. Scardi and M. Leoni. "Diffraction line profiles from polydisperse crystalline systems". *Acta Crystallographica Section A* **57** (2001), pp. 604–613. DOI: 10.1107/S0108767301008881.

[136] P. Scardi and M. Leoni. "Whole powder pattern modelling". *Acta Crystallographica Section A* **58** (2002), pp. 190–200. DOI: 10.1107/S0108767301021298.

[137] K.R. Beyerlein, R.L. Snyder, and P. Scardi. "Powder diffraction line profiles from the size and shape of nanocrystallites". *Journal of Applied Crystallography* **44** (2011), pp. 945–953. DOI: 10.1107/S0021889811030743.

[138] J.P. Urban. "Thermal diffuse X-ray scattering for small samples and small coherent scattering domains". *Acta Crystallographica Section A* **31** (1975), pp. 95–100. DOI: 10.1107/S0567739475000186.

[139] K.R. Beyerlein, M. Leoni, and P. Scardi. "Temperature diffuse scattering of nanocrystals". *Acta Crystallographica Section A* **68** (2012), pp. 382–392. DOI: 10.1107/S0108767312009853.

[140] T. Adler and C.R. Houska. "Simplifications in the x-ray line-shape analysis". *Journal of Applied Physics* **50** (1979), pp. 3282–3287. DOI: 10.1063/1.326368.

[141] N.C. Popa. "The (*hkl*) Dependence of Diffraction-Line Broadening Caused by Strain and Size for all Laue Groups in Rietveld Refinement". *Journal of Applied Crystallography* **31** (1998), pp. 176–180. DOI: 10.1107/S0021889897009795.

[142] C. Zener. *Elasticity and anelasticity of metals*. University of Chicago Press, 1948.

[143] T. Ino and N. Minami. "Intensity profile of Debye–Scherrer line from small crystallites". *Acta Crystallographica Section A* **40** (1984), pp. 538–544. DOI: 10.1107/S0108767384001136.

[144] J. Sheng, U. Welzel, and E.J. Mittemeijer. "Nonmonotonic crystallite-size dependence of the lattice parameter of nanocrystalline nickel". *Applied Physics Letters* **97**, 153109 (2010), pp. 153109–153112. DOI: http://dx.doi.org/10.1063/1.3500827.

[145] L.-M. Peng, G. Ren, S.L. Dudarev, and M.J. Whelan. "Debye–Waller Factors and Absorptive Scattering Factors of Elemental Crystals". *Acta Crystallographica Section A* **52** (1996), pp. 456–470. DOI: 10.1107/S010876739600089X.

[146] B.E. Warren and B.L. Averbach. "The Effect of Cold-Work Distortion on X-Ray Patterns". *Journal of Applied Physics* **21** (1950), pp. 595–599. DOI: 10.1063/1.1699713.

[147] G. Corthey *et al.* "Influence of Capping on the Atomistic Arrangement in Palladium Nanoparticles at Room Temperature". *The Journal of Physical Chemistry C* **118** (2014), pp. 24641–24647. DOI: 10.1021/jp5083505.

[148] P.K. Ghorai and S.C. Glotzer. "Molecular Dynamics Simulation Study of Self-Assembled Monolayers of Alkanethiol Surfactants on Spherical Gold Nanoparticles". *The Journal of Physical Chemistry C* **111** (2007), pp. 15857–15862. DOI: 10.1021/jp0746289.

[149] L. Gelisio. *https://sites.google.com/site/lucagelisio/research/algorithms/storm*.

[150] Free Software Foundation. *GNU General Public License (version 3)*. http://www.gnu.org/licenses/gpl.html. 2007.

[151] J.S. Liu. *Monte Carlo Strategies in Scientific Computing. 2nd ed.* Springer Series in Statistics. Springer, 2008.

[152] B.H. Toby. "R factors in Rietveld analysis: How good is good enough?" *Powder Diffraction* **21** (2006), pp. 67–70. DOI: 10.1154/1.2179804.

[153] W.K. Hastings. “Monte Carlo sampling methods using Markov chains and their applications”. *Biometrika* **57** (1970), pp. 97–109. DOI: 10.1093/biomet/57.1.97.

[154] S. Kirkpatrick, C. Gelatt, and M. Vecchi. “Optimization by Simulated Annealing”. *Science* **220** (1983), pp. 671–680. DOI: 10.1126/science.220.4598.671.

[155] V. Černý. “Thermodynamical approach to the traveling salesman problem: An efficient simulation algorithm”. *Journal of Optimization Theory and Applications* **45** (1985), pp. 41–51. DOI: 10.1007/bf00940812.

[156] A. Corana, M. Marchesi, C. Martini, and S. Ridella. “Minimizing Multimodal Functions of Continuous Variables with the ’Simulated Annealing’ Algorithm”. *ACM Transactions on Mathematical Software* **13** (1987), pp. 262–280.

[157] International Organization for Standardization (ISO). *ISO/IEC 14882:2011*. Geneva, Switzerland, 2012.

[158] Nvidia. *CUDA C Programming Guide (version 6.5)*. 2014.

[159] Python Software Foundation. *Python Language Reference (version 3.4)*. 2014.

[160] R.H. Swendsen and J.-S. Wang. “Replica Monte Carlo simulation of spin glasses”. *Physical Review Letters* **57** (1986), pp. 2607–2609. DOI: 10.1103/PhysRevLett.57.2607.

[161] C.J. Geyer. “Markov chain Monte Carlo maximum likelihood”. In: *Computing Science and Statistics: Proceedings of the 23rd Symposium on the Interface*. Ed. by E.M. Keramidas. Interface Foundation, 1991, pp. 156–163.

[162] A. Laio and M. Parrinello. “Escaping free-energy minima”. *Proceedings of the National Academy of Sciences of the United States of America* **99** (2002), pp. 12562–12566. DOI: 10.1073/pnas.202427399.

[163] T.S. Ahmadi, Z.L. Wang, T.C. Green, A. Henglein, and M.A. El-Sayed. “Shape-controlled synthesis of colloidal platinum nanoparticles”. *Science* **272** (1996), pp. 1924–1926. DOI: 10.1126/science.272.5270.1924.

[164] H. Lee, S.E. Habas, S. Kweskin, D. Butcher, G.A. Somorjai, and P. Yang. “Morphological control of catalytically active platinum nanocrystals”. *Angewandte Chemie* **118** (2006), pp. 7988–7992. DOI: 10.1002/ange.200603068.

[165] N. Tian, Z.-Y. Zhou, S.-G. Sun, Y. Ding, and Z.L. Wang. "Synthesis of Tetrahexahedral Platinum Nanocrystals with High-Index Facets and High Electro-Oxidation Activity". *Science* **316** (2007), pp. 732–735. DOI: 10.1126/science.1140484.

[166] I. Lee, F. Delbecq, R. Morales, M.A. Albiter, and F. Zaera. "Tuning selectivity in catalysis by controlling particle shape". *Nature Materials* **8** (2009), pp. 132–138. DOI: 10.1038/nmat2371.

[167] M. Jin, H. Zhang, Z. Xie, and Y. Xia. "Palladium nanocrystals enclosed by 100 and 111 facets in controlled proportions and their catalytic activities for formic acid oxidation". *Energy & Environmental Science* **5** (2012), pp. 6352–6357. DOI: 10.1039/C2EE02866B.

[168] M. Laskar and S.E. Skrabalak. "Decoupling the Geometric Parameters of Shape-Controlled Pd Nanocatalysts". *ACS Catalysis* **4** (2014), pp. 1120–1128. DOI: 10.1021/cs401064d.

[169] K.M. Bratlie, H. Lee, K. Komvopoulos, P. Yang, and G.A. Somorjai. "Platinum Nanoparticle Shape Effects on Benzene Hydrogenation Selectivity". *Nano Letters* **7** (2007), pp. 3097–3101. DOI: 10.1021/nl0716000.

[170] C.-K. Tsung, J.N. Kuhn, W. Huang, C. Aliaga, L.-I. Hung, G.A. Somorjai, and P. Yang. "Sub-10 nm Platinum Nanocrystals with Size and Shape Control: Catalytic Study for Ethylene and Pyrrole Hydrogenation". *Journal of the American Chemical Society* **131** (2009), pp. 5816–5822. DOI: 10.1021/ja809936n.

[171] A. Nilsson, L.G.M. Pettersson, B. Hammer, T. Bligaard, C.H. Christensen, and J.K. Nørskov. "The electronic structure effect in heterogeneous catalysis". English. *Catalysis Letters* **100** (2005), pp. 111–114. DOI: 10.1007/s10562-004-3434-9.

[172] J.K. Nørskov, T. Bligaard, J. Rossmeisl, and C.H. Christensen. "Towards the computational design of solid catalysts". *Nature Chemistry* **1** (2009), pp. 37–46. DOI: 10.1038/nchem.121.

[173] S.J. Hwang *et al.* "Role of Electronic Perturbation in Stability and Activity of Pt-Based Alloy Nanocatalysts for Oxygen Reduction". *Journal of the American Chemical Society* **134** (2012), pp. 19508–19511. DOI: 10.1021/ja307951y.

[174] H. Xin and S. Linic. "Communications: Exceptions to the *d*-band model of chemisorption on metal surfaces: The dominant role of repulsion between adsorbate states and metal *d*-states". *The Journal of Chemical Physics* **132**, 221101 (2010), pp. 221101–221104. DOI: http://dx.doi.org/10.1063/1.3437609.

[175] T.H. Yu, T. Hofmann, Y. Sha, B.V. Merinov, D.J. Myers, C. Heske, and W.A. Goddard. "Finding Correlations of the Oxygen Reduction Reaction Activity of Transition Metal Catalysts with Parameters Obtained from Quantum Mechanics". *The Journal of Physical Chemistry C* **117** (2013), pp. 26598–26607. DOI: 10.1021/jp4071554.

[176] K.W. Urban. "Studying Atomic Structures by Aberration-Corrected Transmission Electron Microscopy". *Science* **321** (2008), pp. 506–510. DOI: 10.1126/science.1152800.

[177] Z.Y. Li *et al.* "Three-dimensional atomic-scale structure of size-selected gold nanoclusters". *Nature* **451** (2008), pp. 46–48. DOI: 10.1038/nature06470.

[178] S.J.L. Billinge and I. Levin. "The Problem with Determining Atomic Structure at the Nanoscale". *Science* **316** (2007), pp. 561–565. DOI: 10.1126/science.1135080.

[179] D. Wang, H.L. Xin, R. Hovden, H. Wang, Y. Yu, D.A. Muller, F.J. DiSalvo, and H.D. Abruña. "Structurally ordered intermetallic platinum-cobalt core-shell nanoparticles with enhanced activity and stability as oxygen reduction electrocatalysts". *Nature Materials* **12** (2013), pp. 81–87. DOI: 10.1038/nmat3458.

[180] C.-C. Chen *et al.* "Three-dimensional imaging of dislocations in a nanoparticle at atomic resolution". *Nature* **496** (2013), pp. 74–77. DOI: 10.1038/nature12009.

[181] V. Ortalan, A. Uzun, B.C. Gates, and N.D. Browning. "Towards full-structure determination of bimetallic nanoparticles with an aberration-corrected electron microscope". *Nature Nanotechnology* **5** (2010), pp. 843–847. DOI: 10.1038/nnano.2010.234.

[182] N. Shibata, S.J. Pennycook, T.R. Gosnell, G.S. Painter, W.A. Shelton, and P.F. Becher. "Observation of rare-earth segregation in silicon nitride ceramics at subnanometre dimensions". *Nature* **428** (2004), pp. 730–733. DOI: 10.1038/nature02410.

[183] C. Cui, L. Gan, M. Heggen, S. Rudi, and P. Strasser. "Compositional segregation in shaped Pt alloy nanoparticles and their structural behaviour during electrocatalysis". *Nature Materials* **12** (2013), pp. 765–771. DOI: 10.1038/nmat3668.

[184] C. Kisielowski *et al.* "Detection of Single Atoms and Buried Defects in Three Dimensions by Aberration-Corrected Electron Microscope with 0.5-Å Information Limit". *Microscopy and Microanalysis* **14** (2008), pp. 469–477. DOI: 10.1017/S1431927608080902.

[185] S.I. Sanchez, M.W. Small, E.S. Bozin, J.-G. Wen, J.-M. Zuo, and R.G. Nuzzo. "Metastability and Structural Polymorphism in Noble Metals: The Role of Composition and Metal Atom Coordination in Mono- and Bimetallic Nanoclusters". *ACS Nano* **7** (2013), pp. 1542–1557. DOI: 10.1021/nn305314m.

[186] S. Iijima and T. Ichihashi. "Structural instability of ultrafine particles of metals". *Physical Review Letters* **56** (1986), pp. 616–619. DOI: 10.1103/PhysRevLett.56.616.

[187] P.M. Ajayan and L.D. Marks. "Experimental evidence for quasimelting in small particles". *Physical Review Letters* **63** (1989), pp. 279–282. DOI: 10.1103/PhysRevLett.63.279.

[188] I.K. Robinson. "Nanoparticle Structure by Coherent X-ray Diffraction". *Journal of the Physical Society of Japan* **82** (2013), pp. 021012–021018. DOI: 10.7566/JPSJ.82.021012.

[189] S. Marchesini *et al.* "Coherent X-ray diffractive imaging: applications and limitations". *Optics Express* **11** (2003), pp. 2344–2353. DOI: 10.1364/OE.11.002344.

[190] R. Neutze, R. Wouts, D. van der Spoel, E. Weckert, and J. Hajdu. "Potential for biomolecular imaging with femtosecond X-ray pulses". *Nature* **406** (2000), pp. 752–757. DOI: 10.1038/35021099.

[191] M. Jin, H. Liu, H. Zhang, Z. Xie, J. Liu, and Y. Xia. "Synthesis of Pd nanocrystals enclosed by {100} facets and with sizes <10 nm for application in CO oxidation". English. *Nano Research* **4** (2011), pp. 83–91. DOI: 10.1007/s12274-010-0051-3.

[192] H.J. Wasserman and J.S. Vermaak. "On the determination of a lattice contraction in very small silver particles". *Surface Science* **22** (1970), pp. 164–172. DOI: http://dx.doi.org/10.1016/0039-6028(70)90031-2.

[193] H. Sheng. *https://sites.google.com/site/eampotentials/Pd*.

[194] 11BM at the Advanced Photon Source. *http://11bm.xray.aps.anl.gov/*.

[195] J. Wang *et al.* "A dedicated powder diffraction beamline at the Advanced Photon Source: Commissioning and early operational results". *Review of Scientific Instruments* **79**, 085105 (2008), pp. 085105–085111. DOI: http://dx.doi.org/10.1063/1.2969260.

[196] P.J.W. Debye and P. Scherrer. "Interferenzen an regellos orientierten Teilchen im Röntgenlicht. I". *Physikalische Zeitschrift* **17** (1916), pp. 277–283.

[197] National Institute of Standards & Technology. *Standard Reference Material® 660b*.

[198] D.R. Black, D. Windover, A. Henins, J. Filliben, and J.P. Cline. "Certification of Standard Reference Material 660B". *Powder Diffraction* **26** (2011), pp. 155–158. DOI: 10.1154/1.3591064.

[199] J. Langford. "A rapid method for analysing the breadths of diffraction and spectral lines using the Voigt function". *Journal of Applied Crystallography* **11** (1978), pp. 10–14. DOI: 10.1107/S0021889878012601.

[200] F. Sánchez-Bajo and F.L. Cumbrera. "The Use of the Pseudo-Voigt Function in the Variance Method of X-ray Line-Broadening Analysis". *Journal of Applied Crystallography* **30** (1997), pp. 427–430. DOI: 10.1107/S0021889896015464.

[201] P.L. Chebyshev. "Théorie des mécanismes connus sous le nom de parallélogrammes". In: *Mémoires des Savants étrangers présentés à l'Académie de Saint-Pétersbourg*. Vol. 7. Imprimerie de l'Acadeémie Impeériale des Sciences, 1854.

[202] E.N. Maslen. "X-ray absorption". In: *International Tables for Crystallography Volume C: Mathematical, physical and chemical tables*. Ed. by E. Prince. Vol. C. International Tables for Crystallography. Springer Netherlands, 2004, pp. 599–608.

[203] M. Bowden and M. Ryan. "Absorption correction for cylindrical and annular specimens and their containers or supports". *Journal of Applied Crystallography* **43** (2010), pp. 693–698. DOI: 10.1107/S0021889810021114.

[204] T.M. Sabine, B.A. Hunter, W.R. Sabine, and C.J. Ball. "Analytical Expressions for the Transmission Factor and Peak Shift in Absorbing Cylindrical Specimens". *Journal of Applied Crystallography* **31** (1998), pp. 47–51. DOI: 10.1107/S0021889897006961.

[205] E.J. Kirkland. *Advanced Computing in Electron Microscopy. 2nd ed.* Springer, 2010.

[206] E. Runge and E.K.U. Gross. "Density-Functional Theory for Time-Dependent Systems". *Physical Review Letters* **52** (1984), pp. 997–1000. DOI: 10.1103/PhysRevLett.52.997.

[207] R. Car and M. Parrinello. "Unified Approach for Molecular Dynamics and Density-Functional Theory". *Physical Review Letters* **55** (1985), pp. 2471–2474. DOI: 10.1103/PhysRevLett.55.2471.

[208] IBM. *http://www-03.ibm.com/ibm/history/exhibits/mainframe/mainframe_PP704.html*.

[209] T.C. Germann and K. Kadau. "Trillion-atom molecular dynamics becomes a reality". *International Journal of Modern Physics C* **19** (2008), pp. 1315–1319. DOI: 10.1142/S0129183108012911.

[210] The GIMP team. *GIMP http://www.gimp.org/*.

[211] J.D. Hunter. "Matplotlib: A 2D graphics environment". *Computing In Science & Engineering* **9** (2007), pp. 90–95. DOI: 10.1109/MCSE.2007.55.

[212] W. Humphrey, A. Dalke, and K. Schulten. "VMD – Visual Molecular Dynamics". *Journal of Molecular Graphics* **14** (1996), pp. 33–38. DOI: 10.1016/0263-7855(96)00018-5.

[213] US National Institute of Standards and Technology. *The NIST Reference on Constants, Units, and Uncertainty. http://physics.nist.gov/cuu/index.html*. 2011.

Scientific Production

[45] L. Gelisio and P. Scardi. "X-Ray Interference by Nanocrystalline Domains". *Journal of Nanoscience and Nanotechnology* **12** (2012), pp. 8811–8817. DOI: 10.1166/jnn.2012.6479.

[46] L. Gelisio and P. Scardi. "On the Modeling of the Diffraction Pattern from Metal Nanocrystals". *Metallurgical and Materials Transactions A*[†] **45** (2014), pp. 1–10. DOI: 10.1007/s11661-014-2407-x.

[47] P. Scardi and L. Gelisio. "Diffraction from Nanocrystalline Materials". In: *Synchrotron Radiation: Basics, Methods and Applications*. Ed. by S. Mobilio, F. Boscherini, and C. Meneghini. Springer Berlin Heidelberg, 2015. Chap. 18, pp. 499–518. DOI: 10.1007/978-3-642-55315-8_18.

[68] L. Gelisio, C.L. Azanza Ricardo, M. Leoni, and P. Scardi. "Real-space calculation of powder diffraction patterns on graphics processing units". *Journal of Applied Crystallography* **43** (2010), pp. 647–653. DOI: 10.1107/S0021889810005133.

[69] L. Gelisio, C.L. Azanza Ricardo, M. Leoni, and P. Scardi. "Real-space powder diffraction computing on clusters of Graphics Processing Units". *Zeitschrift für Kristallographie Proceedings* **1** (2011), pp. 189–194.

[103] L. Gelisio, K.R. Beyerlein, and P. Scardi. "Atomistic modeling of lattice relaxation in metallic nanocrystals". *Thin Solid Films* **530** (2013), pp. 35–39. DOI: 10.1016/j.tsf.2012.07.063.

[104] P. Scardi, A. Leonardi, L. Gelisio, M.R. Suchomel, B.T. Sneed, M.K. Sheehan, and C.-K. Tsung. "X-ray powder diffraction imaging of anisotropic atom displacement in metal nanocrystals". *submitted* (2014).

[†]Complimentary Editors' Choice for Free Access (E-SYMP-14-458-A)